

ELLIPSOMETRY OF SEMICONDUCTORS UNDER THERMAL AND
LASER EXCITATION

BY

CAROLA EMMINGER, B.S., M.S.

A dissertation submitted to the Graduate School

in partial fulfillment of the requirements

for the degree

Doctor of Philosophy

Major Subject: Physics

New Mexico State University

Las Cruces, New Mexico

December 2021

Carola Emminger

Candidate

Physics

Major

This dissertation is approved on behalf of the faculty of New Mexico State University, and it is acceptable in quality and form for publication:

Approved by the Dissertation Committee:

Dr. Stefan Zollner

Committee Member

Dr. Michael Engelhardt

Committee Member

Dr. Igor Vasiliev

Committee Member

Dr. David Voelz

Committee Member

Dr. Adam Dubroka

Committee Member

ACKNOWLEDGMENTS

First and foremost, I would like to thank my Ph.D. thesis advisor Dr. Stefan Zollner for his support throughout my studies at New Mexico State University (NMSU), as well as for his patience and willingness to answer all my physics questions and sharing his knowledge and experience with me. I am really grateful that I had the chance to be part of the graduate program at the Department of Physics at NMSU, where I could gain experience in research as well as teaching, but also that I was encouraged to travel to numerous conferences and workshops to present our research.

My gratitude also goes to my thesis committee members Dr. Michael Engelhardt, Dr. Igor Vasiliev, and Dr. David Voelz at NMSU, and Dr. Adam Dubroka at Masaryk University in Brno, Czech Republic. During the last year of my Ph.D. studies, I had the chance to stay at the Condensend Matter Physics Department at Masaryk University, for which I would like to thank Dr. Dominik Munzar and Dr. Adam Dubroka.

Many thanks also to my colleagues in the ellipsometry group at NMSU, especially Nuwanjula Samarasingha, Farzin Abadizaman, and Rigo Carrasco for all their help and for being such great colleagues. Furthermore, I would like to say thank you to Nuwanjula Samarasingha and Melissa Rivero Arias for taking measurements at NMSU, while I was not able to travel to Las Cruces myself. I

would also like to express my appreciation to the current and former ellipsometry group members Carlos Armenta, Melissa Rivero Arias, Jaden Love, Haley Woolf, Yoshitha Hettige, Pablo Paradis, Cesy Zamarripa, and Zachary Yoder for being great co-workers and for being patient with me during long group meetings.

My deepest gratitude also goes to Dr. José Menéndez (Arizona State University) for carefully reading the draft of the Ge direct band gap manuscript, as well as for his detailed comments and for various calculations, which have been a relevant contribution to this work.

I would also like to express my gratitude to our collaborators at (or associated with) ELI Beamlines in the Czech Republic: Dr. Shirly Espinoza, Dr. Mateusz Rebarz, Dr. Steffen Richter (Linköping University), M.Sc. Oliver Herfurth (Universität Leipzig, now at: Active Fiber Systems GmbH), Dr. Rüdiger Schmidt-Grund (TU Ilmenau), Dr. Martin Zahradník, and Dr. Jakob Andreasson for their help and for providing the femtosecond pump-probe ellipsometry data for analysis. Many thanks as well to Dr. Christopher Stanton (University of Florida) for his help with the interpretation of the analysis results of the pump-probe ellipsometry data and coherent phonon oscillations, to Dr. David E. Aspnes (North Carolina State University) for his help with the reciprocal and linear filter analysis, to Dr. John A. Woollam for financial support, and to Dr. Tom E. Tiwald (J. A. Woollam Co.) for his help with the instrument and ellipsometry data.

Finally, I would like to thank my parents, my husband, and my friends for

being understanding and patient with me throughout the years. I find myself very lucky to have such wonderful people in my life, who have always been there for me.

This work was supported by the Air Force Office of Scientific Research under award number FA9550-20-1-0135, the National Science Foundation (NSF, No. DMR-1505172 and DMR-2119583), and the US Army (W911NF-16-1-0492).

VITA

- 2010-2014 B.S., Technical Physics, Johannes Kepler University,
Linz, Austria.
- 2014-2018 Dipl.-Ing., Technical Physics, Johannes Kepler University,
Linz, Austria.
- 2018-2020 M.S., Physics, New Mexico State University,
Las Cruces, New Mexico, USA.
- 2018-2020 Teaching Assistant, Department of Physics,
New Mexico State University.

PUBLICATIONS

C. Emminger, F. Abadizaman, N. S. Samarasingha, T. E. Tiwald, and S. Zollner, *Temperature dependent dielectric function and direct bandgap of Ge*, J. Vac. Sci. Technol. B **38**, 012202 (2020).

MANUSCRIPTS IN PROGRESS

C. Emminger, N. S. Samarasingha, M. Rivero Arias, F. Abadizaman, J. Menéndez, and S. Zollner, *Excitonic effects at the temperature-dependent direct band gap of Ge*, submitted to J. Appl. Phys. in November 2021.

C. Emminger, S. Espinoza, S. Richter, M. Rebarz, O. Herrfurth, M. Zahradník, R. Schmidt-Grund, J. Andreasson, and S. Zollner, *Transient critical point parameters of Ge and Si from femtosecond pump-probe ellipsometry*.

PRESENTATIONS

C. Emminger, S. Zollner, and J. Menéndez, *Dielectric function of Ge and related semiconductors near the direct band gap*, AFRL Workshop (virtual), Sept.14-15, 2020 (talk).

C. Emminger, S. Espinoza, S. Richter, M. Rebarz, O. Herrfurth, M. Zahradník, R. Schmidt-Grund, J. Andreasson, and S. Zollner, *Analysis of Femtosecond Pump-Probe Ellipsometry Data of Ge, Si, and InP*, 11th Workshop Ellipsometry, Steyr, Austria, Sept. 06-09, 2021 (talk).

C. Emminger, F. Abadizaman, N. Samarasingha, J. Menéndez, S. Espinoza, S. Richter, M. Rebarz, O. Herrfurth, M. Zahradník, R. Schmidt-Grund, J. Andreasson, and S. Zollner, *Analysis of temperature-dependent and time-resolved ellipsometry spectra of Ge*, Virtual IEEE Photonics Society 2021 Summer Topicals Meeting, July 19-21, 2021 (talk).

C. Emminger, F. Abadizaman, N. Samarasingha, J. Menéndez, S. Espinoza, S. Richter, M. Rebarz, O. Herrfurth, M. Zahradník, R. Schmidt-Grund, J. Andreasson, and S. Zollner, *Computational Analysis of Critical Points in Temperature Dependent and Time Resolved Ellipsometry Spectra of Ge Using Digital Filtering*, Virtual MRS Spring Meeting, April 17-23, 2021 (talk).

C. Emminger, F. Abadizaman, N. Samarasingha, J. Menéndez, S. Espinoza, S. Richter, M. Rebarz, O. Herrfurth, M. Zahradník, R. Schmidt-Grund, J. Andreasson, and S. Zollner, *Analysis of critical points in temperature dependent and time resolved ellipsometry spectra using digital filtering*, Virtual APS March Meeting, March 15-19, 2021 (talk).

C. Emminger, F. Abadizaman, N. Samarasingha, S. Espinoza, S. Richter, M. Rebarz, O. Herrfurth, R. Schmidt-Grund, J. Andreasson, S. Zollner, *Analysis of Critical Points in Ellipsometry Spectra Using Digital Filtering*, ELI Beamlines User Conference (virtual), Oct. 13, 2020 (talk).

C. Emminger, F. Abadizaman, N. Samarasingha, S. Zollner, *Accurate temperature-dependent optical constants for germanium near the direct band gap*, AFRL Workshop (virtual), Sept. 15, 2020. (talk).

F. Abadizaman, C. Emminger, S. Knight, M. Schubert, and S. Zollner, *Optical Hall Effect in the Multi-valley Semiconductor Te-doped GaSb*, AVS 66th International Symposium & Exhibition, Columbus, Ohio, Oct. 20-25, 2019 (talk).

C. Emminger, N. Samarasingha, F. Abadizaman, and S. Zollner, *Temperature Dependence of the Critical Point Parameters of the Direct Band Gap of Germanium*, 8th International Conference on Spectroscopic Ellipsometry, Barcelona, Spain, May 26-31, 2019 (talk).

F. Abadizaman, C. Emminger, S. Knight, M. Schubert, and S. Zollner, *Optical Hall Effect in Te-doped GaSb and undoped InAs*, 8th International Conference on Spectroscopic Ellipsometry, Barcelona, Spain, May 26-31, 2019 (poster).

C. Emminger, N. Samarasingha, F. Abadizaman, and S. Zollner, *Investigation of the Temperature Dependence of the Critical Points E_0 and $E_0 + \Delta_0$ of Bulk Ge*, DPG Spring Meeting, Regensburg, Germany, March 31 – April 5, 2019 (talk).

C. Emminger, N. Samarasingha, F. Abadizaman, and S. Zollner, *Analysis of the Critical Point Parameters of E_0 and $E_0 + \Delta_0$ of Bulk Ge*, APS March Meeting, Boston, Massachusetts, March 4-8, 2019 (talk).

R. A. Carrasco, C. Emminger, N. Samarasingha, F. Abadizaman, and S. Zollner, *Temperature dependent dielectric function and critical point comparison of bulk Ge and α -Sn on InSb*, AVS 65th International Symposium and Exhibition, Long Beach, California, Oct. 21-26, 2018 (talk).

C. Emminger, R. A. Carrasco, N. Samarasingha, F. Abadizaman, S. Zollner, *Temperature dependent dielectric function and critical points of bulk Ge compared to α -Sn on InSb*, IEEE Photonics Society 2018 Summer Topicals Meeting Series, Waikoloa, Hawaii, July 9-11, 2018 (talk).

C. Emminger, N. Samarasingha, F. Abadizaman, and S. Zollner, *Analysis of Critical Points in the Dielectric Function of Ge between 10 and 738 K*, NMAVS Symposium and Exhibition, Albuquerque, New Mexico, 22 May 2018 (talk).

C. Emminger, N. Samarasingha, F. Abadizaman, N. Fernando, and S. Zollner, *Temperature dependence of the dielectric function and analysis of critical point parameters of bulk Ge*, APS March Meeting, Los Angeles, California, March 5-9, 2018 (talk).

C. Emminger, N. Samarasingha, F. Abadizaman, N. Fernando, and S. Zollner, *Temperature dependence of the dielectric function and interband critical points of bulk Ge*, AVS 64th International Symposium & Exhibition, Tampa, Florida, Oct. 30 – Nov. 3, 2017 (talk).

C. Emminger, N. Samarasingha, F. Abadizaman, N. Fernando, and S. Zollner, *Temperature Dependence of the Dielectric Function of Bulk Ge*, NMAVS Symposium and Exhibition, Albuquerque, New Mexico, 16 May 2017 (talk).

C. Emminger, C. Reitböck, J.-P. Perin, K.-D. Bauer, A. Alejo-Molina, D. Stifter,

and K. Hingerl, *Advanced Model for Predicting Polarization Sensitive Second Harmonic Generation in Si(111)*, 18th International Conference on Solid Films and Surfaces, Chemnitz, Germany, Aug. 28 – Sept. 2, 2016 (poster).

ABSTRACT

ELLIPSOMETRY OF SEMICONDUCTORS UNDER THERMAL AND
LASER EXCITATION

BY

CAROLA EMMINGER, B.S., M.S.

Doctor of Philosophy

New Mexico State University

Las Cruces, New Mexico, 2021

Dr. Stefan Zollner, Chair

The temperature-dependent dielectric function of Ge from spectroscopic ellipsometry and the time-resolved pseudodielectric function of Ge and Si from femtosecond pump-probe ellipsometry are quantitatively analyzed in order to study how critical points are affected by temperature and ultrashort laser pulses. Using digital linear filter and reciprocal space analysis techniques, the second derivatives with respect to energy of the dielectric function are calculated and fitted with analytical lineshapes. For the direct band gap E_0 of Ge between 10 and 710 K,

the Hulthén-Tanguy theory is utilized in order to take into account excitonic effects. The agreement between the model and the data is remarkable, although the only significant adjustable parameters are the band gap energy and broadening. Using two- and zero-dimensional critical point lineshapes, the second derivatives of the transient pseudodielectric functions of Ge and Si are fitted, and resulting critical point parameters (threshold energy, lifetime broadening, excitonic phase angle, and amplitude) are presented as functions of time delay. Coherent acoustic phonon oscillations with a period of 11 ps are observed in the critical point parameters of Ge.

CONTENTS

LIST OF TABLES	xvi
LIST OF FIGURES	xxvi
1 INTRODUCTION	1
2 EXPERIMENTAL METHODS	4
2.1 Spectroscopic ellipsometry	4
2.1.1 Principle	4
2.1.2 Experimental challenges	7
2.2 Femtosecond pump-probe spectroscopic ellipsometry	17
3 THEORY	20
3.1 Interband transitions and critical points	20
3.2 Excitons	23
3.3 Strain-related energy shifts	26
4 EXCITONIC EFFECTS AT THE TEMPERATURE-DEPENDENT DIRECT BAND GAP OF GE	30
4.1 Introduction	31
4.2 Experiment	34
4.3 Hulthén-Tanguy model	36
4.4 Second derivatives through linear filtering	43

4.5	Fitting	46
4.6	Temperature dependence	49
4.7	Conclusion	56
4.8	Supplementary material	59
4.8.1	Fit results at higher temperatures	59
4.8.2	Broadening of the direct band gap	59
4.8.3	Screening parameter	65
4.8.4	Experiment	66
4.8.5	Second derivatives	71
5	TRANSIENT CRITICAL POINT PARAMETERS OF GE AND SI FROM FEMTOSECOND PUMP-PROBE ELLIPSOMETRY .	73
5.1	Introduction	74
5.2	Critical point analysis	75
5.3	Results and discussion	79
5.4	Summary	89
5.5	Supplementary material	91
5.5.1	Notes on experiment and data analysis	91
5.5.2	Coherent phonon oscillations	91
6	CONCLUSION	98
	Appendices	100
A.1	Digital linear filters	100

A.1.1	Second energy derivatives	102
A.2	Code	105
A.3	Fitting of the dielectric function with the Hulthén-Tanguy model	107
REFERENCES	116

LIST OF TABLES

4.1	Experimental parameters: Slit width (s), step size ($\Delta E'$), and native oxide layer thickness (d). An iris was installed at the exit window of the cryostat for measurements above 400 K. ΔE is the width of the linear filter used to calculate the second energy derivatives (see Sec. 4.4).	36
4.2	Parameters at 4.2 K, determined as explained in the text. Effective and reduced masses are given in units of m_0	42
4.3	Parameters E_a , E_b , and the effective phonon energy E_{ph} obtained from fitting Eq. (61) to the temperature dependent energy E_0 of the direct band gap for different analysis methods and models.	52
4.4	Parameters obtained by fitting Eq. (62) to the temperature dependent broadening, where $\gamma_0 = 0$, and the effective phonon energy was fixed to the value obtained from fitting the energy (see Tab. 4.3). Calculated values from Ref. 65 are listed for comparison.	53
4.5	Parameters in Eqs. (65)-(68) for Ge.	62
4.6	Estimated relaxation times in fs from Eqs. (65)-(68) for the direct band gap of Ge at 10, 80, 300, and 710 K.	63

4.7	Estimated lifetime broadenings in meV at 10, 80, 300, and 710 K obtained from the relaxation times in Tab. 4.6.	63
4.8	Parameters describing the temperature dependence of the broadening obtained by fitting Eq. (62) to the broadening between 10 and 300 K, where $\gamma_0 = 0$ was fixed, compared to values from the literature.	71
5.1	Material parameters of Ge and Si at room temperature.	82
5.2	Wavelength λ and refractive index n at the E_1 and $E_1 + \Delta_1$ critical points of Ge and E_1 of Si, along with the period T of coherent longitudinal acoustic phonon oscillations calculated from Eq. (74) and the penetration depth ζ	83
5.3	Parameters obtained from fitting Eq. (75) to the E_1 and $E_1 + \Delta_1$ shifts of Ge measured with the 800 nm pump pulse between 1 and 30 ps (Figs. 5.4 and 5.5).	85
5.4	Ratio $\sigma_{ii}^e/\sigma_{ii}^p$ of the electron and phonon contributions to stress.	87
5.5	Filter width ΔE and range of step size for the data sets of Ge and Si measured with $\lambda_{\text{pump}} = 800, 400, \text{ and } 267$ nm pump pulse wavelengths.	92

LIST OF FIGURES

2.1	Schematic image of an ellipsometry setup. The initially unpolarized light emitted from a white light source passes through a polarizer (and becomes linearly polarized), gets reflected from the surface of a sample, passes through an analyzer, and finally reaches a detector. Green arrows depict the polarization state of the light.	4
2.2	Picture of the V-VASE ellipsometer and the Janis ST-400 UHV cryostat used to measure the temperature-dependent dielectric function presented in chapter 4. Source: ellipsometry.nmsu.edu [Accessed: 18 November 2021].	8
2.3	Real part $\langle\epsilon_1\rangle$ and imaginary part $\langle\epsilon_2\rangle$ of the pseudodielectric function of bulk Ge before (Ge_2O layer thickness: 87 \AA) and after cleaning the sample (24 \AA) compared to the real (ϵ_1) and imaginary part (ϵ_2) of the dielectric function obtained from an oxide correction of $\langle\epsilon\rangle$ of the cleaned sample, as explained in the text.	10
2.4	Change of the thickness of the native oxide layer on top of bulk Ge with temperature. Figure reproduced from Ref. 6.	11

2.5	Change of the thickness of the native oxide layer on top of bulk Ge with time, obtained from several measurements at 10 K using various combinations of step sizes (0.5, 1, or 10 meV) and slit widths (0.5, 1, or 2 mm). Figure reproduced from Ref. 6.	12
2.6	Ellipsometric angles ψ and Δ of Ge measured at a temperature of 583 K using an iris attached to the outside of the exit window of the cryostat (solid) to suppress black body radiation compared to not using an iris (dashed). Figure reproduced from Ref. 6.	13
2.7	Imaginary part of the dielectric function of Ge at 300 K measured with spectroscopic ellipsometry using a step size of 10 meV and a maximum slit width of 1.9 mm [16] (squares) and a step size of 2 meV and slit width of 0.5 mm [6] (circles). The solid line represents a three-dimensional lineshape (imaginary part of the dielectric function defined in Eq. (15) for $\mu = -0.5$, $E_g = 0.8$ eV, $A = 2.0$, $\phi = 3\pi/2$, and $\Gamma = 0$).	14
2.8	Top: Baseline measurement using a xenon light source at 70° angle of incidence: Reflection off Ge sample in air (i.e. outside of the cryostat). Bottom: Depolarization of high-resolution measurements (0.4 meV step size, 0.4-0.5 mm slit width) on the same Ge sample inside the cryostat between 323 and 500 K. Vertical lines mark the peaks of the xenon light source.	16

2.9	Femtosecond pump-probe ellipsometry setup at ELI Beamlines, which was used to measure the data analyzed in chapter 5. The notation is as follows: beam splitter (BS), super-continuum generation (SCG), chopper (Ch), polarizer (P), sample (S), lens (L), rotating compensator (C_R), analyzer (A), second/third harmonic generation (SHG/THG), delay line (DL), charge-coupled device detector (CCD). Reproduced from Ref. 9 with the permission of AIP Publishing.	17
2.10	Schematic image of a pump-probe experiment on Ge. The red shaded area depicts the volume excited by the 800 nm pump pulse and the green shaded area shows the probed volume. The figure is not drawn to scale.	18
3.1	Left: Critical points in the spectrum of the pseudodielectric function of bulk Ge measured at 10 K (data taken from [6]). Right: Band structure of Ge showing interband transitions according to the critical points shown on the left-hand side. Modified figure from Ref. 21, p. 268.	21

- 3.2 Imaginary part of the dielectric function of several materials taken from [29] (squares) at room temperature compared to the Hulthén-Tanguy model [7] using different screening parameters: $g = 0.001$ (dashed), $g = 0.5$ (dotted), and $g = 100$ (dash-dotted). The data represented by small dots were measured at NMSU using an FTIR ellipsometer [30] (InSb) and a V-VASE ellipsometer [15] (Ge, see section 4.2). The solid lines represent the fits explained in section 4.2. 25
- 4.1 Real and imaginary parts of the terms in Eq. (35), defined in Eqs. (38)-(41), with $E_0 = 0.889$ eV (marked by the vertical line), $\gamma = 1$ meV, $R = 1.5$ meV, $A = 1.0$ eV^{-3/2}, and $g = 35$. The solid line represents the dielectric function as defined in Eq. (35), which is equivalent to the sum of the four terms f_1 - f_4 in Eqs. (38)-(41). For large g , $f_2=0$ 38
- 4.2 Natural logarithm of the Fourier coefficient amplitude C_n of the real (ϵ_1) and imaginary (ϵ_2) part of the dielectric function of Ge at 80 K, obtained as explained in the text. Symbols represent the Fourier transform of the EG filters for $M = 4$ and different ΔE . The vertical lines mark the onset of white noise for ϵ_1 (solid) and ϵ_2 (dashed), respectively. $\Delta E = 0.85$ meV for ϵ_1 and $\Delta E = 0.95$ meV for ϵ_2 are the best choices for this case. 44

4.3	Real (a) and imaginary (b) parts of the dielectric function and the corresponding second derivatives with respect to energy, (c) and (d), respectively, calculated from Eq. (70) at various temperatures. Solid lines represent the best fits to the data.	47
4.4	Like Fig. 4.3 for a temperatures of 690 K, where the solid line represents the best fit to the data and the dashed line shows the fit shifted by 8 meV towards lower energies.	49
4.5	Temperature dependence of the direct band gap energy obtained from the fits with Eq. (42) (\square), compared to the results by a reciprocal space analysis [6] (\triangle) and the results from Macfarlane <i>et al.</i> [56] (\times). Lines represent fits with Eq. (61).	50
4.6	Temperature dependence of the broadening obtained from the fits (\triangle), best fit to the data with Eq. (62) (dashed), filter widths used for the real part (∇) and imaginary part (\square), the instrumental resolution ($\gamma_{\text{inst.}}$), calculated width as explained in the text (\circ), and values from McLean and Paige [62, 63] (\times) and Aspnes [26] ($+$). The hh and lh broadening parameters are forced to have the same value.	51

4.7	Excitonic binding energies of the heavy-hole (R_{hh}) and light-hole (R_{lh}) excitons calculated from Eq. (44) versus energy E_0 of the direct band gap (which varies with temperature, as shown in Fig. 4.5). Closed symbols depict R_{hh} and R_{lh} calculated using ϵ_{st} from extrapolating ϵ_1 to lower energies (symbols in Fig. 4.8) and open symbols show R_{hh} and R_{lh} calculated using Eq. (63) (line in Fig. 4.8). Solid lines represent fits with $R(E_0) = b \cdot E_0^x$ and the dashed line represents the extension to lower energies of the curve shown in Fig. 5 of Ref. 67 with $R_h \propto E_0^{1.0(1)}$	54
4.8	Temperature dependence of the high-frequency dielectric constant ϵ_∞ of Ge obtained from the experimental data (symbols) compared with ϵ_∞ calculated from Eq. (63) (line) using the literature value [69] $\epsilon_\infty(T = 300 \text{ K}) = 16.2$	55
4.9	Like Fig. 4.3 for temperatures of 598, 639, 676, and 710 K.	60
4.10	Carrier density of intrinsic Ge as a function of temperature.	65
4.11	Screening parameter g of intrinsic Ge as a function of temperature, calculated from the carrier density shown in Fig. 4.10.	66
4.12	Like Fig. 4.6 including the broadening obtained from fits using the temperature-dependent screening parameter depicted in Fig. 4.11 (\blacktriangle).	67

4.13	Fit results at 710 K (solid) as shown in Fig. 4.9, i.e. $g = 35$, compared to the fit using $g = 0.26$ (dashed).	67
4.14	Imaginary (top) and real (bottom) part of the dielectric function for a broadening of $\gamma_{hh} = \gamma_{lh} = 0.77$ meV (dashed) and $\gamma_{hh} = \gamma_{lh} = 1.53$ meV (solid). Experimental data (symbols) at 10 K from Ref. 6.	69
4.15	Like Fig. 4.6 showing the low temperature range. The dashed line represents the fit with Eq. (62) to the broadening between 10 and 300 K. Fit parameters are given in Tab. 4.8.	70
4.16	Second derivatives of the real part of the dielectric function of Ge at 10 K (data from Ref. 6) obtained from the Savitzky-Golay (SG) method using a polynomial of third degree over $N = 10$ and $N = 11$ data points compared with the second derivatives from the EG filter method explained in Sec. 4.4, using a filter width of 1 meV. . . .	72
4.17	Same as Fig. 4.16 for the imaginary part of the dielectric function.	72
5.1	Second derivatives with respect to energy of the dielectric function in the region of E_1 and $E_1 + \Delta_1$ of Ge measured with an 800 nm pump pulse at different time delays before (-5 ps), at, and 100 ps after the pump pulse. Dashed lines represent the derivatives obtained as explained in the text. Solid lines represent the fits using two-dimensional lineshapes for E_1 and $E_1 + \Delta_1$	78

5.2	Temporal evolution of the critical point parameters of E_1 (solid) and $E_1 + \Delta_1$ (dashed) in Ge measured with 267 (purple), 400 (cyan), and 800 nm (orange).	80
5.3	Same as Fig. 5.2 for E_1 in Si.	80
5.4	Shift ΔE_1 (change of the E_1 energies) with time delay of Ge measured with the 800 nm pump pulse. The solid line represents a fit with Eq. (75). The first ($\Delta E_a(t)$) and second ($\Delta E_b(t)$) terms in Eq. (75) are represented by the dashed and dotted lines, respectively.	84
5.5	Same as Fig. 5.4 for $\Delta(E_1 + \Delta_1)$ (change of the $E_1 + \Delta_1$ energies).	84
5.6	Real (squares) and imaginary (dots) parts of the pseudodielectric function of Ge measured with an 800 nm pump pulse at probe energies of 2.06 eV (top) and 2.27 eV (bottom) close to E_1 and $E_1 + \Delta_1$ as functions of delay time along with the E_1 and $E_1 + \Delta_1$ critical point energies obtained from the second derivative analysis explained in the text.	93
5.7	Attenuation of the intensity inside the material of the probe and pump light beams in Ge (top) and Si (bottom). The probe intensities are calculated for the E_1 (dashed) and $E_1 + \Delta_1$ (dotted) wavelengths. The horizontal line marks the penetration depth $d = I_0/e$.	95

5.8	Damped oscillator $\cos(2\pi ft)e^{-t/\tau}$ with $\tau = \zeta/v_s$ and $f = 1/T$ calculated using the parameters given in Tab. 5.2 for E_1 (solid) and $E_1 + \Delta_1$ (dashed) of Ge and E_1 of Si (dotted), where $1/f = T$ is the period of coherent acoustic phonon oscillations.	96
5.9	Comparison of a damped oscillator $\cos(2\pi ft)e^{-t/\tau}$ where $f = 1/T$ and $\tau = \zeta/v_s$ with T and ζ listed in Tab. 5.2 compared to the E_1 energy of Si measured with a 400 nm pump pulse.	96
5.10	Oscillations in the E_1 and $E_1 + \Delta_1$ energies of Ge measured with an 800 nm-pump pulse as functions of delay time. The period of these oscillations is found to be between 100 and 150 fs.	97
A.1	Wavelength-to-energy conversion using Eq. (A4) for various $M = 0, \dots, 4$ (lines) of model data with noise (open circles). Solid circles represent the model data without noise.	101
A.2	Second derivative with respect to energy of the real part of the dielectric function of Ge measured at 500 K from Ref. 16 in the range of E_1 and $E_1 + \Delta_1$ (symbols). The second derivatives were obtained using Savitzky-Golay [37] (SG) coefficients using a polynomial of third degree over $N = 10$ data points. Lines represent the best fit to the data points using the second derivative of a 0D (dotted), 1D (dash-dotted), and 2D (solid) CP lineshape (Eq. (15)).	102

A.3	Same as Fig. A.2 but for the imaginary part of the dielectric function of Ge measured at 500 K from Ref. 16.	103
A.4	Second derivative with respect to energy of the real part of the dielectric function of Ge measured at 500 K from Ref. 16 in the range of E_1 and $E_1 + \Delta_1$. The second derivatives were obtained using Savitzky-Golay [37] (SG) coefficients using a polynomial of third degree over $N = 14$ data points (symbols) and the EG-filers defined in Eq. 70 (dotted line). Dashed and solid lines represent the best fit to the SG and EG derivatives using the second derivative of a 2D CP linsehape.	104
A.5	Same as Fig. A.2 but for the imaginary part of the dielectric function of Ge measured at 500 K from Ref. 16.	105

1 INTRODUCTION

Germanium (Ge) and silicon (Si) are group IV semiconductors with an indirect band gap of 0.66 eV [1] and 1.12 eV [2], respectively. Both semiconductors are important materials for optoelectronic devices and an in-depth understanding of the optical properties of these materials is essential for simulations and developments of mid-infrared devices, such as photodetectors and lasers [3].

One part of the present work is the investigation of the temperature-dependent dielectric function at the direct band gap of Ge measured by spectroscopic ellipsometry. Excitonic effects at the direct band gap of Ge are not negligible [4–6] and are taken into account by fitting a model based on the Tanguy solution of the Hulthén potential [7] to the dielectric function and its second derivative with respect to energy, from which the temperature dependence of the energy and lifetime broadening of the direct gap between 10 and 710 K is found. In principle, this model can also be applied to other semiconductors with similar band structures, such as InSb, GaAs, or $\text{Ge}_{1-x}\text{Sn}_x$ alloys, if non-parabolicity, warping, and screening are considered.

Pump-probe optical spectroscopy can provide insight into carrier dynamics and many-body effects in semiconductors [8]. The pseudodielectric function of Ge, Si, and InP has been measured with femtosecond pump-probe ellipsometry

by Espinoza *et al.* [9] using pump-pulse wavelengths of 266, 400, and 800 nm. To enhance the understanding of photoexcitation through the ultrafast laser pulse, a qualitative analysis of the data is indispensable.

A common method to analyze spectroscopic ellipsometry data is to fit an analytical lineshape to the second derivative of the dielectric function with respect to energy to obtain parameters (threshold energy, broadening, amplitude, and excitonic phase angle) that characterize the critical points which should be investigated. In this work, the critical point parameters of E_1 and $E_1 + \Delta_1$ of Ge and E_1 of Si from Ref. 9 are found as functions of time delay (before, at, and after the pump pulse). After a sharp increase or decrease of the critical point parameters at and shortly after the pump pulse, the parameters start to recover. In the case of Ge, coherent acoustic phonon (CAP) oscillations with a period of about 11 ps are observed in the parameters of E_1 and $E_1 + \Delta_1$ within the first 30 ps. It is important to understand the properties of CAP oscillations in order to distinguish them from other effects, such as band gap renormalization, Pauli blocking, or heating through the laser. An explanation based on theory [10] is attempted and is in reasonable agreement with the experimental results.

Structure of the thesis

The present thesis is organized in the following way. In chapter 2, the principle of spectroscopic ellipsometry is briefly explained, followed by a discussion of

experimental conditions and challenges, and a short introduction to femtosecond pump-probe ellipsometry in section 2.2. Chapter 3 comprises the physical background relevant for this work. Chapters 4 and 5 constitute the major part of my Ph.D. work. It should be noted that chapters 4 and 5 are the most recent versions of manuscripts, which are planned to be submitted for publication in scientific journals in the near future.

The second energy derivatives of the dielectric and pseudodielectric functions are computed based on the linear filter method introduced by Le *et al.* [11], which combines scale change, noise reduction, and derivatives. Details on the analysis procedure and the code which I wrote to analyze the data and their derivatives are provided in the appendix.

2 EXPERIMENTAL METHODS

2.1 Spectroscopic ellipsometry

2.1.1 Principle

Spectroscopic ellipsometry (SE) is a contact-free optical measurement technique which measures the change in the polarization of light reflected from the surface of a sample [12]. Figure 2.1 schematically shows an ellipsometry setup consisting of a light source, a polarizer, optional compensators, an analyzer, and a detector. These optical components can change the polarization state of the light which

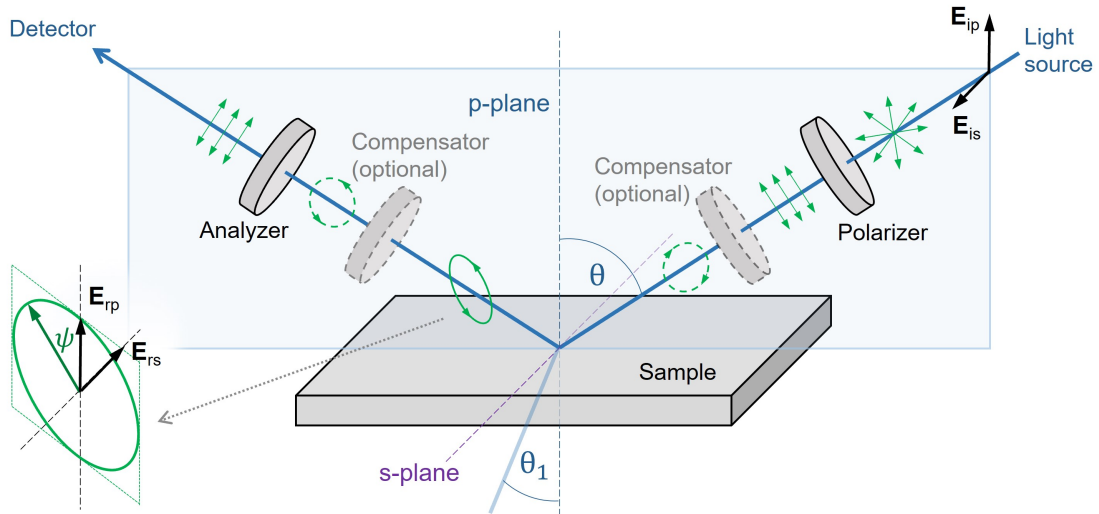


Figure 2.1: Schematic image of an ellipsometry setup. The initially unpolarized light emitted from a white light source passes through a polarizer (and becomes linearly polarized), gets reflected from the surface of a sample, passes through an analyzer, and finally reaches a detector. Green arrows depict the polarization state of the light.

passes through them. The polarization is defined by the *ellipsometric angles* ψ

and Δ , which are defined by the ratio ρ of the Fresnel reflection coefficients r_p and r_s [12]

$$\rho = \frac{r_p}{r_s} = \tan(\psi) e^{i\Delta}, \quad (1)$$

where p stands for parallel to and s for perpendicular to the plane of incidence (p-plane in Fig. 2.1). Expressed in terms of the incident (i) and reflected (r) p - and s -polarized electric fields (E_{ip} , E_{is} , E_{rp} , and E_{rs}), the Fresnel coefficients are defined as

$$r_p = \frac{E_{rp}}{E_{ip}} \quad (2)$$

and

$$r_s = \frac{E_{rs}}{E_{is}}, \quad (3)$$

which constitute the complex reflection coefficients of the sample for p -polarized and s -polarized light, respectively. The angle Δ is the phase difference between the p - and s -polarized electric field components, and ψ (shown in the image illustrating elliptically polarized light in Fig. 2.1) can be calculated as $\psi = \tan^{-1}(|r_p|/|r_s|)$ [12]. Equations (2) and (3) are related to the reflectance R_p and R_s which, for reflection on the surface of a sample in air (the refractive index of air is equal to one), are given by [12]

$$R_p = |r_p|^2 = \left| \frac{\tilde{n}^2 \cos \theta - \sqrt{\tilde{n}^2 - \sin^2 \theta}}{\tilde{n}^2 \cos \theta + \sqrt{\tilde{n}^2 - \sin^2 \theta}} \right|^2 \quad (4)$$

and

$$R_s = |r_s|^2 = \left| \frac{\cos \theta - \sqrt{\tilde{n}^2 - \sin^2 \theta}}{\cos \theta + \sqrt{\tilde{n}^2 - \sin^2 \theta}} \right|^2, \quad (5)$$

where θ is the angle of incidence of the light, and $\tilde{n} = n + i\kappa$ is the complex refractive index. The latter is related to the complex dielectric function via

$$\tilde{n} = n + i\kappa = \sqrt{\epsilon} = \sqrt{\epsilon_1 + i\epsilon_2}, \quad (6)$$

from which follows

$$\epsilon_1 = n^2 - \kappa^2 \quad (7)$$

and

$$\epsilon_2 = 2n\kappa, \quad (8)$$

or

$$n = \frac{1}{\sqrt{2}} \sqrt{\epsilon_1 + \sqrt{\epsilon_1^2 + \epsilon_2^2}}. \quad (9)$$

The imaginary part κ of the refractive index is also called *extinction coefficient* and can be calculated in a similar way

$$\kappa = \frac{1}{\sqrt{2}} \sqrt{-\epsilon_1 + \sqrt{\epsilon_1^2 + \epsilon_2^2}}. \quad (10)$$

The absorption coefficient α is proportional to κ and inversely proportional to the wavelength λ of the light

$$\alpha = \frac{4\pi\kappa}{\lambda}, \quad (11)$$

and is usually given in units of cm^{-1} . The intensity of the light inside a material can be calculated from the absorption coefficient via Beer's law

$$I(z) = I_0 e^{-\alpha z}, \quad (12)$$

where I_0 is the initial intensity and z is the direction of propagation of light. The penetration depth is defined as

$$\zeta = \frac{1}{\alpha}, \quad (13)$$

which gives the distance from the surface inside the material at which the intensity has decreased to I_0/e (e being Euler's number). The above equations outline some basic physics needed to understand ellipsometry. More details on the theoretical background can be found in many textbooks, for example in Refs. 12 and 13, and optical properties of solids are, for instance, described in [14].

2.1.2 Experimental challenges

The dielectric function of Ge at various temperatures, which is investigated in this work (chapter 4), was measured using the J. A. Woollam V-VASE ellipsometer [15] and the UHV cryostat shown in Fig. 2.2. While taking an ellipsometry measurement in air at room temperature is relatively easy to perform using a commercial ellipsometer (given that the sample quality and size are suitable), experiments below and above room temperature are more challenging. The temperature-dependent experiments discussed in this work were carried out in ultra-high vacuum (UHV) with the help of a Janis ST-400 UHV cryostat (see Fig. 2.2) at temperatures between liquid helium (4.2 K) and liquid nitrogen (77 K) temperature and up to 800 K. Depending on the sample material, the temperature at the sample surface deviates more or less from the set temperature below and

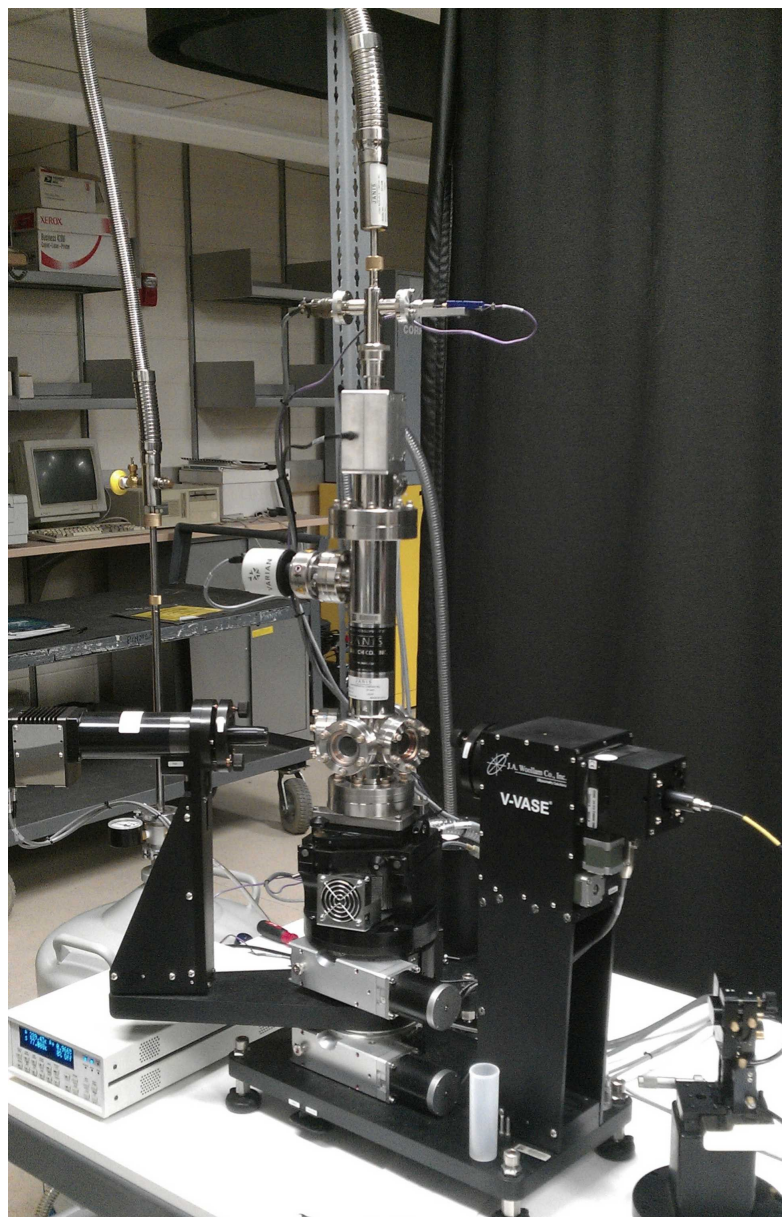


Figure 2.2: Picture of the V-VASE ellipsometer and the Janis ST-400 UHV cryostat used to measure the temperature-dependent dielectric function presented in chapter 4. Source: ellipsometry.nmsu.edu [Accessed: 18 November 2021].

above room temperature due to heat conduction. At the highest possible temperature of 800 K of the cryostat, the sample temperature was measured to be about 710-740 K for Ge (see chapter 4 and Refs. 6 and 16). In the case of single-crystalline Ni(100), for instance, a temperature of 770 K could be achieved [17] using the same instruments as shown in Fig. 2.2.

The surface of a bulk semiconductor oxidizes and forms an overlayer on top of the bulk substrate. To accurately measure the dielectric function, the Ge sample was cleaned with isopropanol alcohol in an ultrasonic bath for about 20 min to reduce the oxide layer. However, the oxide cannot be removed completely and its thickness increases over time when exposed to air. Details on the preparation of the sample are given in Sec. 4.2. To obtain the dielectric function of a material, one needs to take into account the native oxide layer which forms on the top of a bulk substrate, since ψ and Δ measured with SE give the dielectric function of material system, i.e. the substrate plus its oxide overlayer. This dielectric function is known as the *pseudodielectric* function and denoted as $\langle\epsilon\rangle = \langle\epsilon_1\rangle + i\langle\epsilon_2\rangle$. Figure 2.3 depicts $\langle\epsilon_1\rangle$ and $\langle\epsilon_2\rangle$ of bulk Ge before (blue curves) and after the cleaning the sample (red solid curves). Using the optical constant of GeO₂ from Ref. 18 and a parametric oscillator model [19], the pseudodielectric function can be corrected for the oxide layer, which is described in Refs. 18 and 20. A model consisting of two layers, a substrate and an overlayer, is fitted to the data. The thickness of the GeO₂-overlayer is fitted to the data below the direct band gap, while the

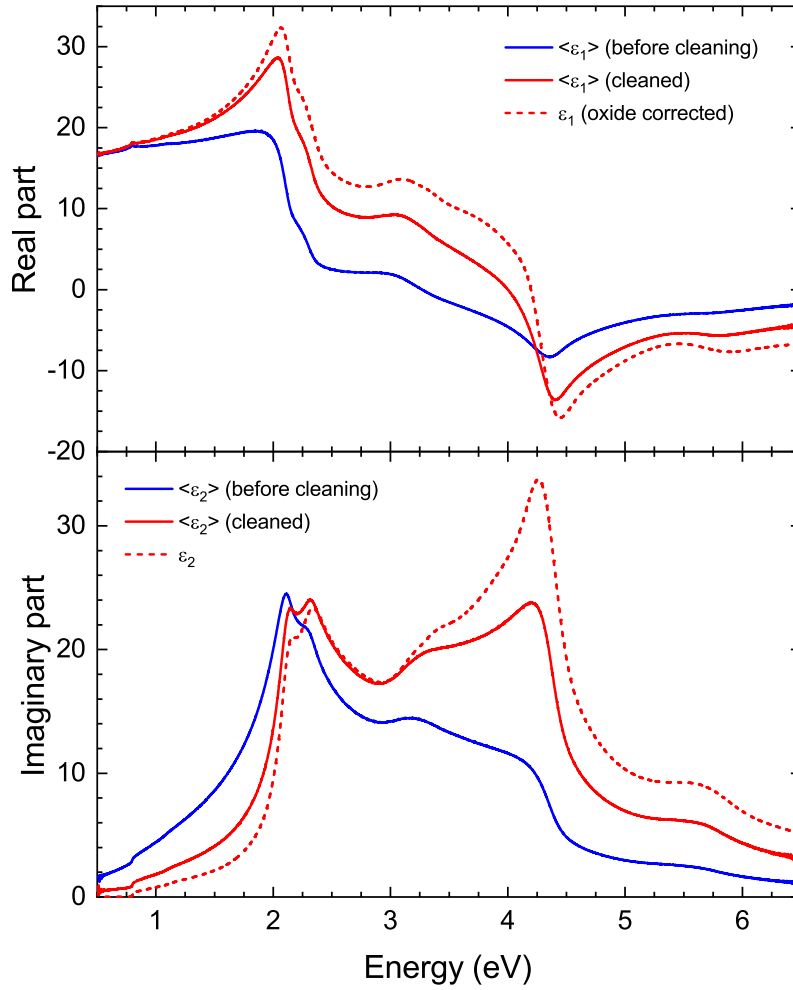


Figure 2.3: Real part $\langle \epsilon_1 \rangle$ and imaginary part $\langle \epsilon_2 \rangle$ of the pseudodielectric function of bulk Ge before (Ge_2O layer thickness: 87 Å) and after cleaning the sample (24 Å) compared to the real (ϵ_1) and imaginary part (ϵ_2) of the dielectric function obtained from an oxide correction of $\langle \epsilon \rangle$ of the cleaned sample, as explained in the text.

parameters of the substrate layer (the parameteric oscillator model) are fitted over the entire spectral range between 0.5 and 6.5 eV. The real and imaginary parts of the resulting dielectric function $\epsilon = \epsilon_1 + i\epsilon_2$ are represented by the dashed line in Fig. 2.3. The GeO_2 layer thickness changes with temperature due to the formation of ice at lower temperatures, and degassing and oxidation or an increase in surface roughness at higher temperatures [6], as illustrated in Fig. 2.4. At liquid

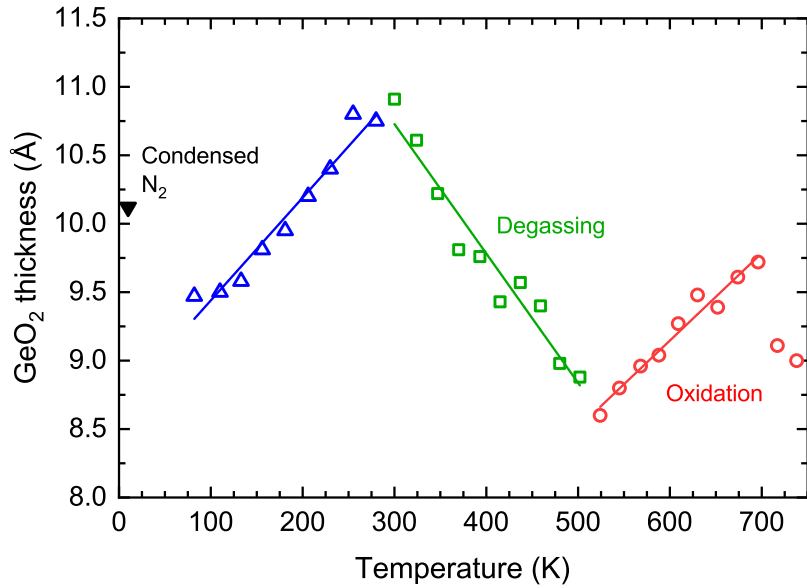


Figure 2.4: Change of the thickness of the native oxide layer on top of bulk Ge with temperature. Figure reproduced from Ref. 6.

helium temperature, it was observed that the thickness grows over time by about 0.04 \AA/h , which is shown in Fig. 2.5, probably as a result of oxygen or nitrogen condensation [6].

The thickness at the highest temperatures is less reliable due to the shift of the band gap to the lower (more noisy) spectral region, as mentioned in [6]. Noise

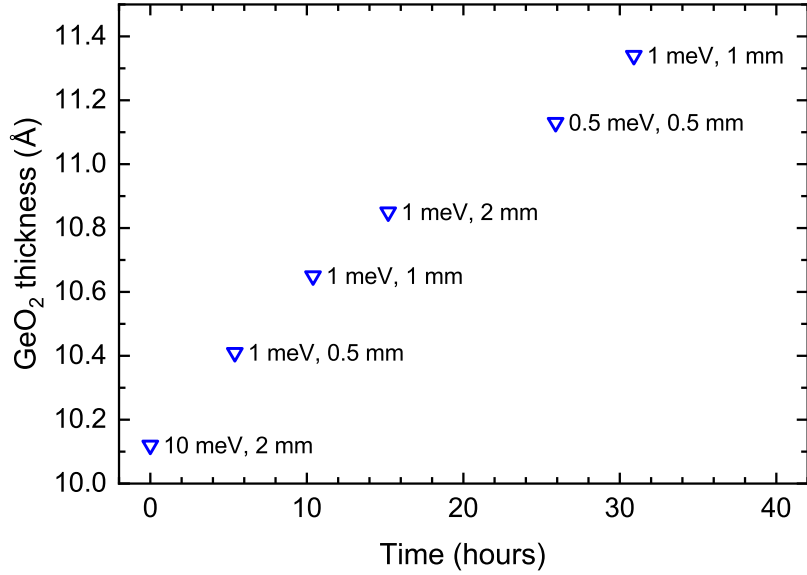


Figure 2.5: Change of the thickness of the native oxide layer on top of bulk Ge with time, obtained from several measurements at 10 K using various combinations of step sizes (0.5, 1, or 10 meV) and slit widths (0.5, 1, or 2 mm). Figure reproduced from Ref. 6.

also increases at higher temperatures due to black body radiation. This effect becomes significant at temperatures above 500 K and energies below 1 eV, but can be suppressed by installing an iris at the exit window of the cryostat [6].

Figure 2.6 demonstrates how the data at 583 K improve if an iris is used.

Figure 2.7 shows the imaginary part of the dielectric function at the direct band gap of Ge at room temperature, measured with different step sizes and slit widths [6, 16]. The spectral resolution of the monochromator depends on the grating used in this energy range, which has a dispersion of 4.6 nm/mm, and is calculated via $\gamma_{\text{inst.}} = hc\Delta\lambda/\lambda^2$, where h is Planck's constant, c is the speed of light, λ is the wavelength of the light, and $\Delta\lambda$ is equal to the dispersion times the

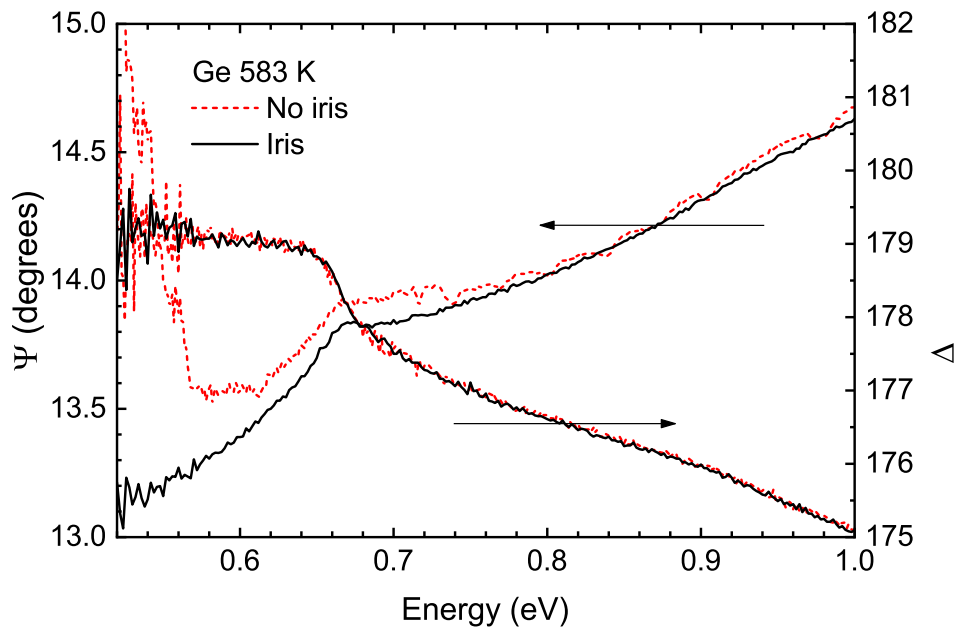


Figure 2.6: Ellipsometric angles ψ and Δ of Ge measured at a temperature of 583 K using an iris attached to the outside of the exit window of the cryostat (solid) to suppress black body radiation compared to not using an iris (dashed). Figure reproduced from Ref. 6.

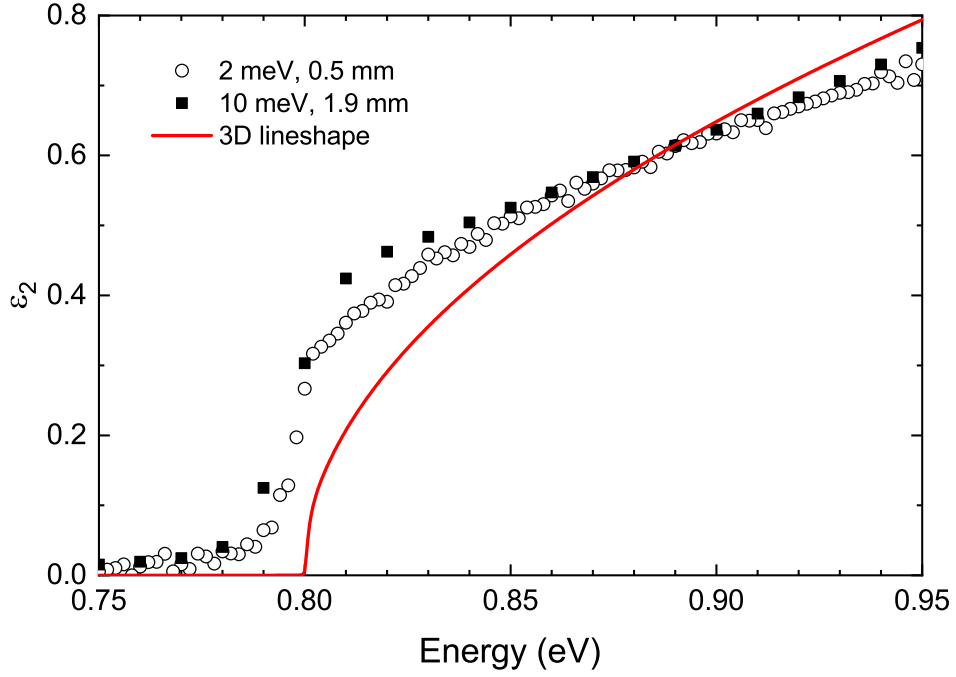


Figure 2.7: Imaginary part of the dielectric function of Ge at 300 K measured with spectroscopic ellipsometry using a step size of 10 meV and a maximum slit width of 1.9 mm [16] (squares) and a step size of 2 meV and slit width of 0.5 mm [6] (circles). The solid line represents a three-dimensional lineshape (imaginary part of the dielectric function defined in Eq. (15) for $\mu = -0.5$, $E_g = 0.8$ eV, $A = 2.0$, $\phi = 3\pi/2$, and $\Gamma = 0$).

slit width. Using a slit width of 0.5 mm (1.9 mm) at room temperature, where $E_0 = 0.8$ eV or $\lambda = 1550$ nm, gives an instrumental resolution of about 1.2 meV (4.5 meV).

As mentioned in section 4.5, spectral line peaks of the xenon light source used for the measurements with the V-VASE ellipsometer, have an effect on the dielectric function at the direct band gap at certain temperatures. The graph on the top in Fig. 2.8 shows the light from the xenon lamp at an angle of incidence of $\theta = 70^\circ$ reflected from the bulk Ge sample (“baseline” measurement). The peaks agree with the spectral lines characteristic for xenon. The graph on the bottom in Fig. 2.8 shows the depolarization of the ellipsometry measurements between 323 and 500 K (also at $\theta = 70^\circ$) on the same sample inside the cryostat (i.e. the same measurements which are studied in chapter 4). Although the band gap lies between about 0.8 and 0.9 eV at room temperature and below, the xenon lamp peaks do not seem to affect the analysis at these temperature. At temperatures between 370 and 450 K, on the other hand, the xenon lamp peaks affect the dielectric function and its second derivative, as discussed in section 4.5. For example, the real part of the dielectric function measured at a temperature of 391 K shows small distortions between 0.74 and 0.75 eV, as well as at about 0.77 eV, i.e. at the same energies as the xenon lamp peaks occur in the reflection measurement.

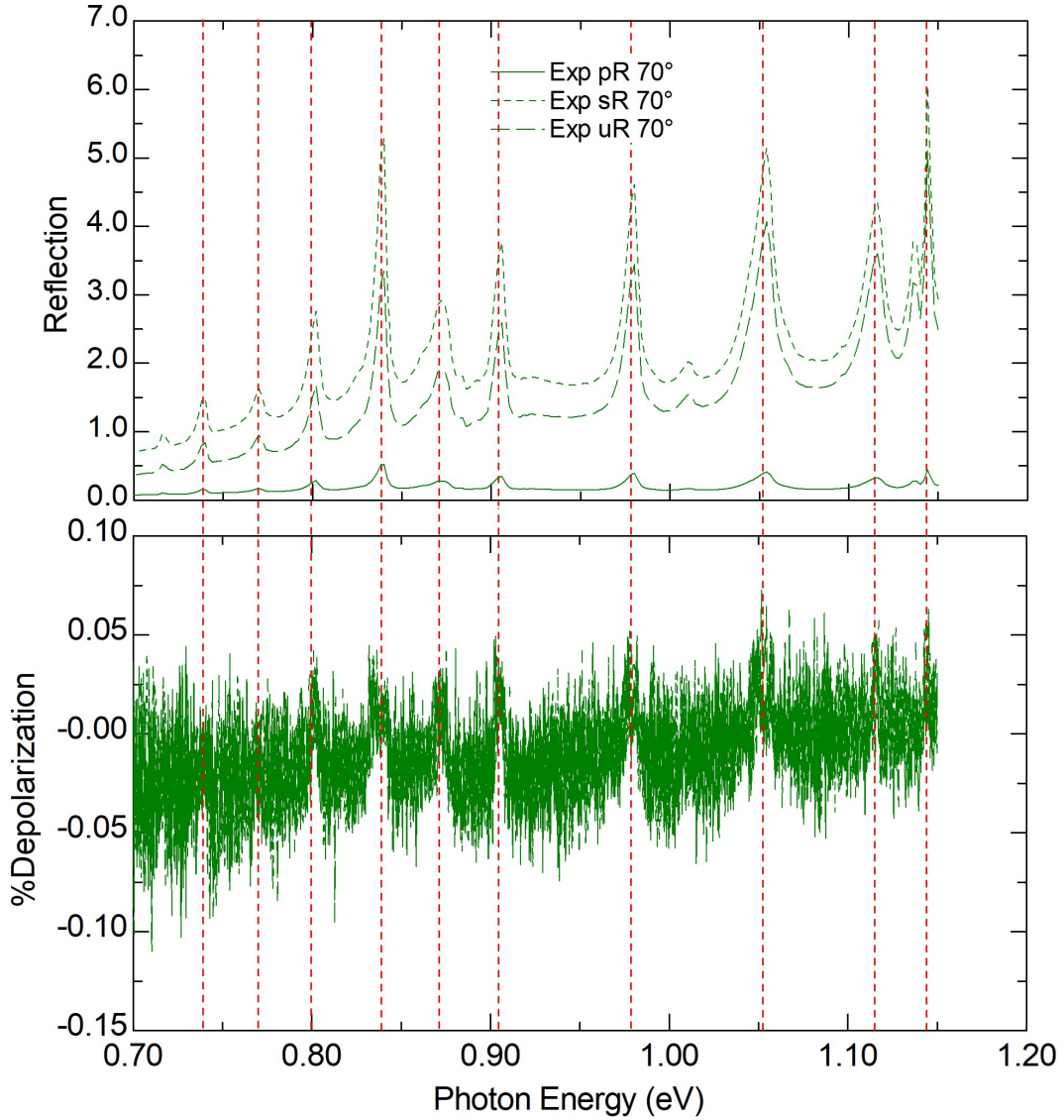


Figure 2.8: Top: Baseline measurement using a xenon light source at 70° angle of incidence: Reflection off Ge sample in air (i.e. outside of the cryostat). Bottom: Depolarization of high-resolution measurements (0.4 meV step size, 0.4-0.5 mm slit width) on the same Ge sample inside the cryostat between 323 and 500 K. Vertical lines mark the peaks of the xenon light source.

2.2 Femtosecond pump-probe spectroscopic ellipsometry

The femtosecond pump-probe SE setup is shown in Fig. 2.9. Details on the ex-

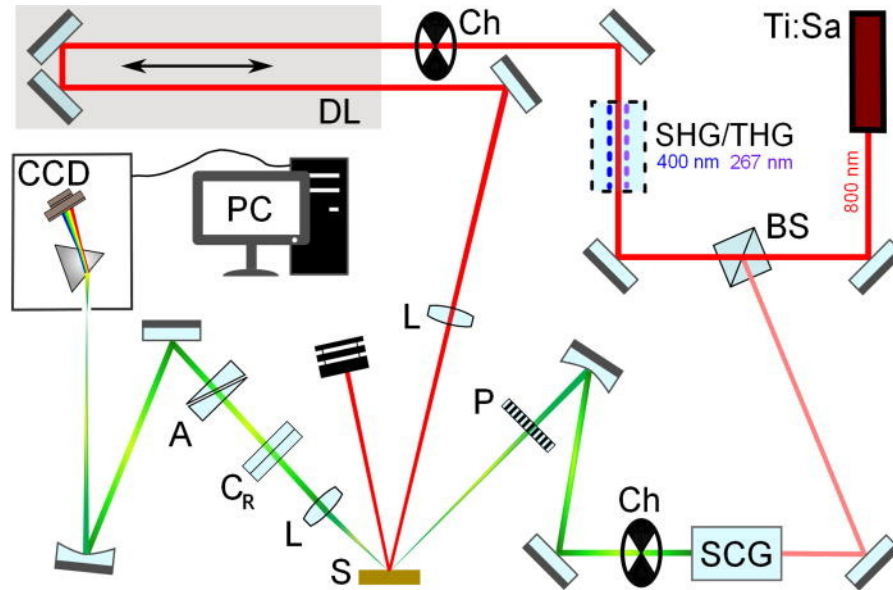


Figure 2.9: Femtosecond pump-probe ellipsometry setup at ELI Beamlines, which was used to measure the data analyzed in chapter 5. The notation is as follows: beam splitter (BS), super-continuum generation (SCG), chopper (Ch), polarizer (P), sample (S), lens (L), rotating compensator (C_R), analyzer (A), second/third harmonic generation (SHG/THG), delay line (DL), charge-coupled device detector (CCD). Reproduced from Ref. 9 with the permission of AIP Publishing.

perimental setup and conditions are given in Ref. 9. In this section, only a brief description of the experiment is provided.

A Ti:sapphire laser (Coherent Astrella) was used to produce 35 fs laser pump pulses of a wavelength of $\lambda_{\text{pump}} = 800$ nm with a repetition rate of 1 kHz. Through second- and third-harmonic generation (SHG and THG), the wavelength of the laser pulse can be changed from 800 to 400 or 267 nm. The red line represents

the laser beam, which is split into two parts by a beam splitter, such that a fraction of the laser beam is used for white light generation (super-continuum generation (SCG)) needed for the ellipsometry (probe) measurement. Following the green line, one can see the ellipsometry setup consisting of a polarizer, a rotating compensator, and an analyzer. The gray box illustrates the optical delay line, which is required for introducing a time delay between the pump and probe pulses [9].

The incident angles of the pump and probe beams were 45° and 60° (to the surface normal), respectively. Figure 2.10 illustrates schematically how the pump and probe pulses are reflected from the surface of a Ge sample, where the red shaded area inside the material (gray box) depicts the volume photoexcited by the 800 nm laser pulse (with a penetration depth of about $\zeta \approx 200$ nm). The

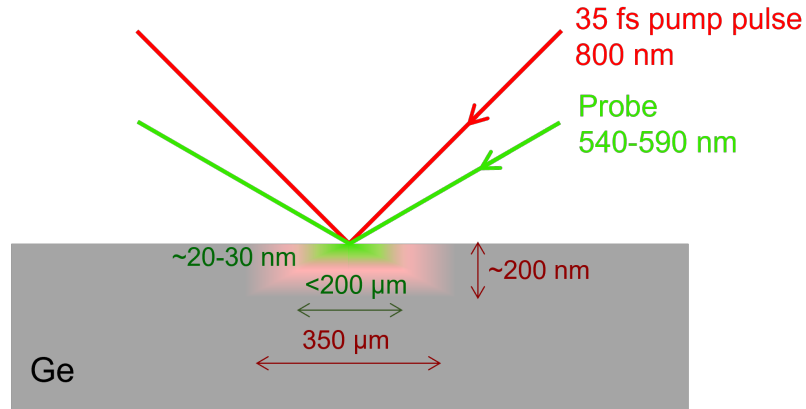


Figure 2.10: Schematic image of a pump-probe experiment on Ge. The red shaded area depicts the volume excited by the 800 nm pump pulse and the green shaded area shows the probed volume. The figure is not drawn to scale.

green shaded area, in turn, represents the *probed* volume. The penetration depth

in Ge for probe wavelengths between 540 and 590 nm (i.e. the range of the critical points E_1 and $E_1 + \Delta_1$) is much smaller than the one of the 800 nm pump pulse, and hence, the carrier concentration initiated by the laser pulse is assumed to be uniform throughout the probed volume in this particular case [9]. The situation looks different for 267 and 400 nm pump pulses, and also depends on the material (via the absorption coefficient defined in Eq. (11)), as shown in Fig. 5.7 for Ge and Si.

While in the temperature-dependent SE experiments the entire sample has a uniform temperature, the femtosecond laser pulse causes a localized increase in temperature at the surface of the sample, which contributes to strain inside the material [10]. Stress and strain with respect to their effect on the E_1 and $E_1 + \Delta_1$ critical points will be discussed in section 3.3, and laser-pulse induced strain as the source of coherent acoustic phonon oscillations is subject of the study in chapter 5.

3 THEORY

3.1 Interband transitions and critical points

A photon with an energy $E = \hbar\omega$ which is larger than the energy gap of a material can excite an electron in the valence band so that it occupies a state in the conduction band, leaving behind a hole in the valence band. Such a transition between two bands is called an *interband transition*, and is related to so-called *critical points* [21].

Critical points (CPs) occur as structures in the spectrum of the dielectric function, where the joint density of states (JDOS) shows singularities, known as Van Hove singularities [22]. The joint density of states is defined as [21]

$$D_j(E_{CV}) = \frac{1}{4\pi^3} \int \frac{dS_k}{|\Delta_{\mathbf{k}}(E_{CV})|}, \quad (14)$$

where S_k is the constant energy surface and $E_{CV} = E_C - E_V$ is the difference between conduction and valence band. Equation (14) shows a singularity if $|\Delta_{\mathbf{k}}(E_{CV})| = 0$, which is the case for the direct transitions shown in the band structure of Ge on the right-hand side of Fig. 3.1. The left-hand side of Fig. 3.1 depicts the pseudodielectric function $\langle\epsilon\rangle = \langle\epsilon_1\rangle + i\langle\epsilon_2\rangle$ of bulk Ge measured [16] with SE at a temperature of 10 K. The peaks shown in the spectra of $\langle\epsilon_1\rangle$ and $\langle\epsilon_2\rangle$ correspond to the critical points related to the interband transitions shown on the right-hand side of the same figure. The critical points of interest in this work

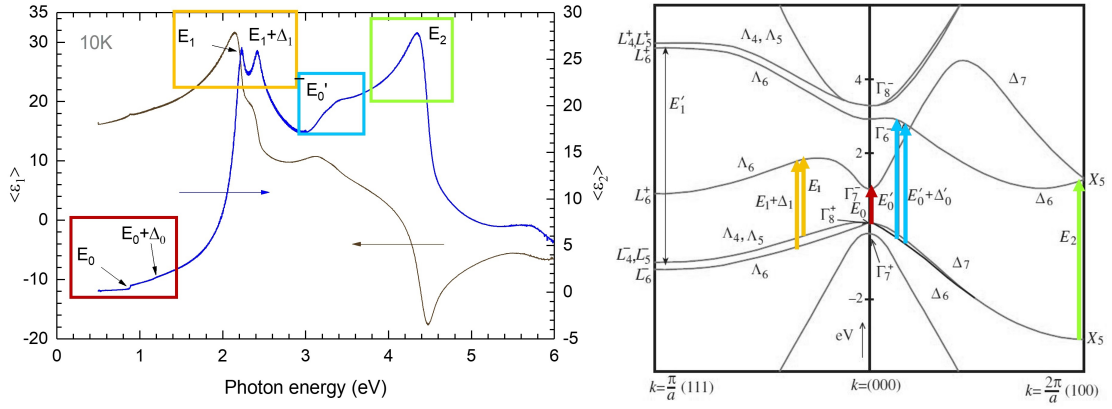


Figure 3.1: Left: Critical points in the spectrum of the pseudodielectric function of bulk Ge measured at 10 K (data taken from [6]). Right: Band structure of Ge showing interband transitions according to the critical points shown on the left-hand side. Modified figure from Ref. 21, p. 268.

are the direct band gap E_0 (interband transition at the zone center, where $k = 0$ (Γ -point)), and E_1 and $E_1 + \Delta_1$ (Δ_1 denotes the spin-orbit splitting) which result from interband transitions along the Λ -direction (where the bands are parallel) close to the L -point. It should be mentioned that instead of E_0' and $E_0' + \Delta_0'$, a single critical point \bar{E}_0' is denoted since the two critical points cannot really be distinguished [23].

The lineshape of CPs in the dielectric function $\epsilon(E)$ can be defined as [24, 25]

$$\epsilon(E) = B - \frac{Ae^{i\phi}}{(E - E_g + i\Gamma)^\mu}, \quad (15)$$

where A is the amplitude, E_g is the threshold energy, Γ is the broadening, B is a non-resonant background, and the phase angle ϕ accounts for excitonic effects via mixing of lineshapes [21]. The exponent μ in Eq. (15) defines the *dimension* of a critical point in the following way: $\mu = 1$ for a zero-dimensional (0D)

(or excitonic) lineshape, $\mu = 0.5$ for a one-dimensional (1D), $\mu = 0$ for a two-dimensional (2D), and $\mu = -0.5$ for a three-dimensional (3D) lineshape [24, 25]. Critical points, and hence the parameters that describe their lineshape, depend on temperature, doping, and pressure [21]. The temperature dependence of CPs in many semiconductor materials is well known. In Ge, for example, the energies redshift with increasing temperature, while the broadenings increase, the excitonic phase angles decrease, and the amplitudes remain constant, i.e. they are independent of temperature [23].

The imaginary part of the dielectric function is related to the absorption of the material (via Eqs. (8) and (11)). Below the fundamental band gap, the absorption is zero. Ge is an indirect semiconductor, that means that the valence band maximum and conduction band minimum are not at the same point in reciprocal space. The maximum of the valence band is at the Γ -point, while the minimum of the conduction band is located at L (see Fig. 3.1). In principle, the onset of absorption shows a square-root like dependence on energy, i.e. $\alpha \propto (E - E_g)^{1/2}$, or a 3D lineshape as defined in Eq. (15) for $\mu = -0.5$ [21]. However, in the case of Ge, excitonic effects at E_0 are present and clearly impact the lineshape [6]. A 3D lineshape is compared to the real part of the dielectric function of Ge at E_0 in Fig. 2.7. Even at room temperature, where excitonic effects are small compared to cryogenic temperatures, a 3D lineshape does not describe the data well. The agreement between the data and a lineshape considering excitonic effects, such

as the Hulthén-Tanguy model [7], is significantly better, which can be seen in Fig. 4.3. The role of excitons will be further discussed in the next section and in chapter 4.

3.2 Excitons

As mentioned above, when a photon is absorbed in a semiconductor or insulator, an electron is excited to the conduction band and a hole is created in the valence band. These two carriers are attracted by Coulomb interaction and form a bound pair, which is called an *exciton* [21]. The binding energy of an exciton is given by [14]

$$E_n = -\frac{\mu_h}{m_0} \frac{1}{\epsilon_r^2} \frac{R_H}{n^2}, \quad (16)$$

where n is the principle quantum number (not to be confused with the refractive index), $R_H = 13.6$ eV is the Rydberg energy of the hydrogen atom, m_0 is the free electron mass, μ_h is the reduced mass of the electron and hole, and ϵ_r is the dielectric constant. The orbital radius is proportional to the Bohr radius a_H of the hydrogen atom:

$$r_n = \frac{m_0}{\mu_h} \epsilon_r n^2 a_H. \quad (17)$$

Bound excitons appear as sharp peaks in the absorption spectrum below the band edge, and unbound excitons enhance the absorption above the band gap (exciton continuum) [21]. Two basic types of excitons are distinguished: Wannier-Mott (or free) excitons, and Frenkel (or tightly bound) excitons. The difference between

these two types is defined by their binding energy and orbital radius. Wannier-Mott excitons, which are mainly observed in semiconductors, have exciton binding energies of about 0.01 eV, while Frenkel excitons have binding energy of about 0.1-1 eV [14]. In the case of Ge, the excitonic binding energy is on the order of 1-2 meV [26].

Excitonic effects are considered by the theory established by Elliott [27] and Tanguy [7, 28]. The Tanguy model for a Hulthén potential takes into account excitonic effects and screening and can, in principle, be applied to various materials. Figure 3.2 shows the model for InSb, InAs, InP, and GaAs compared to data taken from data bases [29], and Ge measured as explained in chapter 4. The data set of InSb represented by small dots was measured with an FTIR ellipsometer [30]. The model is shown for different screening parameters: $g = 0.001$ (equivalent to $g \rightarrow 0$, i.e. maximum screening), $g = 0.5$ (dotted), and $g = 100$ (equivalent to $g \rightarrow \infty$, i.e. screening switched off) [7]. The agreement between theory and experiment can probably be improved by considering non-parabolicity and warping, and using suitable screening parameters, which should be addressed in future work. In chapter 4, the model is applied to the temperature-dependent band gap of Ge.

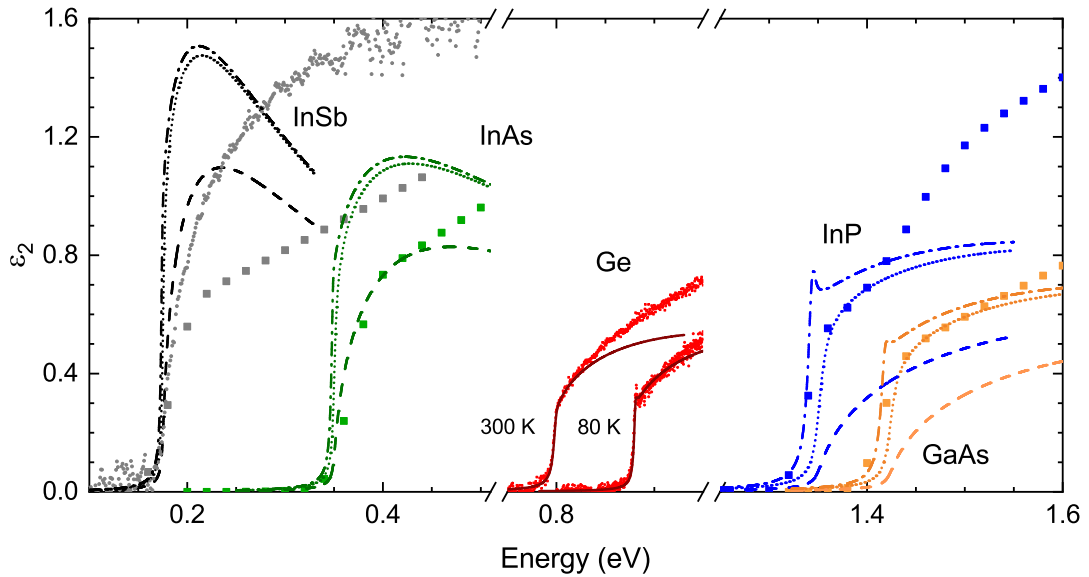


Figure 3.2: Imaginary part of the dielectric function of several materials taken from [29] (squares) at room temperature compared to the Hulthén-Tanguy model [7] using different screening parameters: $g = 0.001$ (dashed), $g = 0.5$ (dotted), and $g = 100$ (dash-dotted). The data represented by small dots were measured at NMSU using an FTIR ellipsometer [30] (InSb) and a V-VASE ellipsometer [15] (Ge, see section 4.2). The solid lines represent the fits explained in section 4.2.

3.3 Strain-related energy shifts

An ultrafast laser pulse can induce strain in a material [10, 31], which in turn affects the dielectric function since critical points depend on strain [20, 32, 33]. In light of this, some equations and relations which can be used to estimate the E_1 and $E_1 + \Delta_1$ CP energy shifts due to strain are summarized in this section.

Stress $\hat{\sigma}$ and strain $\hat{\epsilon}$ are second-rank tensors and related to one another via the elastic compliance \hat{S} , which is a fourth-rank tensor [34]:

$$\epsilon_{ij} = \sum_{kl} S_{ijkl} \sigma_{kl}. \quad (18)$$

While second-rank tensors can be expressed as 3×3 matrices, a fourth-rank tensor has $9 \times 9 = 81$ components. However, the elastic compliance can be reduced to a 6×6 matrix (this is explained, for example, in Sec. 3.4 of Ref. 35) and its form depends on the space group of the material. For Ge and Si (O_h -group), the elastic compliance is [35]

$$\hat{S} = \begin{pmatrix} S_{11} & S_{12} & S_{12} & 0 & 0 & 0 \\ S_{21} & S_{11} & S_{12} & 0 & 0 & 0 \\ S_{21} & S_{21} & S_{11} & 0 & 0 & 0 \\ 0 & 0 & 0 & S_{44} & 0 & 0 \\ 0 & 0 & 0 & 0 & S_{44} & 0 \\ 0 & 0 & 0 & 0 & 0 & S_{44} \end{pmatrix}. \quad (19)$$

Thomsen *et al.* [10] assume for their picosecond pump-probe experiments that the stress only depends on z . Hence, the only non-zero component of the strain tensor is ϵ_{33} . In terms of the definition given by Eq. (18), this component can be

expressed as

$$\begin{aligned}\epsilon_{33} = \sum_{kl} S_{33kl} \sigma_{kl} = & S_{3311} \sigma_{11} + S_{3312} \sigma_{12} + S_{3313} \sigma_{13} \\ & + S_{3321} \sigma_{21} + S_{3322} \sigma_{22} + S_{3323} \sigma_{23} \\ & + S_{3331} \sigma_{31} + S_{3332} \sigma_{32} + S_{3333} \sigma_{33}.\end{aligned}\quad (20)$$

Using the convention in Tab. 3.6 in Ref. 35, one gets

$$\begin{aligned}\epsilon_3 = \sum_{kl} S_{3kl} \sigma_{kl} = & S_{31} \sigma_1 + S_{36} \sigma_6 + S_{35} \sigma_5 \\ & + S_{36} \sigma_6 + S_{32} \sigma_2 + S_{34} \sigma_4 \\ & + S_{35} \sigma_5 + S_{34} \sigma_4 + S_{33} \sigma_3,\end{aligned}\quad (21)$$

which can be reduced using Eq. (19) to

$$\epsilon_3 = S_{21}(\sigma_1 + \sigma_2) + S_{11} \sigma_3. \quad (22)$$

Setting $\sigma_1 = \sigma_2 = \sigma_3 = \sigma$ in Eq. (22) leads to

$$\epsilon_3 = (S_{11} + 2S_{12})\sigma. \quad (23)$$

Stress is given in units of N/m² and strain is unitless, so the components of \hat{S} must be in m²/N. Similar to Eq. (18), one can write

$$\sigma_{ij} = \sum_{kl} C_{ijkl} \epsilon_{kl}, \quad (24)$$

where $C_{ijkl} = \hat{C}$ is the fourth-rank stiffness tensor. Relations between the components of the compliance and stiffness tensors are as follows [21]:

$$C_{44} = \frac{1}{S_{44}}, \quad (25)$$

$$C_{11} - C_{12} = \frac{1}{S_{11} - S_{12}}, \quad (26)$$

and

$$C_{11} + 2C_{12} = \frac{1}{S_{11} + 2S_{12}}. \quad (27)$$

Stiffness constants are listed, for example, in Tab. 3.6a in Ref. 21 for several materials. Using $C_{11} = 1.285 \times 10^7$ N/cm², $C_{12} = 0.483 \times 10^7$ N/cm², and $C_{44} = 0.680 \times 10^7$ N/cm² for Ge [21], one can calculate

$$S_{11} + 2S_{12} = \frac{1}{C_{11} + 2C_{12}} = 0.444 \frac{\text{cm}^2}{\text{N}}. \quad (28)$$

The shifts of the E_1 and $E_1 + \Delta_1$ critical point energies due to strain are defined in the following way [36]

$$E_1 = E_1^0 + \frac{\Delta_1}{2} + \Delta E_H - \sqrt{\frac{(\Delta_1)^2}{4} + (\Delta E_S)^2} \quad (29)$$

$$E_1 + \Delta_1 = E_1^0 + \frac{\Delta_1}{2} + \Delta E_H + \sqrt{\frac{(\Delta_1)^2}{4} + (\Delta E_S)^2}, \quad (30)$$

where E_1^0 is the E_1 energy of the unstrained material, and ΔE_H and ΔE_S are the hydrostatic and shear shifts, respectively, given by [36]

$$\Delta E_H = \sqrt{3}D_1^1\epsilon_H \quad (31)$$

and

$$\Delta E_S = \sqrt{6}D_3^3\epsilon_S. \quad (32)$$

D_1^1 and D_3^3 are the hydrostatic and shear deformation potentials. The hydrostatic strain ϵ_H and shear strain ϵ_S depend on the in-plane (ϵ_{\parallel}) and out-of-plane (ϵ_{\perp}) strain [36]:

$$\epsilon_H = \frac{\epsilon_{\perp} + 2\epsilon_{\parallel}}{3} \quad (33)$$

and

$$\epsilon_S = \frac{\epsilon_{\perp} - \epsilon_{\parallel}}{3}. \quad (34)$$

These equations are used in chapter 5 to estimate the shifts ΔE_1 and $\Delta(E_1 + \Delta_1)$ of Ge due to the strain caused by the femtosecond laser pulse in the time-resolved SE experiments.

4 EXCITONIC EFFECTS AT THE TEMPERATURE-DEPENDENT DIRECT BAND GAP OF GE

This manuscript was submitted to the Journal of Applied Physics in November 2021.

Carola Emminger,^{1,2} Nuwanjula S. Samarasingha,¹ Melissa Rivero Arias,¹ Farzin Abadizaman,² José Menéndez,³ and Stefan Zollner¹

¹*Department of Physics, New Mexico State University, Las Cruces, NM 88003-8001, USA*

²*Department of Condensed Matter Physics, Masaryk University, 61137 Brno, Czech Republic*

³*Department of Physics, Arizona State University, Tempe, AZ 85287-1504, USA*

Abstract

The temperature dependence of the complex dielectric function $\epsilon_1 + i\epsilon_2$ of bulk Ge near the direct band gap was measured with spectroscopic ellipsometry at temperatures between 10 and 710 K. Second derivatives of the dielectric function with respect to energy are obtained using a digital linear filter method. A model that incorporates excitonic effects using the Tanguy model for the Hulthén potential [C. Tanguy, Phys. Rev. B 60, 10660 (1999)] was used to fit the dielectric func-

tion and its second derivatives simultaneously. Using $k \cdot p$ theory and literature values for effective masses, remarkable agreement with experiment is obtained up to room temperature using the direct band gap and its broadening as the only adjustable parameters.

4.1 Introduction

Photo-excited electron-hole pairs in semiconductors form excitonic bound states, because the negatively charged electron and the positively charged hole are attracted to each other by the Coulomb force, similar to a hydrogen atom. The Bohr model gives a reasonable description of excitonic effects in semiconductors, as long as the effective masses of electrons and holes replace the masses of the proton and free electron, respectively, and the electrostatic screening is taken into account using the static dielectric constant. This electron-hole interaction not only results in discrete excitonic peaks below the band gap. It also leads to the so-called Sommerfeld enhancement of the absorption above the band gap [21].

While the physics of excitonic effects has been understood for decades [7, 27, 28], a quantitative comparison of these theories with experimental data for the dielectric function of semiconductors near the direct band gap E_0 has never been attempted. The goal of this work is to fit the dielectric function (and its second derivative) of Ge near E_0 from 10 to 710 K with only two adjustable parameters, the band gap energy and the broadening at each temperature. Our model will have

important applications for optoelectronic devices such as detectors and lasers. It can be applied not only to Ge, but also to other materials, such as GaAs, InSb, or germanium-tin alloys.

In a recent publication [6], we presented results on the temperature dependence of the direct band gap energy and broadening of bulk Ge, obtained from spectroscopic ellipsometry (SE). The E_0 energy was determined by a Fourier or reciprocal space [42] (RS) analysis, without assuming a specific lineshape, as well as by fitting a three-dimensional (3D) standard analytical lineshape [24,25] to the numerically calculated [37] second derivatives (SD) with respect to energy, and by applying a parametric semiconductor model [19]. However, the assumption of a 3D lineshape does not deliver a satisfactory description of the absorption edge of Ge due to the presence of excitonic effects [38,39]. An analytical expression for optical absorption by excitons was published by Elliott [27] and the theory was expanded to the complex dielectric function by Tanguy [28]. The bare excitonic Coulomb interaction in semiconductor materials can be screened by mobile carriers, and this leads to a Yukawa-like potential for which there are no analytical solutions to the excitonic problem. However, it has been shown that a remarkably accurate substitution for the Yukawa interaction is the Hulthén potential [40], for which Tanguy [7] has found analytical expressions for the complex dielectric function. In the limit of negligible screening, applicable to intrinsic Ge at room temperature and below, the dielectric function for the Hulthén potential becomes

identical to the dielectric function found by Tanguy for the bare Coulomb potential. At the highest temperatures in our experiments, however, the intrinsic carrier concentration increases by several orders of magnitude to values comparable to the critical Mott concentration [41] and therefore screening effects may be substantial. Accordingly, we use the Tanguy solution for the Hulthén potential to fit the dielectric function and its second derivative. The latter is obtained using a digital linear filter method [11, 43, 44] based on extended Gauss functions [45, 46].

The Hulthén-Tanguy model depends on the band gap energy, a Lorentzian broadening parameter, the exciton binding energy, an amplitude, a momentum matrix element, and a screening parameter. The amplitude, momentum matrix element, and excitonic binding energy can be obtained from $k \cdot p$ theory and fit to the band structure. The screening parameter is computed from a standard expression for the Thomas-Fermi screening wave vectors, following a prescription from Ref. 5. This leaves only two adjustable parameters for the Hulthén model: energy and broadening of the direct gap. We add a Sellmeier term with two additional adjustable parameters to consider contributions from critical points at higher energies to the real part of the dielectric function. We simply combine the heavy-hole (hh) and light-hole (lh) excitonic dielectric functions as if they were additive. This is not strictly correct but it has been shown to be a good approximation [5, 47].

Recent work [5] on phonon-assisted indirect absorption in Ge shows that this

absorption is strongly resonant at the direct band gap. A satisfactory theory for photon energies above the direct gap is not available at this time, and one cannot rule out a significant contribution in a range that was traditionally believed to be accounted mainly by direct transitions. Unfortunately, previous fits of the dielectric function in this range relied on adjustable amplitude parameters that are not well described by theory and on the introduction of phase factors that account for excitonic effects very indirectly. Due to the ad-hoc character of the parameters, the issue of whether the above gap absorption is truly dominated by direct transitions could not be addressed. The new model that we present in this paper treats excitonic effects explicitly and relies on known material parameters to calculate those “amplitudes”. The only significant adjustable parameters are the band gap energy and its broadening, and therefore any deviations between our fits and the experimental data might be related to the possible contribution of phonon-assisted processes.

4.2 Experiment

The dielectric function in the region of the direct band gap of a commercially obtained undoped bulk Ge sample with (100) surface orientation was measured between 80 and 710 K using a J. A. Woollam VASE ellipsometer [15] with a xenon light source (190 nm - 2 μm) and a Janis ST-400 UHV cryostat. The Ge wafer was undoped with a resistivity higher than 50 Ωcm , which indicates an electron

or hole concentration no higher than 10^{14} cm^{-3} [48].

We used liquid nitrogen to cool the system for the measurements between 80 K and room temperature. The sample was cleaned in an ultrasonic bath in isopropanol for 20 min, followed by an ultrasonic bath in ultrapure water for another 20 min, which reduced the native oxide layer thickness from 4 nm to about 1 nm. After the clean, the sample was immediately mounted into the UHV cryostat and heated up to 635 K for about eight hours for degassing and to stabilize the native oxide layer. At temperatures $T \geq 391$ K, we installed an iris at the exit window of the cryostat to suppress effects due to black body radiation, as illustrated in Fig. S4 in Ref. 6. To resolve the narrow structure of the excitonic peak, we used smaller step sizes (0.2-0.4 meV) than in our previous work [6]. A slit width between 300 and 1700 μm was chosen for our J. A. Woollam Co. HS-190 monochromator in order to achieve an instrumental resolution of about 1-2.5 meV and a satisfactory signal-to-noise ratio at each temperature.

Experimental parameters at the various temperatures are listed in Tab. 4.1. We also analyze the data set from Ref. 6 measured at 10 K with a step size of 0.5 meV and slit width of 500 μm .

A two-layer model (substrate+native oxide layer) was used to perform an oxide correction of the pseudodielectric function and to extract the dielectric function, as explained elsewhere [18,20]. The thickness of the native oxide layer varied between 12-13 Å at and below room temperature and 7-11 Å at higher temperatures.

Table 4.1: Experimental parameters: Slit width (s), step size ($\Delta E'$), and native oxide layer thickness (d). An iris was installed at the exit window of the cryostat for measurements above 400 K. ΔE is the width of the linear filter used to calculate the second energy derivatives (see Sec. 4.4).

Temperature	s (μm)	$\Delta E'$ (meV)	d (\AA)	Iris	ΔE (meV)
10 K ^a	500	0.5	11	No	1.0
80-300 K	400	0.4	12-13	No	0.9-1.6
323-391 K	400	0.4	9-11	No	1.8-4.0
412-436 K	500	0.4	9	Yes	3.5
458-479 K	900	0.4	8	Yes	3.5-4.0
500-542 K	1000	0.4	8	Yes	4.0-4.5
559 K	800	0.4	8	Yes	5.0
578-676 K	1500	0.4	8	Yes	5.0-7.0
690-710 K	1700	0.4	7-8	Yes	8.0

^aRef. 6

4.3 Hulthén-Tanguy model

To describe excitonic effects at the direct band gap of Ge, we use the expression for the complex dielectric function given by the Tanguy model for the Hulthén potential [7]

$$\epsilon(E) = \frac{A\sqrt{R}}{(E + i\gamma)^2} \times [\tilde{g}(\xi(E + i\gamma)) + \tilde{g}(\xi(-E - i\gamma)) - 2\tilde{g}(\xi(0))] \quad (35)$$

with

$$\xi(z) = \frac{2}{\left(\frac{E_0-z}{R}\right)^{1/2} + \left(\frac{E_0-z}{R} + \frac{4}{g}\right)^{1/2}}, \quad (36)$$

and

$$\tilde{g}(\xi) = -2\psi\left(\frac{g}{\xi}\right) - \frac{\xi}{g} - 2\psi(1-\xi) - \frac{1}{\xi}, \quad (37)$$

where $\psi(z)$ is the digamma function, A is the amplitude, R is the excitonic binding energy, γ is the broadening, and E_0 is the direct band gap energy. The Hulthén screening parameter g depends on the carrier concentration and is set to $g = 35$ for undoped Ge, according to Fig. 5 in Ref. 47. However, g is not independent of temperature due to the temperature-dependent carrier concentration (see Figs. 4.10 and 4.11 in the supplementary material). The four terms in Eq. (37) define the lineshape of the direct band gap, which is illustrated in Fig. 4.1. We define $\epsilon(E) = \epsilon_1(E) + i\epsilon_2(E) = \sum_{j=1}^4 f_j$ with

$$f_1 = -2\beta \left[\psi\left(\frac{g}{\xi(z_1)}\right) + \psi\left(\frac{g}{\xi(z_2)}\right) + \psi\left(\frac{g}{\xi(0)}\right) \right], \quad (38)$$

$$f_2 = -\frac{\beta}{g} [\xi(z_1) + \xi(z_2) + \xi(0)], \quad (39)$$

$$f_3 = -2\beta [\psi(1-\xi(z_1)) + \psi(1-\xi(z_2)) + \psi(1-\xi(0))], \quad (40)$$

and

$$f_4 = -\frac{\beta}{\xi(z_1)} - \frac{\beta}{\xi(z_2)} - \frac{\beta}{\xi(0)}, \quad (41)$$

where $\beta = A\sqrt{R}(E + i\gamma)^{-2}$, $z_1 = E + i\gamma$, and $z_2 = -E - i\gamma$. The first term, f_1 , describes the enhancement due to the exciton continuum (unbound excitons), f_3

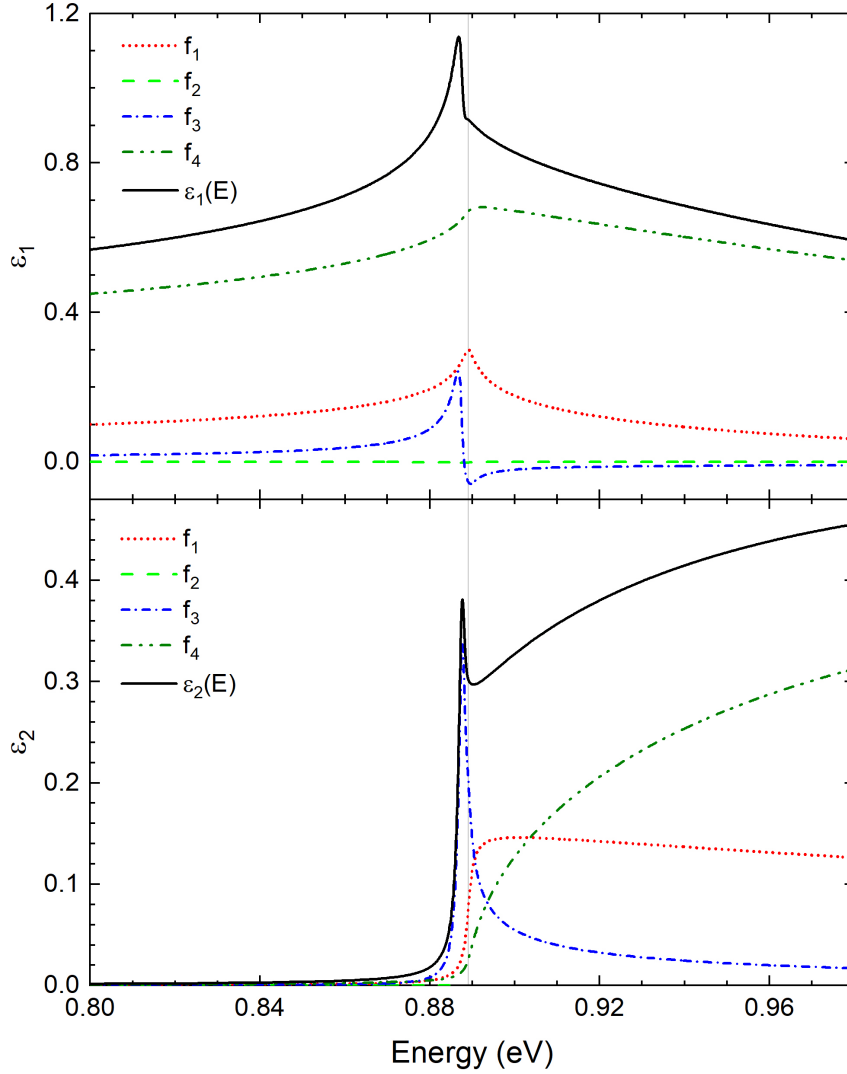


Figure 4.1: Real and imaginary parts of the terms in Eq. (35), defined in Eqs. (38)-(41), with $E_0 = 0.889$ eV (marked by the vertical line), $\gamma = 1$ meV, $R = 1.5$ meV, $A = 1.0$ eV $^{-3/2}$, and $g = 35$. The solid line represents the dielectric function as defined in Eq. (35), which is equivalent to the sum of the four terms f_1 - f_4 in Eqs. (38)-(41). For large g , $f_2=0$.

describes the peak of the bound exciton, and f_4 is equal to a three-dimensional critical point lineshape, that describes the absorption edge without excitonic effects. For large screening parameters, i.e. $g \gg 1$, f_2 vanishes.

The Hulthén-Tanguy model assumes spherical parabolic bands [7, 27], as well as one conduction and one valence band, but since two degenerate valence bands (hh and lh) are present at the Γ -point of Ge, one would have to solve a complicated three-body problem [47]. However, the error made by adding separate hh- and lh-excitons is small, as discussed in Refs. 47 and 5, and therefore we use separate terms for the hh and lh. To take into account contributions from the E_1 critical point to the real part of the dielectric function, we add a single term from the Sellmeier dispersion formula, i.e. $1 + A_1/(1 - B_1'^2 E^2)$, where we treat the parameters A_1 and $B_1' = B_1/(2\pi c\hbar)$ as adjustables. Values for A_1 and B_1 for Ge can be found in Ref. 49 ($A_1 \approx 14.76$, $B_1' \approx 0.35 \text{ eV}^{-1}$). Since the split-off band contribution $E_0 + \Delta_0$ is small and only affects the real part of the dielectric function, which can be compensated by adapting the Sellmeier parameters, we do not include an additional term for the split-off band. Following these considerations, the expression that we use for the fits is

$$\begin{aligned} \epsilon(E) = & 1 + \frac{A_1}{1 - B_1'^2 E^2} \\ & + \frac{A_{hh}\sqrt{R_{hh}}}{(E + i\gamma_{hh})^2} [\tilde{g}(\xi(E + i\gamma_{hh})) + \tilde{g}(\xi(-E - i\gamma_{hh})) - 2\tilde{g}(\xi(0))] \\ & + \frac{A_{lh}\sqrt{R_{lh}}}{(E + i\gamma_{lh})^2} [\tilde{g}(\xi(E + i\gamma_{lh})) + \tilde{g}(\xi(-E - i\gamma_{lh})) - 2\tilde{g}(\xi(0))], \end{aligned} \quad (42)$$

where γ_{hh} and γ_{lh} are the hh- and lh-broadening parameters, respectively. The excitonic amplitude is given by [21]

$$A_h = \frac{e^2 \sqrt{m_0}}{\sqrt{2\pi\epsilon_0 \hbar}} \mu_h^{3/2} \frac{E_P}{3}, \quad (43)$$

where $h = hh, lh$, e is the electron charge, m_0 is the free electron mass, ϵ_0 is the vacuum permittivity, μ_h is the reduced mass calculated from the effective mass of the hh or lh and the effective mass of the electron in the Γ -valley, and $E_P = 2P^2/m_0$ with P being the $k \cdot p$ momentum matrix element corresponding to interband transitions between the Γ'_{25} valence band and the Γ'_2 conduction band. From the reduced mass $\mu_h = m_h m_{e\Gamma} / (m_h + m_{e\Gamma})$ and the Rydberg energy of the hydrogen atom $R_y = 13.6$ eV, the excitonic binding energy is calculated

$$R_h = \frac{\mu_h}{m_0 \epsilon_{st}^2} R_y, \quad (44)$$

where ϵ_{st} is the static dielectric constant. The effective mass $m_{e\Gamma}$ of the electron in the Γ -valley is related to E_P and E_0 : [50–52]

$$\frac{m_0}{m_{e\Gamma}} = 1 + \frac{E_P}{3} \left[\frac{2}{E_0} + \frac{1}{E_0 + \Delta_0} \right], \quad (45)$$

where $\Delta_0 = 0.29$ eV [6, 53] is the temperature independent spin-orbit splitting at the Γ -point. The hh and lh effective masses are given by [54]

$$\frac{m_0}{m_{hh}} = \frac{1}{\hbar^2} \left[-A + \sqrt{B^2 + C^2/5} \right] \quad (46)$$

and

$$\frac{m_0}{m_{lh}} = \frac{1}{\hbar^2} \left[-A - \sqrt{B^2 + C^2/5} \right], \quad (47)$$

where A , B , and C are parameters introduced by Dresselhaus, Kip, and Kittel [55] (DKK), which are defined as [52, 55]

$$A = \frac{1}{3} [F + 2G + 2M] + 1, \quad (48)$$

$$B = \frac{1}{3} [F + 2G - M], \quad (49)$$

$$C^2 = \frac{1}{3} [(F - G + M)^2 - (F + 2G - M)^2]. \quad (50)$$

The DKK parameters A , B , and C^2 depend on temperature via [21]

$$F(T) = -E_P(T)/E_0(T), \quad (51)$$

$$M(T) = -E_Q(T)/E'_0(T), \quad (52)$$

$$G(T) = G(4.2 \text{ K}) \frac{a_0^2(4.2 \text{ K})}{a_0^2(T)}. \quad (53)$$

The temperature dependence of E'_0 is taken from Ref. 20:

$$E'_0(T) = (3.18 \text{ eV}) - (0.05 \text{ eV}) \left(1 + \frac{2}{e^{\frac{313 \text{ K}}{T}} - 1} \right). \quad (54)$$

In Eq. (52), $E_Q = 2Q^2/m_0$, and Q is the non-zero matrix element corresponding to interband transitions between the Γ'_{25} valence band and the Γ'_{15} conduction band [21, 52]. Thermal expansion causes a temperature dependence of the matrix elements $M = P, Q$ given by [5]

$$E_M(T) = E_M(4.2 \text{ K}) \times \frac{a_0^2(4.2 \text{ K})}{a_0^2(T)}, \quad (55)$$

via the temperature-dependent lattice constant

$$a_0(T) = (5.6516 \text{ \AA}) + \frac{\beta}{\exp(T_0/T) - 1}, \quad (56)$$

Table 4.2: Parameters at 4.2 K, determined as explained in the text. Effective and reduced masses are given in units of m_0 .

$m_{e\Gamma}$	m_{hh}	m_{lh}	μ_{hh}	μ_{lh}	A_{hh}	A_{lh}	R_{hh} (meV)	R_{lh} (meV)
0.036	0.33	0.042	0.032	0.019	0.74	0.35	1.8	1.1

where $\beta = 1.315 \times 10^{-2} \text{ \AA}$ and $T_0 = 355.14 \text{ K}$ are parameters describing thermal expansion of the Ge lattice [5]. The change of the matrix elements with temperature is small (less than 1% between 0 and 800 K). Therefore, the major contribution to the temperature dependence of the DKK parameters and consequently of the effective masses stems from the energy gaps.

Equation 53 specifies the contribution related to the matrix element R between Γ'_{25} and Γ'_{12} [21, 52]. Since the temperature dependence of this gap is not known, we use $A = -13.34$, $B = -8.48$, and $|C| = 13.14$ at 4.2 K from Ref. 5 in order to find exact low-temperature solutions. Using $E_0(4.2 \text{ K}) = 0.889 \text{ eV}$ [56], we obtain $E_P(4.2 \text{ K}) = 26.0 \text{ eV}$ (which is close to the value of 26.3 eV reported by Lawaetz [57]), $E_Q(4.2 \text{ K}) = 18.5 \text{ eV}$, and $G(4.2 \text{ K}) = -1.04$. Table 4.2 lists the resulting effective and reduced masses, amplitudes, and excitonic binding energies at liquid He temperature. The conduction band effective mass $m_{e\Gamma}$ agrees well with $m_{e\Gamma} = 0.037 m_0$ reported by Roth *et al.* [58] and $m_{e\Gamma} = 0.038 m_0$ by Lawaetz [57], and the calculated hh and lh masses are in reasonable agreement with the values found by Lawaetz [57] ($m_{hh} = 0.35 m_0$ and $m_{lh} = 0.043 m_0$).

4.4 Second derivatives through linear filtering

To obtain the second energy derivatives, we apply the linear filter method using Gaussian kernels by Le *et al.* [11], which is based on a direct space convolution

$$\bar{f}(E) = \int_{-\infty}^{\infty} dE' f(E') b_M(E - E') \quad (57)$$

with extended Gauss (EG) [11, 45, 46] filters

$$b_m(x) = \left(1 - \frac{a}{1!} \frac{d}{da} + \dots (-1)^m \frac{a^m}{m!} \frac{d^m}{da^m} \right) a^{-\frac{1}{2}} e^{-\frac{x^2}{4a}}, \quad (58)$$

where $a = \Delta E^2$ and $m = 1, \dots, M$. This technique allows for simultaneous noise reduction, interpolation, calculation of derivatives, and scale change [11]. The latter is not needed for our data which were measured with equidistant energy steps.

We choose $M = 4$ following the discussions in Refs. 11 and 44, and since we do not see a significant advantage in using M of higher-order. Substituting Eq. (A2) into Eq. (A1) and approximating the integral as a sum over the data points $f(E_j) = \epsilon_j$, in accordance with Eq. (21c) in Ref. 11 for wavelength-to-energy conversion, we can write the dielectric function for $M = 4$ and equidistant energy steps $\Delta E'$ as

$$\bar{\epsilon}_4(E) \approx \frac{\pi^{-\frac{1}{2}} \Delta E'}{12288 \Delta E^3} \sum_{j=-\infty}^{\infty} \left[\epsilon_j e^{-\frac{(E-E_j)^2}{4\Delta E^2}} \left(15120 - \frac{10080(E-E_j)^2}{\Delta E^2} + \frac{1512(E-E_j)^4}{\Delta E^4} - \frac{72(E-E_j)^6}{\Delta E^6} + \frac{(E-E_j)^8}{\Delta E^8} \right) \right] \quad (59)$$

from which we calculate the second derivative

$$\begin{aligned} \frac{d^2\bar{\epsilon}_4(E)}{dE^2} &\approx \frac{\pi^{-\frac{1}{2}}\Delta E'}{49152\Delta E} \sum_{j=-\infty}^{\infty} \left[\epsilon_j e^{-\frac{(E-E_j)^2}{4\Delta E^2}} \right. \\ &\times \left(-110880 + \frac{188496(E-E_j)^2}{\Delta E^2} - \frac{45936(E-E_j)^4}{\Delta E^4} \right. \\ &\left. \left. + \frac{3608(E-E_j)^6}{\Delta E^6} - \frac{106(E-E_j)^8}{\Delta E^8} + \frac{(E-E_j)^{10}}{\Delta E^{10}} \right) \right]. \end{aligned} \quad (60)$$

Equation (59) can be used to obtain a continuous function of the dielectric function with noise reduction depending on the filter width ΔE , which is chosen according to the white noise onset of the Fourier coefficients obtained from a discrete Fourier transform of the data [11,44] and is illustrated in Fig. 4.2. The Fourier coefficients

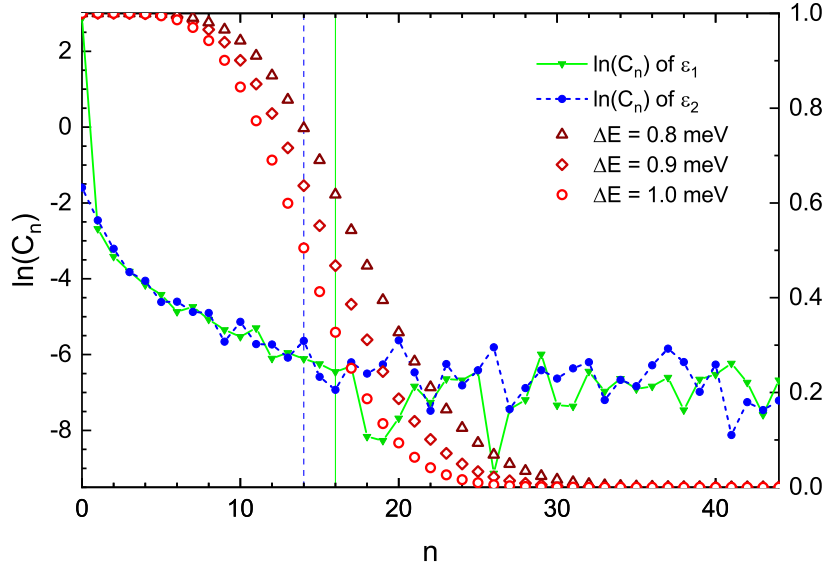


Figure 4.2: Natural logarithm of the Fourier coefficient amplitude C_n of the real (ϵ_1) and imaginary (ϵ_2) part of the dielectric function of Ge at 80 K, obtained as explained in the text. Symbols represent the Fourier transform of the EG filters for $M = 4$ and different ΔE . The vertical lines mark the onset of white noise for ϵ_1 (solid) and ϵ_2 (dashed), respectively. $\Delta E = 0.85$ meV for ϵ_1 and $\Delta E = 0.95$ meV for ϵ_2 are the best choices for this case.

C_n of the real (ϵ_1) and imaginary (ϵ_2) part of the dielectric function are obtained from a discrete Fourier transform along with removal of endpoint discontinuities, as described in Ref. 42. Comparing the Fourier transform $B_4(n)$ of the EG filter (symbols in Fig. 4.2) with $\ln(C_n)$, it becomes obvious why the right choice of ΔE is crucial to efficiently suppress noise while at the same time preserving information about the lineshape contained in the lower order Fourier coefficients [11, 44]. In other words, if ΔE takes on a value that is too small, noise is enhanced and distorts the lineshape, while a rather large ΔE broadens the lineshape. For most data sets, the filter widths of ϵ_1 and ϵ_2 are chosen to have the same value, but for some cases (such as the one shown in Fig. 4.2), ϵ_2 requires slightly more filtering. We reach the best compromise between noise reduction and broadening of the lineshape due to the filter for a drop of B_4 by approximately 40-50% at the onset of white noise (similar to Fig. 5 in Ref. 11 and Fig. 2 in Ref. 44). For the data shown in Fig. 4.2, this corresponds to a filter width of $\Delta E = 0.85$ meV for ϵ_1 and $\Delta E = 0.95$ meV for ϵ_2 , which is about twice the step size ($\Delta E' = 0.4$ meV) and about the same as the instrumental broadening for E_0 at 80 K.

Determining the filter widths from the Fourier coefficients provides a tangible method to set the amount of smoothing for each data set in the same way. For the calculation of the second derivatives of our data, smoothing works slightly better using the EG filter method compared to the commonly used Savitzky-Golay [37] technique. This is illustrated in Figs. 4.16 and 4.17 in the supplementary material.

In more recent publications, the authors of Ref. 11 point out that the EG filter can be outperformed by either using different filters [59] or by exploiting a maximum-entropy method [60] to extend the Fourier coefficients beyond the white-noise onset to reconstruct data and generate derivatives that are effectively noise-free. For the purpose of our investigations, we achieve satisfactory results utilizing the EG filters.

4.5 Fitting

The fits are performed using a standard Levenberg-Marquardt algorithm [61], modified for the possibility of a simultaneous fit of the real and imaginary parts of the dielectric function and their second energy derivatives by calculating a weighted χ^2 . Parts (a) and (b) of Fig. 4.3 show ϵ_1 and ϵ_2 (dotted lines), respectively, determined through independent fits at each wavelength (point-by-point fits) and corrected for the native oxide layer at various temperatures. Dotted lines in (c) and (d) represent the second derivatives calculated via Eq. (70) and solid lines in (a)-(d) show the fits with Eq. (42). The energy and broadening parameters are fitted to ϵ_1 and ϵ_2 and their second energy derivatives, $d^2\epsilon_1/dE^2$ and $d^2\epsilon_2/dE^2$, while the Sellmeier parameters are fitted to the real part only. Since the hh and lh excitonic peaks cannot be distinguished in our data, we set $\gamma = \gamma_{hh} = \gamma_{lh}$. The agreement between the model and the data right at the band gap (i.e. in the range of $E_0 \pm 40$ meV) at room temperature and below is remarkable, particularly

in view of the fact that amplitudes are not fitted, as in traditional ellipsometry work. At the lowest temperatures (10-110 K), however, while the model provides a good description of the exciton continuum, the excitonic peak, which depends on the broadening, the amount of screening, and the excitonic binding energy, is not described well by the model. The reason for this discrepancy is unclear, but might partly be related to the broadening and to limitations of our additive model for the excitonic contributions of light- and heavy-holes. Above room temperature,

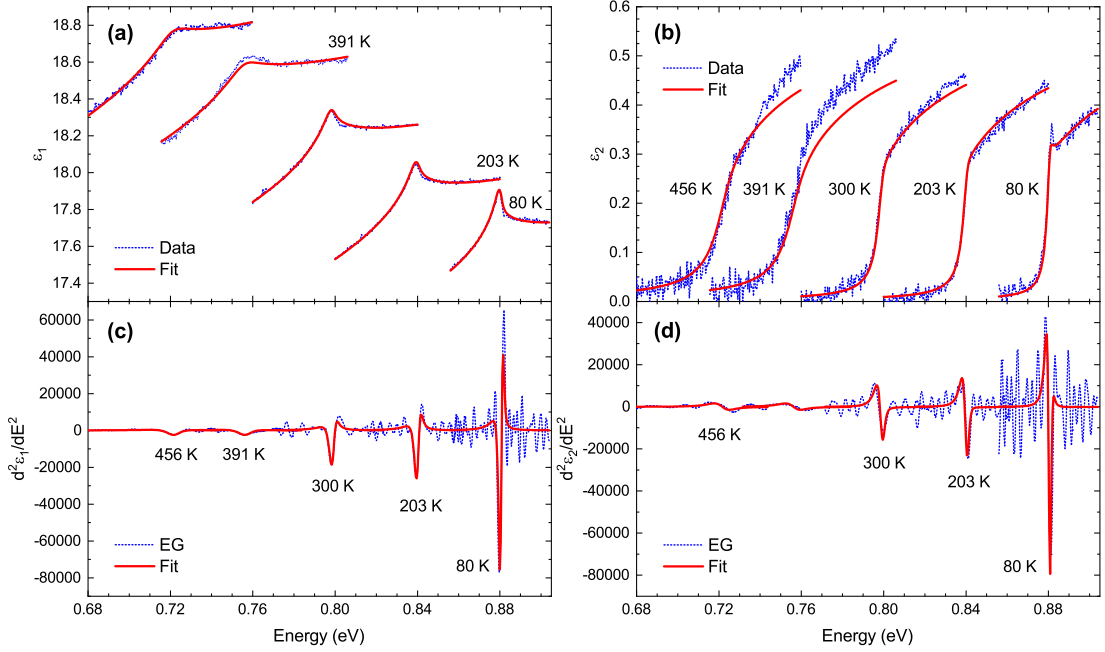


Figure 4.3: Real (a) and imaginary (b) parts of the dielectric function and the corresponding second derivatives with respect to energy, (c) and (d), respectively, calculated from Eq. (70) at various temperatures. Solid lines represent the best fits to the data.

we observe distortions at about 0.74, 0.77, and 0.8 eV due to xenon lamp spectral line peaks. These distortions seem to affect the second derivatives and the broad-

ening between 370 and 450 K. It may be possible to avoid this problem by taking measurements with a quartz tungsten halogen lamp, which does not have discrete spectral lines. Furthermore, the agreement between the model and the imaginary part ϵ_2 worsens with increasing temperature. This can be explained only to some extent by the uncertainty caused by the native oxide layer correction. Changing the oxide layer thickness by 1 Å results in a change in the ϵ_2 magnitude of about 6%, while the deviation between model and data at $T > 500$ K is on the order of 10-25%. This is illustrated in part (b) of Fig. 4.4, which shows the fit results of the 690 K measurement. Although it appears that the band gap energy is off by a few meV and shifting the fit to the left (dashed curve) improves the agreement of the model and ϵ_2 , it worsens the real part and the second derivatives. Hence, we conclude that the problem lies with the amplitude rather than the direct band gap energy.

We have extended the model to include non-parabolicity and the energy dependence of the momentum matrix element, but we find that the overall effect is negligible for the spectral range of our fits, and therefore use the simpler formulation for parabolic bands. The discrepancies due to non-parabolicity are small for $E - E_0 < 40$ meV and only become important for $E - E_0 > 100$ meV.

Due to the issue with the magnitude it was necessary for the high-temperature data sets to fit the energies and, in some cases also the broadenings, to the second derivatives only. At the highest temperature (710 K), the energy and broadening

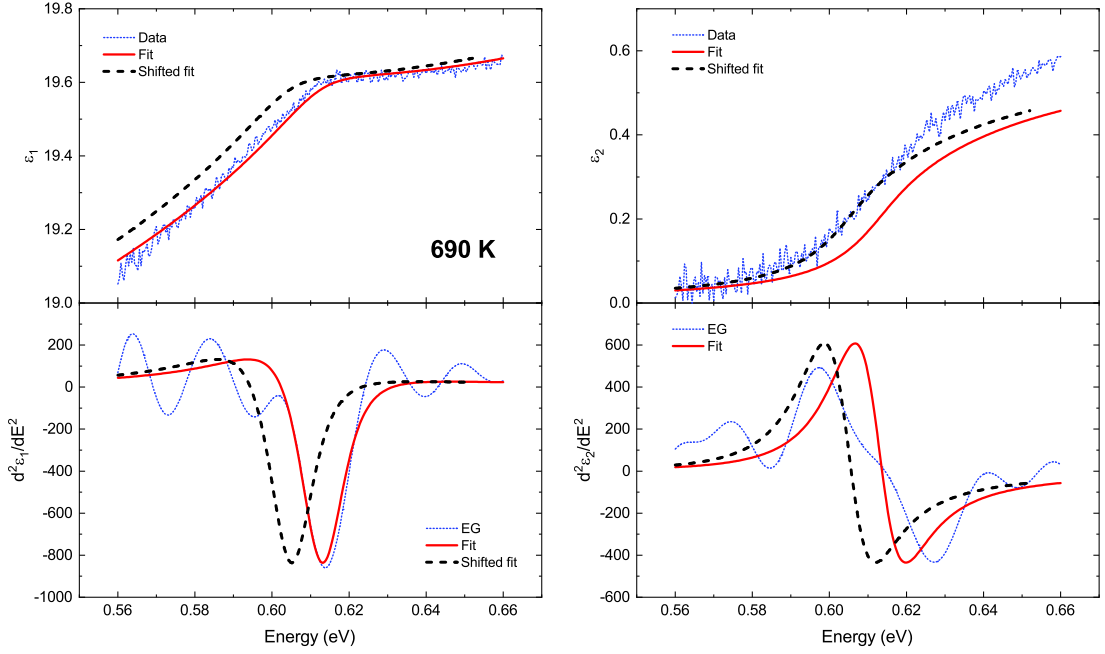


Figure 4.4: Like Fig. 4.3 for a temperatures of 690 K, where the solid line represents the best fit to the data and the dashed line shows the fit shifted by 8 meV towards lower energies.

were fitted to the second derivative of ϵ_2 only, since $d^2\epsilon_1/dE^2$ is too distorted as a results of noise. Figure 4.9 shows the fit results at 598, 639, 676, and 710 K.

4.6 Temperature dependence

Figure 4.5 shows the temperature dependence of the direct band gap energy obtained from the Tanguy fits compared to results from Refs. 6 and 56. The temperature dependence of the broadening parameters obtained from the Hulthén-Tanguy fits is shown in Fig. 4.6 along with experimental results by McLean and Paige [62,63] and Aspnes [26], and the broadening calculated according to Eq. (38) in Ref. 47 for $\epsilon = 0$. For the latter, only contributions corresponding to scattering

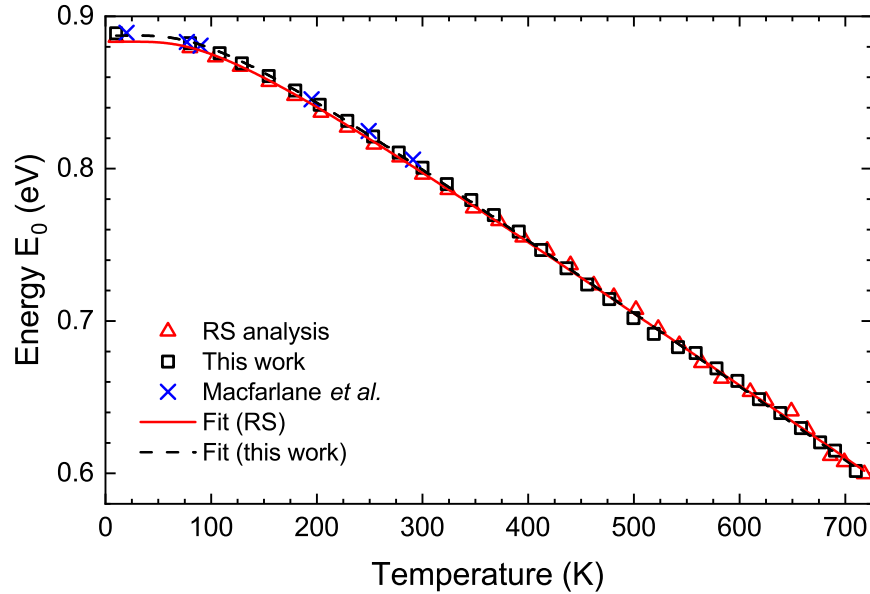


Figure 4.5: Temperature dependence of the direct band gap energy obtained from the fits with Eq. (42) (\square), compared to the results by a reciprocal space analysis [6] (\triangle) and the results from Macfarlane *et al.* [56] (\times). Lines represent fits with Eq. (61).

of electrons with LA and LO phonons are taken into account (for further explanations see Sec. 4.8.2 in the supplementary material). Temperature-dependent phonon energies from Ref. 64 are considered in the calculation, as well as the temperature dependence of the transverse mass using Eqs. (B4) and (B5) in Ref. 5. The deformation potentials (taken from Ref. 47) and the longitudinal mass are assumed to be independent of temperature. For better comparison with the theory, the instrumental resolution is added to the calculated broadening. We note that the agreement between the experimental and predicted broadenings is reasonable up to room temperature. Theory and experiment begin to diverge at the temperatures when the lineshape fits begin to worsen. Taking into account

the temperature dependence of the screening parameter g reduces the broadening at the highest temperatures by about 10% (see Sec. 4.8.3 in the supplementary material), as shown in Fig. 4.12.

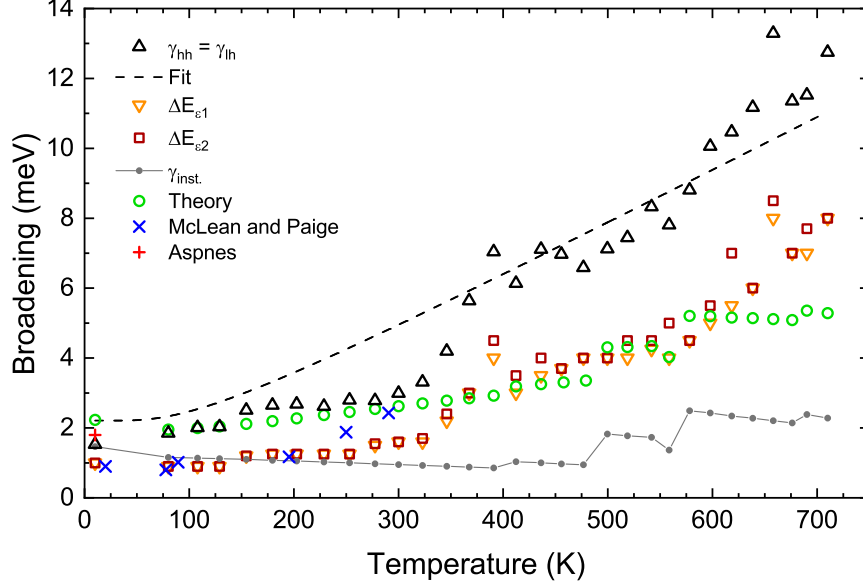


Figure 4.6: Temperature dependence of the broadening obtained from the fits (Δ), best fit to the data with Eq. (62) (dashed), filter widths used for the real part (∇) and imaginary part (\square), the instrumental resolution ($\gamma_{\text{inst.}}$), calculated width as explained in the text (\circ), and values from McLean and Paige [62,63] (\times) and Aspnes [26] ($+$). The hh and lh broadening parameters are forced to have the same value.

To fit the temperature dependence due to electron-phonon interactions, we use the Bose-Einstein model for the energies [23]

$$E(T) = E_a - E_b \left[1 + 2 / \left(e^{E_{\text{ph}} / (k_B T)} - 1 \right) \right], \quad (61)$$

where E_a is the unrenormalized transition energy, E_b is the electron-phonon coupling strength, k_B is the Boltzmann constant, and $E_{\text{ph}} = k_B \Theta_{\text{ph}}$ is the effective

phonon energy. A similar expression describes the broadening as function of temperature [23]

$$\gamma(T) = \gamma_1 + \gamma_0 \left[1 + 2 / \left(e^{E_{\text{ph}}/(k_B T)} - 1 \right) \right]. \quad (62)$$

Equation (62) is an attempt to capture the complex physics of the electron-phonon self energies in a simple expression that uses an effective phonon frequency. It is helpful as a compact parametrization of the experimental data. The fits with the above equations are shown by the various lines in Figs. 4.5 and 4.6, and the fit parameters in Eqs. (61) and (62) are listed in Tabs. 4.3 and 4.4.

Table 4.3: Parameters E_a , E_b , and the effective phonon energy E_{ph} obtained from fitting Eq. (61) to the temperature dependent energy E_0 of the direct band gap for different analysis methods and models.

	E_a (eV)	E_b (eV)	E_{ph} (meV)
This work	0.958 ± 0.002	0.071 ± 0.003	25 ± 1
RS (Ref. 6)	0.953 ± 0.003	0.070 ± 0.004	25 ± 1
SD, 3D (Ref. 6)	0.947 ± 0.004	0.061 ± 0.005	22 ± 2

We find $E_0 = 888.8 \pm 0.5$ meV at 10 K and $E_0 = 882.4 \pm 0.5$ meV at 80 K, which compare well to the energies reported by Nishino *et al.* [66] (889.0 meV at 24 K and 881.4 meV at 83 K) and Macfarlane *et al.* [56] (889.2 meV at 20 K and 883.2 eV at 77 K). Aspnes [26] found $E_0 = 887.2$ meV and the excitonic energy $E_{\text{ex}} = 885.8 \pm 0.5$ meV, as well as a broadening of 1.8 ± 0.3 meV at 10 K.

The decrease in the effective masses between 10 and 710 K is 29% for $m_{e\Gamma}$

Table 4.4: Parameters obtained by fitting Eq. (62) to the temperature dependent broadening, where $\gamma_0 = 0$, and the effective phonon energy was fixed to the value obtained from fitting the energy (see Tab. 4.3). Calculated values from Ref. 65 are listed for comparison.

	γ_1 (meV)	E_{ph} (meV)
This work	2.21 ± 0.06	25(f)
Theory (Ref. 65)	1.459 ± 0.001	27.6 ± 0.2

and m_{lh} , and 9% for m_{hh} according to Eqs. (45), (46), and (47). The major contribution to the temperature dependence of the effective masses stems from the energies E_0 (Fig. 4.5) and E'_0 via the DKK parameters defined in Eqs. (48)-(50), since the changes due to thermal expansion of the matrix elements are small. This temperature dependence of the effective masses also leads to a temperature-dependent excitonic binding energy. According to Ref. 67, the excitonic binding energy is proportional to the direct band gap energy, $R_h \propto E_0$, illustrated by the dotted line in Fig. 4.7. Our results do not satisfy this relation. Instead, we find

$$R_{hh}(E_0) = 2.158(5) \cdot E_0^{1.549(8)}$$

and

$$R_{lh}(E_0) = 1.302(3) \cdot E_0^{1.598(8)}.$$

Only two parameters affect the binding excitonic energy: the reduced mass and the static dielectric constant ϵ_{st} . We obtain ϵ_{st} , which is equal to the high-frequency dielectric constant ϵ_{∞} in the case of Ge, from our data by extrapolating

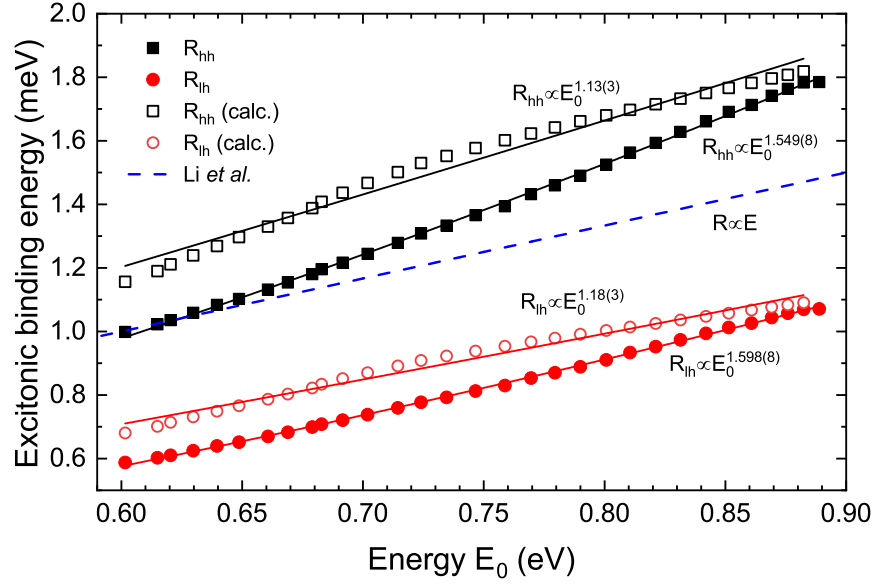


Figure 4.7: Excitonic binding energies of the heavy-hole (R_{hh}) and light-hole (R_{lh}) excitons calculated from Eq. (44) versus energy E_0 of the direct band gap (which varies with temperature, as shown in Fig. 4.5). Closed symbols depict R_{hh} and R_{lh} calculated using ϵ_{st} from extrapolating ϵ_1 to lower energies (symbols in Fig. 4.8) and open symbols show R_{hh} and R_{lh} calculated using Eq. (63) (line in Fig. 4.8). Solid lines represent fits with $R(E_0) = b \cdot E_0^x$ and the dashed line represents the extension to lower energies of the curve shown in Fig. 5 of Ref. 67 with $R_h \propto E_0^{1.0(1)}$.

the fit of the dielectric function with a parametric oscillator model [19] to very low energies. Figure 4.8 shows how ϵ_∞ increases with temperature, mostly due to the decrease of the Penn gap E_{Penn} via [21]

$$\epsilon_\infty(T) = 1 + \left(\frac{E_u}{E_{\text{Penn}}(T)} \right)^2. \quad (63)$$

We use $E_u = \hbar\omega_u = 15.6$ eV for Ge, which is calculated from the plasma frequency

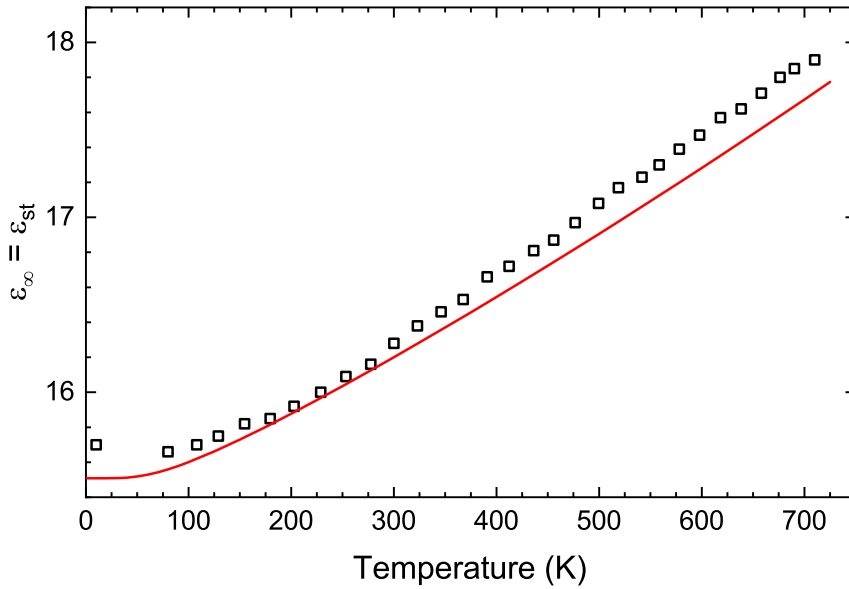


Figure 4.8: Temperature dependence of the high-frequency dielectric constant ϵ_∞ of Ge obtained from the experimental data (symbols) compared with ϵ_∞ calculated from Eq. (63) (line) using the literature value [69] $\epsilon_\infty(T = 300 \text{ K}) = 16.2$.

ω_u , and assume that E_{Penn} and E_2 have the same temperature dependence [68].

Taking the latter from Ref. 20 and $\epsilon_\infty = 16.2$ at room temperature from the literature [69], we can write the temperature dependence of the Penn gap as

$$E_{\text{Penn}}(T) = 4.146 \text{ eV} - 0.05 \text{ eV} \left(\frac{2}{e^{\frac{217\text{K}}{T}} - 1} + 1 \right). \quad (64)$$

We find a reasonable agreement between the high-frequency dielectric constant calculated from Eq. (63) (line in Fig. 4.8) and the values we obtain from the extrapolation of our data (symbols in Fig. 4.8) up to room temperature. The deviation at higher temperatures might explain the deviation of R_h from $R_h \propto E_0$. Using Eq. (63) to calculate R_{hh} and R_{lh} results in

$$R_{hh}(E_0) = 2.14(2) \cdot E_0^{1.13(3)}$$

and

$$R_{lh}(E_0) = 1.29(1) \cdot E_0^{1.18(3)}.$$

The effective masses used to compute R_{hh} and R_{lh} depend on the fit parameter E_0 as outlined in Sec. 4.3

4.7 Conclusion

Several assumptions and simplifications were made to the theory. Firstly, we simply added two Hulthén-Tanguy terms, one for the hh and one for the lh, instead of solving a complicated three-body problem. Secondly, the contribution of the split-off band was ignored since it only affects the real part of the dielectric function and the small effect can be compensated by adjusting the Sellmeier parameters. Thirdly, we did not consider warping and non-parabolicity. The latter results in a deviation between the model and the data starting at about 100 meV above the band gap. Furthermore, we ignore the indirect band gap which affects E_0 due to

the resonant character of the direct and indirect band gaps [5]. An experimental and theoretical study thereof is given in Ref. 5. This effect might be important for Ge because the indirect band gap lies only about 0.15 eV below the direct gap [4, 53]. Finally, we only fit the band gap energy and broadening, but no adjustable parameter that would affect the magnitude of the imaginary part. In principle, this theory can also be applied to other semiconductors with similar band structures such as GaAs, InSb, or germanium-tin alloys.

In summary, we fitted the Hulthén-Tanguy model to the dielectric function and its second derivatives and find the model to be in good agreement with our data up to room temperature. Discrepancies at higher temperatures might be partly due to the above-mentioned simplifications of the theory and partly due to the challenging experimental conditions at high temperatures. Improvements to the model and investigations of electron-phonon scattering processes will be addressed in future work.

Supplementary material

In the supplementary material, we discuss the broadening of the direct band gap and the limitations due to instrumental resolution, noise, and the digital linear filter. Furthermore, a brief discussion of the second derivatives obtained from the EG filter method and Savitzky-Golay coefficients, and fit results at some selected high temperatures are provided.

Acknowledgments

This work was supported by the Air Force Office of Scientific Research under award number FA9550-20-1-0135 and the National Science Foundation (NSF, No. DMR-1505172 and DMR-2119583).

4.8 Supplementary material

4.8.1 Fit results at higher temperatures

As an addition to the discussion in the main part of the manuscript regarding the discrepancies above 500 K, we show the fit results at some selected temperatures (598, 639, 676, and 710 K) in Fig. 4.9. Despite using an iris at the exit window of the cryostat to suppress black body radiation at high temperatures (as demonstrated in Fig. S4 in Ref. 6), the noise below about 0.6 eV is significant. At 710 K, it is not possible to obtain reasonable parameters from fitting the second derivative of the real part of the dielectric function ($d^2\epsilon_1/dE^2$) and hence the energy and broadening was obtained from fitting $d^2\epsilon_2/dE^2$ only. At all other temperatures, both $d^2\epsilon_1/dE^2$ and $d^2\epsilon_2/dE^2$ could be fitted with the second derivative of the Hulthén-Tanguy model.

4.8.2 Broadening of the direct band gap

4.8.2.1 Theory

Intervalley scattering of electrons by longitudinal acoustic (LA) phonons between the high symmetry Γ - and L -points is allowed, while longitudinal optical (LO) and transverse acoustic (TA) phonon scattering is forbidden [47]. However, to calculate the lifetime of the states at Γ that form the direct gap, transitions to points near but not necessarily coincident with L must be included. For this $\Gamma \rightarrow$ “around

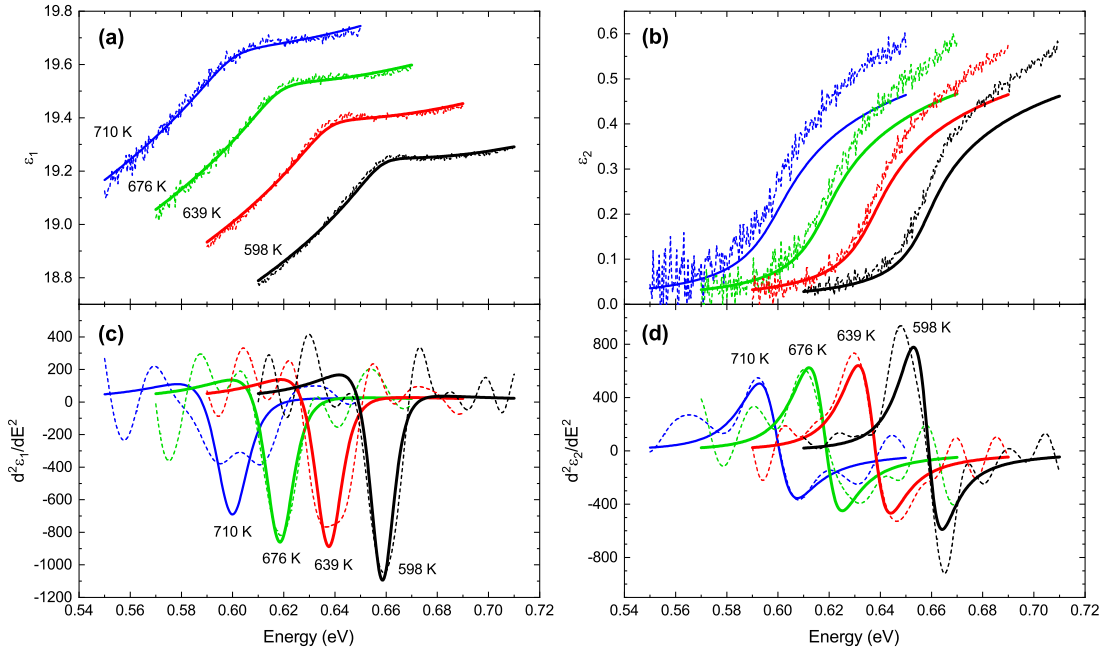


Figure 4.9: Like Fig. 4.3 for temperatures of 598, 639, 676, and 710 K.

L'' processes, transitions induced by TA and LO phonons become allowed due to the lower symmetry. Of these, *ab initio* calculations [70, 71] show that the TA contribution is negligible. A simple expression that captures this phenomenology is Eq. (38) in Ref. 47, which for $\epsilon = 0$ (the parameter ϵ represents the energy above the conduction band edge at Γ) corresponds to the broadening of the direct gap if the broadening of the hole states is neglected. The expression contains a term corresponding to LA phonons and a term corresponding to LO phonons. The LA contribution the scattering rate is equivalent to Conwell's expression [72]

$$\tau_{\Gamma L}^{-1} = \frac{N_V D_{\Gamma L}^2 m_{\text{eff}}^{3/2}}{\sqrt{2\pi\hbar^2\rho E_{\text{ph}}}} \times \left[N_{\text{ph}} \sqrt{\Delta E + E_{\text{ph}}} + (N_{\text{ph}} + 1) \sqrt{\Delta E - E_{\text{ph}}} \right], \quad (65)$$

where N_{ph} is the Bose-Einstein phonon occupation factor defined as

$$N_{\text{ph}} = \frac{1}{e^{E_{\text{ph}}/(k_B T)} - 1}. \quad (66)$$

$D_{\Gamma L}$ in Eq. (65) is the intervalley deformation potential for Γ to L scattering, $N_V = 4$ (four equivalent valleys at the L -point), ρ is the mass density, ΔE is the difference between the Γ -valley and L -valley minima, $E_{\text{ph}} = E_{\text{ph,LA}}$ is the LA-phonon energy at the L -point, and m_{eff} is the effective electron mass for the final state in a single valley calculated from the transverse and longitudinal effective masses at the L -point, $m_{\text{eff}} = (m_{\parallel} m_{\perp}^2)^{1/3}$. The LO scattering contribution is given by the second term in Eq. (38) in Ref. 47. Note also that a term representing scattering to the higher Δ -minimum vanishes due to energy conservation.

To assess the validity of the neglect of a hole contribution in the theoretical estimate of the broadening using Eq. (38) in Ref. 47, we explicitly estimate this contribution. Intravalley scattering of holes with optical phonons at the Γ -point is estimated by setting $\epsilon = 0$ in Eq. (4.42) in Ref. 73, which leads to

$$\tau_{\text{op},h}^{-1} = \frac{m_h^{3/2} D_o^2}{\sqrt{2\pi\rho\hbar^2} \sqrt{E_{\text{ph,op}}}} N_{\text{ph,op}}, \quad (67)$$

where $E_{\text{ph,op}}$ is the optical phonon energy at the Γ -point, $D_o = d_o/a$ is the optical deformation potential in units of eV/Å, a is the lattice constant, $N_{\text{ph,op}}$ is the phonon occupation factor of optical phonons, and m_h is the hh or lh effective mass.

To estimate the broadening related to intravalley deformation potential scattering of electrons with acoustic phonons, we use the expression for LA phonon intravalley scattering at the Γ -point in Ref. 73, which reads

$$\tau_{\text{ac}}^{-1}(\epsilon) = \frac{\sqrt{2}E_1^2 m_{e\Gamma}^{3/2} k_B T}{\pi \rho \hbar^4 v_s^2} \sqrt{\epsilon}, \quad (68)$$

where E_1 is the acoustic deformation potential in units of eV and $v_s = v_{\text{lo}}$ is the longitudinal sound velocity. Exactly at the Γ -point, Eq. (68) is zero. We set $\epsilon = 10$ meV to take into account a small region around the zone center to estimate if this type of scattering possibly becomes important away from Γ .

Table 4.5 lists the parameters defined above and which are used to calculate the scattering times and lifetime broadenings listed in Tabs. 4.6 and 4.7, respectively.

Table 4.5: Parameters in Eqs. (65)-(68) for Ge.

ρ	v_{lo}	E_1	d_{o}	$D_{\Gamma L}$	a	$E_{\text{ph,op}}$	$E_{\text{ph,LA}}$
(g/cm ³)	(10 ⁵ cm/s)	(eV)	(eV)	(eV/Å)	(Å)	(meV)	(meV)
5.32	5.4 ^a	11.4 ^b	37 ^c	2.8 ^d	5.66	37 ^e	28 ^e

^a Ref. 74

^b Ref. 75

^c Ref. 76

^d Ref. 77

^e Ref. 78

According to these calculations, it appears that the intravalley deformation

Table 4.6: Estimated relaxation times in fs from Eqs. (65)-(68) for the direct band gap of Ge at 10, 80, 300, and 710 K.

Temperature	τ_{ac}	$\tau_{op,hh}$	$\tau_{op,lh}$	$\tau_{\Gamma L}$
10 K	4.3×10^5	3.4×10^{21}	1.0×10^{23}	1050
80 K	5.4×10^4	1.7×10^5	4.9×10^6	550
300 K	1.4×10^4	2600	8.2×10^4	110
710 K	6000	740	3.1×10^4	53

Table 4.7: Estimated lifetime broadenings in meV at 10, 80, 300, and 710 K obtained from the relaxation times in Tab. 4.6.

Temperature	γ_{ac}	$\gamma_{op,hh}$	$\gamma_{op,lh}$	$\gamma_{\Gamma L}$
10 K	7.7×10^{-4}	9.5×10^{-20}	3.3×10^{-21}	0.31
80 K	6.1×10^{-3}	2.0×10^{-3}	6.8×10^{-5}	0.59
300 K	0.023	0.13	4.0×10^{-3}	3.0
710 K	0.055	0.44	0.011	6.2

potential scattering does not constitute an important contribution to the broadening, consistent with our initial assumptions. Notice that in our calculations we allowed small deviations from the exact maximum of the valence band. If we allow for a similar small energy shift from the minimum of the conduction band, TA-induced transitions from such “near- Γ ” states to the L -point also become allowed and have been shown to play a role in indirect absorption [47]. However, the contribution of such terms in our broadening expressions is also very small.

Although, as indicated above, *ab initio* calculations imply that TA phonons are unimportant at room temperature, we cannot state with certainty that they do not play a role at higher temperatures due to possible temperature-dependent deformation potentials (as for example in the case of GaAs, see Ref. 79) An increase in the deformation potential with temperature might improve the discrepancies between the experimental and predicted widths shown in Fig. 4.6 above 300 K. However, resolving the question of the importance of transverse phonon scattering requires more calculations of the intervalley scattering present in Ge, which is beyond the scope of this work. In the case of $D_{\Gamma L}$ in Eq. (65), we estimate $D_{\Gamma L} = 3 \text{ eV/\AA}$ for $T = 10 \text{ K}$, $D_{\Gamma L} = 4 \text{ eV/\AA}$ for $T = 80 \text{ K}$, and $D_{\Gamma L} = 6.5 \text{ eV/\AA}$ at room temperature and above to take into account a temperature-dependent deformation potential similar to the one in GaAs [79]. When adding the instrumental resolution of about 2 meV to the broadening at the highest temperatures, $\gamma_{\Gamma L} \approx 8 \text{ meV}$ which is still about 40% smaller than the width obtained from the

Hulthén-Tanguy fit.

4.8.3 Screening parameter

As mentioned in Sec. 4.6, the screening parameter g depends on temperature through the temperature-dependent carrier density N , which is calculated based on the model as in Eqs. (9)-(12) in Ref. 47. Figure 4.10 shows how the carrier density of intrinsic Ge increases from $N \approx 2 \times 10^{13} \text{ cm}^{-3}$ at 300 K to $N \approx 6 \times 10^{13} \text{ cm}^{-3}$ at 700 K. The screening parameters calculated from Eqs. (13) and

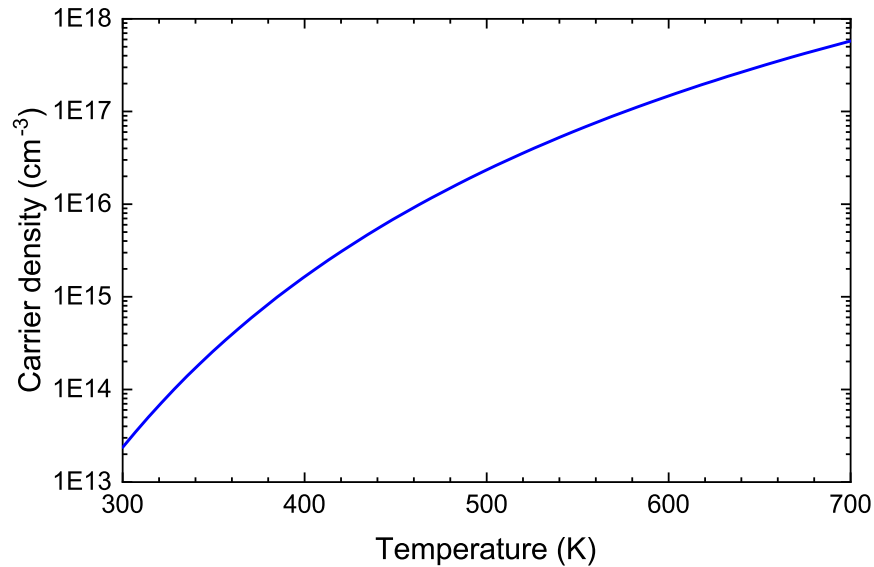


Figure 4.10: Carrier density of intrinsic Ge as a function of temperature.

(44) in Ref. 47 is plotted in Fig. 4.11. The temperature dependence of g has no significant impact on the results of the E_0 energies, but it starts affecting the broadening at $T > 500$ K, which is illustrated in Fig. 4.12. Using $g = 0.28$ at 700 K instead of $g = 35$ results in a decrease in broadening of about 10% at the

highest temperatures. The effect of using the temperature-dependent g on the

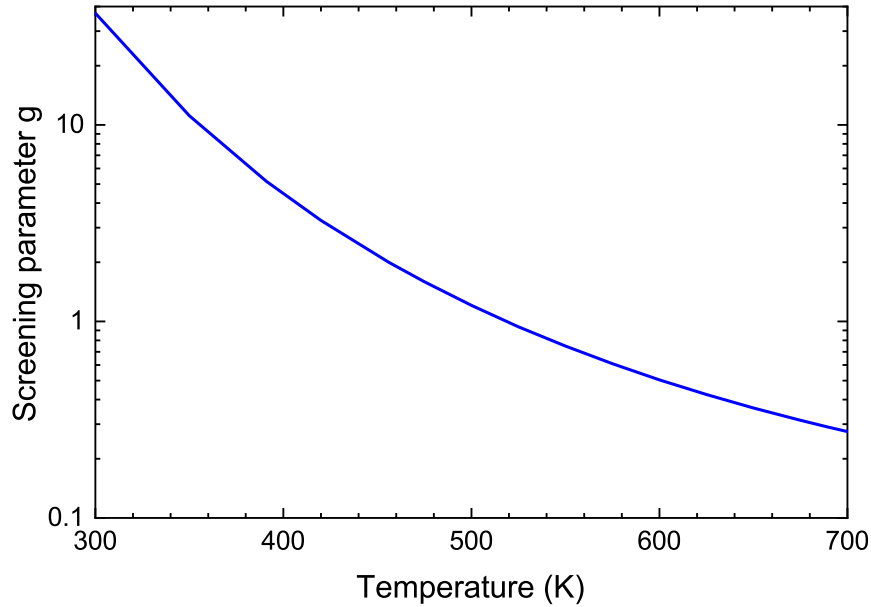


Figure 4.11: Screening parameter g of intrinsic Ge as a function of temperature, calculated from the carrier density shown in Fig. 4.10.

agreement between fit and data is small, as shown in Fig. 4.13 for the dielectric function and its second derivative at 710 K.

4.8.4 Experiment

Determining accurate information regarding the lifetime broadening of the direct band gap is challenging because of the limitation due to instrumental resolution and noise. The latter increases with temperature as a result of black body radiation and the simultaneous shift of the band gap to lower energies. Attempts to overcome the instrumental resolution by decreasing the width of the filter to the smallest possible value (0.6 meV, which is slightly larger than the step size),

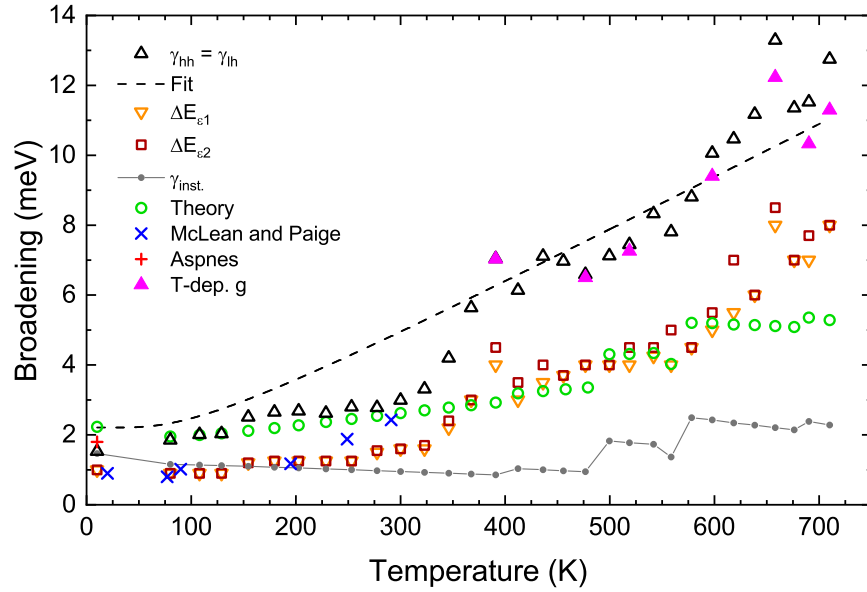


Figure 4.12: Like Fig. 4.6 including the broadening obtained from fits using the temperature-dependent screening parameter depicted in Fig. 4.11 (\blacktriangle).

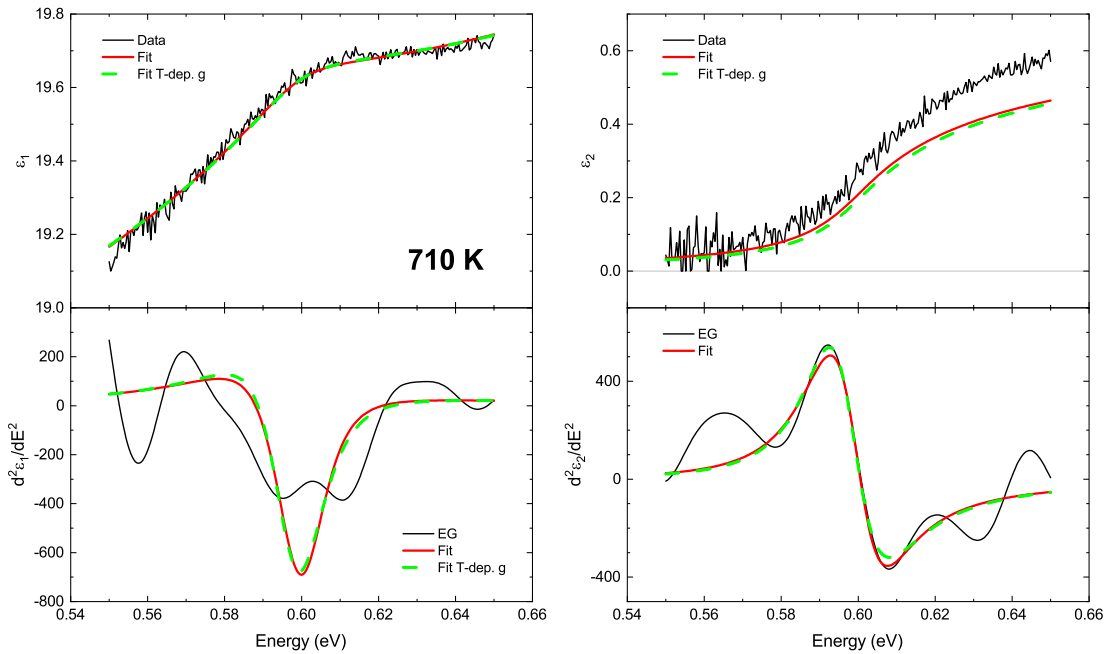


Figure 4.13: Fit results at 710 K (solid) as shown in Fig. 4.9, i.e. $g = 35$, compared to the fit using $g = 0.26$ (dashed).

result in a broadening of 1.3 meV, which is still twice as large as $\gamma_{th} = 0.77$ meV calculated from theory without adding the instrumental resolution. Below a filter width of 0.6 meV, noise becomes dominant and the derivatives cannot be used for analysis. Further reducing the instrumental resolution by using slit widths $< 400 \mu\text{m}$ does not show any advantages since it worsens the signal-to-noise ratio, which is also reflected in the second derivatives. Figure 4.14 depicts the model calculated from Eq. (42) for a temperature of 10 K and the parameters listed in Tab. 4.2 for $\gamma_{hh} = \gamma_{lh} = 0.77$ meV and $\gamma_{hh} = \gamma_{lh} = 1.53$ meV. On the one hand, using the predicted width of 0.77 meV increases the agreement between model and data for the excitonic peak, on the other hand, the theory does not describe the tail of the imaginary part ϵ_2 below the gap. For the data between 80 and 710 K, the tail in ϵ_2 is described well by the model.

Apart from restrictions due to resolution and noise, the nature of the Lorentzian broadening is questionable. It is pointed out in Ref. 5 that at room temperature a Gaussian broadening yields a much better agreement with experiment than a Lorentzian one, which is illustrated in Fig. 7 in Ref. 5. The tail of the Lorentzian broadening expands to the region of the indirect band gap, where it results in an absorption coefficient which is larger than the one of the indirect absorption itself. Furthermore, at higher temperatures, the exciton lineshape will be Gaussian rather than Lorentzian [80] and the temperature dependence of the broadening is proportional to T^2 [62]. Nevertheless, we fit the broadening parameters obtained

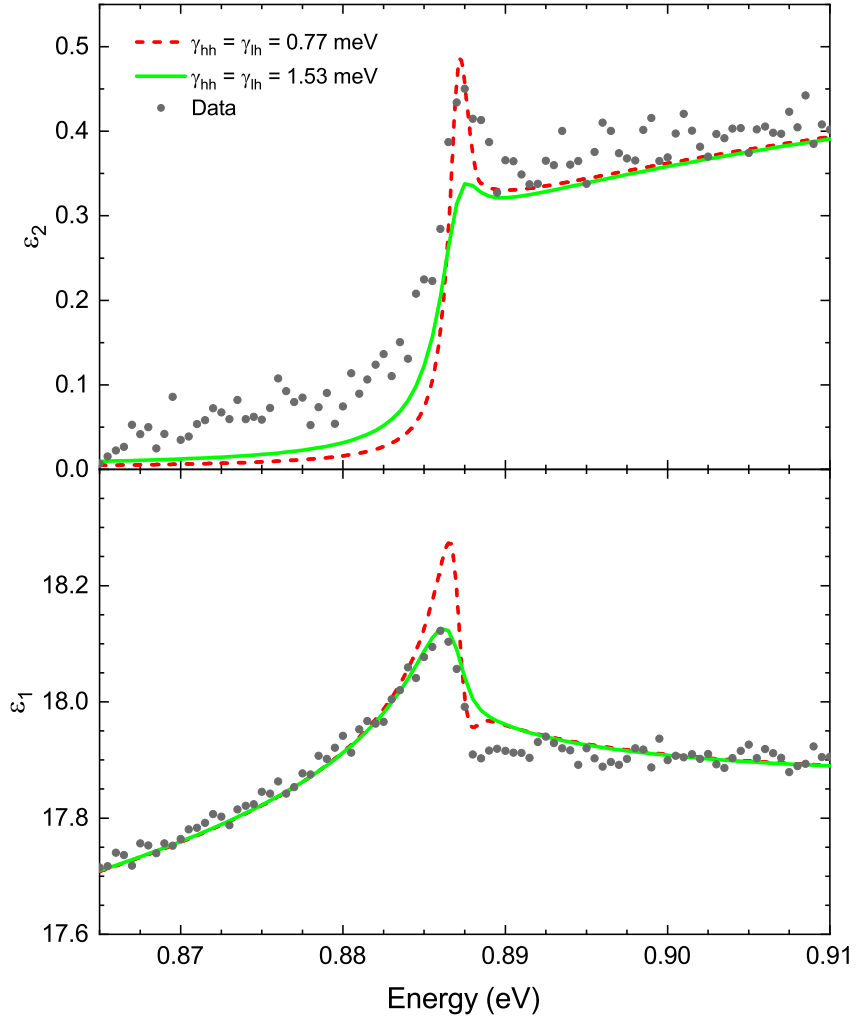


Figure 4.14: Imaginary (top) and real (bottom) part of the dielectric function for a broadening of $\gamma_{hh} = \gamma_{lh} = 0.77$ meV (dashed) and $\gamma_{hh} = \gamma_{lh} = 1.53$ meV (solid). Experimental data (symbols) at 10 K from Ref. 6.

from the fits to the Bose-Einstein model (Eq. (62)) in order to find an estimate of the effective phonon energy related to electron-phonon interaction. Due to the

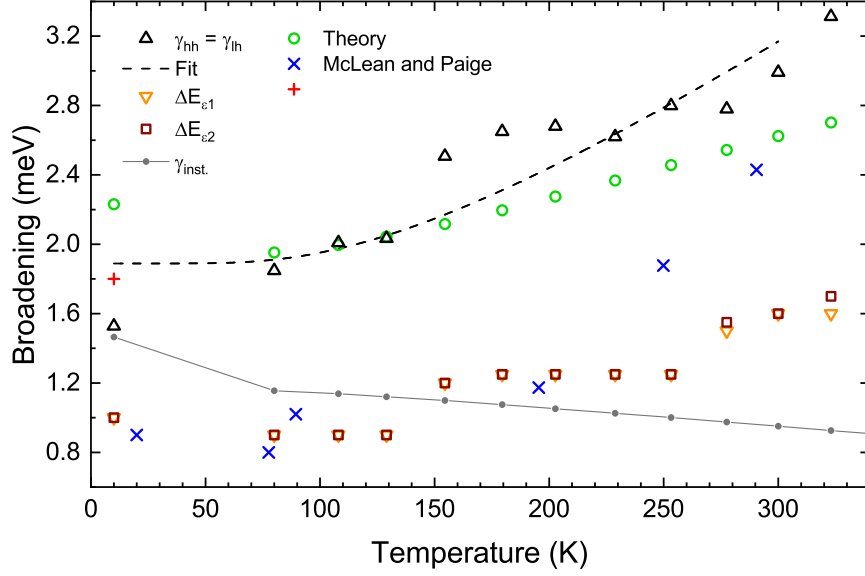


Figure 4.15: Like Fig. 4.6 showing the low temperature range. The dashed line represents the fit with Eq. (62) to the broadening between 10 and 300 K. Fit parameters are given in Tab. 4.8.

uncertainties at higher temperatures, we consider the low-temperature data only, see Fig. 4.15. The lines in Fig. 4.15 represent the best fit to the data using Eq. (62), where γ_0 was set to zero (fitting γ_0 leads to negative values for the zero-temperature broadening, which is unphysical). The fit parameters are listed in Tab. 4.8. Although the broadenings are probably enhanced due to the limitations discussed above, the phonon energies found from the fits are within a reasonable range (the energy of LA phonons at the L -point is 28 meV and the energy of optical phonons at the Γ -point is about 37 meV) [78].

Table 4.8: Parameters describing the temperature dependence of the broadening obtained by fitting Eq. (62) to the broadening between 10 and 300 K, where $\gamma_0 = 0$ was fixed, compared to values from the literature.

	γ_1 (meV)	E_{ph} (meV)
10-300 K (this work)	1.9 ± 0.1	36 ± 4
20-291 K (Ref. 62)	0.8	26

4.8.5 Second derivatives

Figures 4.16 and 4.17 show the second derivatives of the real and imaginary parts of the dielectric function, respectively, at a temperature of 10 K taken from Ref. 6. The derivatives calculated from Eq. (70) for a filter width of 1 meV (solid line) are compared to the derivatives obtained from the Savitzky-Golay (SG) algorithm [37] using a polynomial of third degree over $N = 10$ (squares) and $N = 11$ data points (circles). The amount of smoothing is comparable, however, the EG derivatives have the advantage of being a continuous function and hence having as many points available as needed for the analysis.

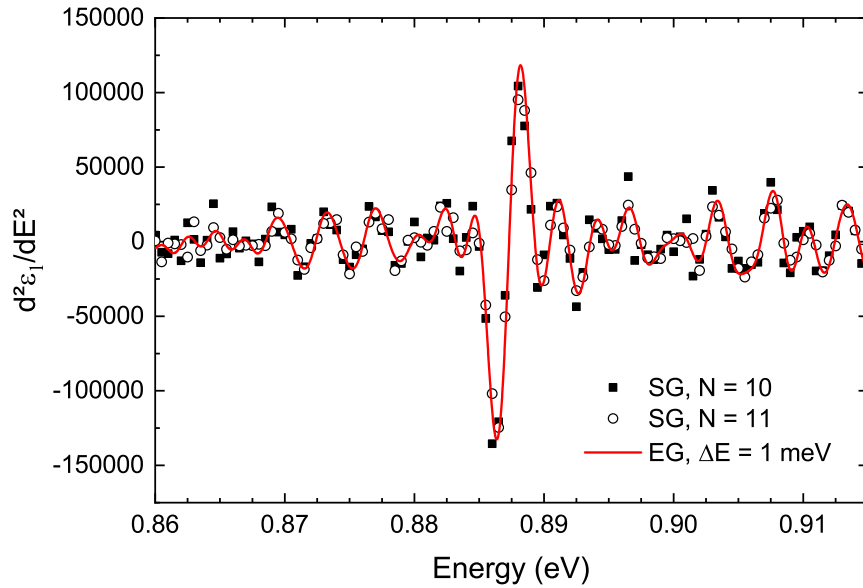


Figure 4.16: Second derivatives of the real part of the dielectric function of Ge at 10 K (data from Ref. 6) obtained from the Savitzky-Golay (SG) method using a polynomial of third degree over $N = 10$ and $N = 11$ data points compared with the second derivatives from the EG filter method explained in Sec. 4.4, using a filter width of 1 meV.

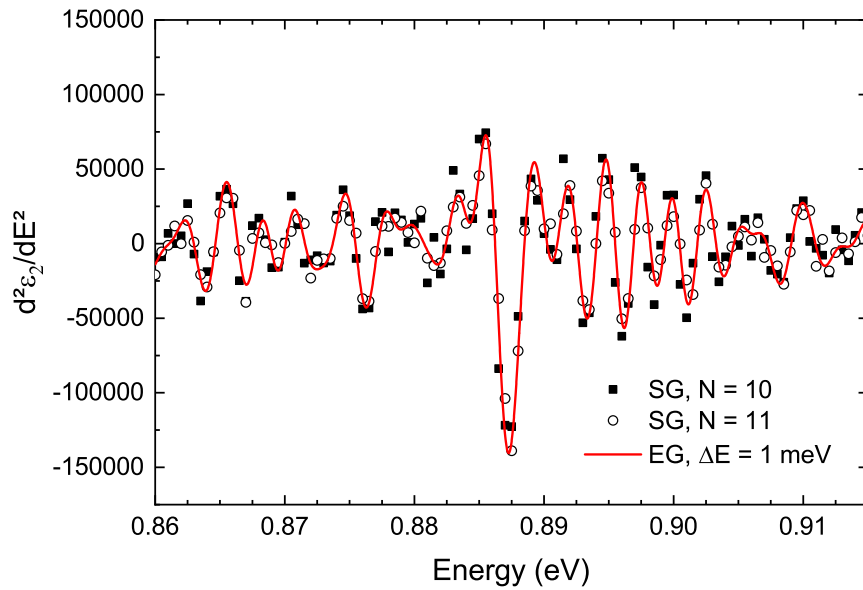


Figure 4.17: Same as Fig. 4.16 for the imaginary part of the dielectric function.

5 TRANSIENT CRITICAL POINT PARAMETERS OF GE AND SI FROM FEMTOSECOND PUMP-PROBE ELLIPSOMETRY

The present chapter is a manuscript in progress.

Carola Emminger,^{1,2} Shirly Espinoza,³ Steffen Richter,^{3,4} Mateusz Rebarz,³
Oliver Herrfurth,^{5,6} Martin Zahradník,³ Rüdiger Schmidt-Grund,^{5,7} Jakob
Andreasson,³ and Stefan Zollner¹

¹*Department of Physics, New Mexico State University, Las Cruces, NM 88003, USA*

²*Department of Condensed Matter Physics, Masaryk University, 61137 Brno, Czech
Republic*

³*ELI Beamlines, Fyzikální ústav AV ČR, 25241 Dolní Břežany, Czech Republic*

⁴*Linköpings universitet, Institutionen för fysik, kemi och biologi, 58183 Linköping,
Sweden*

⁵*Universität Leipzig, Felix-Bloch-Institut für Festkörperphysik, 04103 Leipzig,
Germany*

⁶*Active Fiber Systems GmbH, 07745 Jena, Germany*

⁷*Technische Universität Ilmenau, Institut für Physik, 98693 Ilmenau, Germany*

Abstract

The complex pseudodielectric function of Ge and Si from femtosecond pump-probe spectroscopic ellipsometry with 267, 400, and 800 nm pump pulse wavelengths is analyzed by fitting an analytical lineshape to the second derivatives of the

pseudodielectric function with respect to energy. This yields the critical point parameters (threshold energy, lifetime broadening, amplitude, and excitonic phase angle) of E_1 and $E_1 + \Delta_1$ in Ge and E_1 in Si as functions of time delay. Coherent longitudinal acoustic phonon oscillations with a period of about 11 ps are observed in the transient critical point parameters of Ge. Reasonable agreement of the strain estimated from the amplitudes of the coherent phonon oscillations and the strain calculated from theory is found for Ge measured with the 800 nm pump pulse.

5.1 Introduction

In a recent publication [9], the transient pseudodielectric function of Ge, Si, and InP obtained from femtosecond pump-probe spectroscopic ellipsometry (SE) between 1.7 and 3.5 eV using pump wavelengths of 267, 400, and 800 nm has been presented. Details on the experimental setup and the measurement results have been given in Ref. 9 (the instrumental setup is also described in Ref. 81), however, a quantitative analysis of the data has not been included. Therefore, the goal of this work is to quantitatively investigate the time-resolved critical points (CPs) E_1 and $E_1 + \Delta_1$ in Ge and E_1 in Si from the data provided in Ref. 9. For this purpose, a standard CP lineshape [24,25] is fitted to the second energy derivatives of the pseudodielectric function of both materials to obtain the CP parameters (threshold energy, lifetime broadening, excitonic phase angle, and amplitude) as

a function of time delay.

In the temporal evolution of the CP parameters of Ge, oscillations are observed within the first 30 ps, which are identified as coherent longitudinal acoustic phonon (CAP) oscillations. The origin of such oscillations is a laser-pulse induced strain pulse, which travels through the material [31]. CAP oscillations have been described in the literature [10, 31, 82] and have been measured in many different materials [83–94]. Although in general hard to detect in bulk semiconductors due to the large penetration depth [84], CAP oscillations have been observed, for example, in the pump-probe reflectivity spectra of GaP and Si by Ishioka *et al.* [84], in GaAs by Vinod *et al.* [85] and Han *et al.* [86], and in GaN by Wu *et al.* [87].

In the present study, it is shown that CAP oscillations can also be found in the transient CP parameters of bulk Ge measured by femtosecond pump-probe SE. The analysis method is outlined in Sec. 5.2 and the results are discussed in Sec. 5.3.

5.2 Critical point analysis

The second derivatives of the pseudodielectric function with respect to energy are calculated applying a linear filter method [11, 43, 44, 59] using extended Gauss (EG) functions [45, 46] which are defined as [11]

$$b_m(x) = \left(1 - \frac{a}{1!} \frac{d}{da} + \cdots (-1)^m \frac{a^m}{m!} \frac{d^m}{da^m} \right) a^{-\frac{1}{2}} e^{-\frac{x^2}{4a}}, \quad (69)$$

where $m = 1, \dots, M$ and $\sqrt{a} = \Delta E$ is the width of the filter. Similar to the example given in Eq. (21c) in Ref. 11, one can define an expression using $b_4(x)$ and calculate the second derivatives with respect to energy. The pseudodielectric function is not given in equidistant energy or wavelength steps. Therefore, instead of converting from wavelength to energy, we calculate an average step size $\Delta E'_j = (E_{j+1} - E_{j-1})/2$ at each data point j . The second energy derivative of the data ϵ_j , where ϵ_j can be either the real or imaginary part of the pseudodielectric function $\langle \epsilon \rangle = \langle \epsilon_1 \rangle + i \langle \epsilon_2 \rangle$, is then given by

$$\begin{aligned} \frac{d^2 \bar{\epsilon}_4(E)}{dE^2} \approx & \frac{1}{49152\sqrt{\pi}\Delta E^3} \sum_{j=j_1}^{j_2} \left[\frac{E_{j+1} - E_{j-1}}{2} \epsilon_j e^{-\frac{(E-E_j)^2}{4\Delta E^2}} \right. \\ & \times \left(-110880 + \frac{188496(E-E_j)^2}{\Delta E^2} - \frac{45936(E-E_j)^4}{\Delta E^4} \right. \\ & \left. \left. + \frac{3608(E-E_j)^6}{\Delta E^6} - \frac{106(E-E_j)^8}{\Delta E^8} + \frac{(E-E_j)^{10}}{\Delta E^{10}} \right) \right]. \end{aligned} \quad (70)$$

For J data points, $j_1 = 2$ and $j_2 = J - 1$. The width ΔE of the filter is chosen according to the white noise onset of the Fourier coefficients obtained from a discrete Fourier transform as explained in Ref. 11. To compute the Fourier transform and remove discontinuities at endpoints of the data set we use the method in Ref. 42. The amount of noise in the data determines the white noise region and therefore the filter width. In principle, one would have to determine the filter width for each data set separately. However, since the number of data sets for each material and pump pulse wavelength is > 200 , we determine ΔE at

some selected time delays before, at, and after the pump pulse and choose the filter width that works best for all selected data sets. Table 5.5 lists the chosen filter widths, the range of the step size, the spectral energy range, the energy range used for the fit, and the time range (before to after the pump pulse) for both materials measured with various pump pulse wavelengths.

To fit the analytical lineshapes to the second energy derivatives of $\langle\epsilon_1\rangle$ and $\langle\epsilon_2\rangle$ using Eq. (70), a Levenberg-Marquardt algorithm as explained in Chap. 15.5 in Ref. 61 was implemented in C++. Starting parameters for the eight fit parameters (amplitude, energy, broadening, and phase angle for both E_1 and $E_1 + \Delta_1$) are taken based on values found in the literature [20,23]. At each delay time, all eight parameters are fitted to both $d^2\langle\epsilon_1\rangle/dE^2$ and $d^2\langle\epsilon_2\rangle/dE^2$, by minimizing the sum of the χ^2 merit functions of $d^2\langle\epsilon_1\rangle/dE^2$ and of $d^2\langle\epsilon_2\rangle/dE^2$. The code automatically fits the data sets at all time delays using the same starting parameters for each case.

Figure 5.1 shows the second derivatives at E_1 and $E_1 + \Delta_1$ in Ge measured with an 800 nm pump pulse, calculated from Eq. (70) before ($t = -5$ ps), at ($t = 0$), and at $t = 100$ ps after the pump pulse. Solid lines show the fits with the second derivative of a two-dimensional CP lineshape, which best represents the E_1 and $E_1 + \Delta_1$ CPs [23], given by

$$\frac{d^2\epsilon(E)}{dE^2} = \frac{A_{E_1}e^{i\phi_{E_1}}}{(E - E_1 + i\Gamma_{E_1})^2} + \frac{A_{E_1+\Delta_1}e^{i\phi_{E_1+\Delta_1}}}{(E - (E_1 + \Delta_1) + i\Gamma_{E_1+\Delta_1})^2}. \quad (71)$$

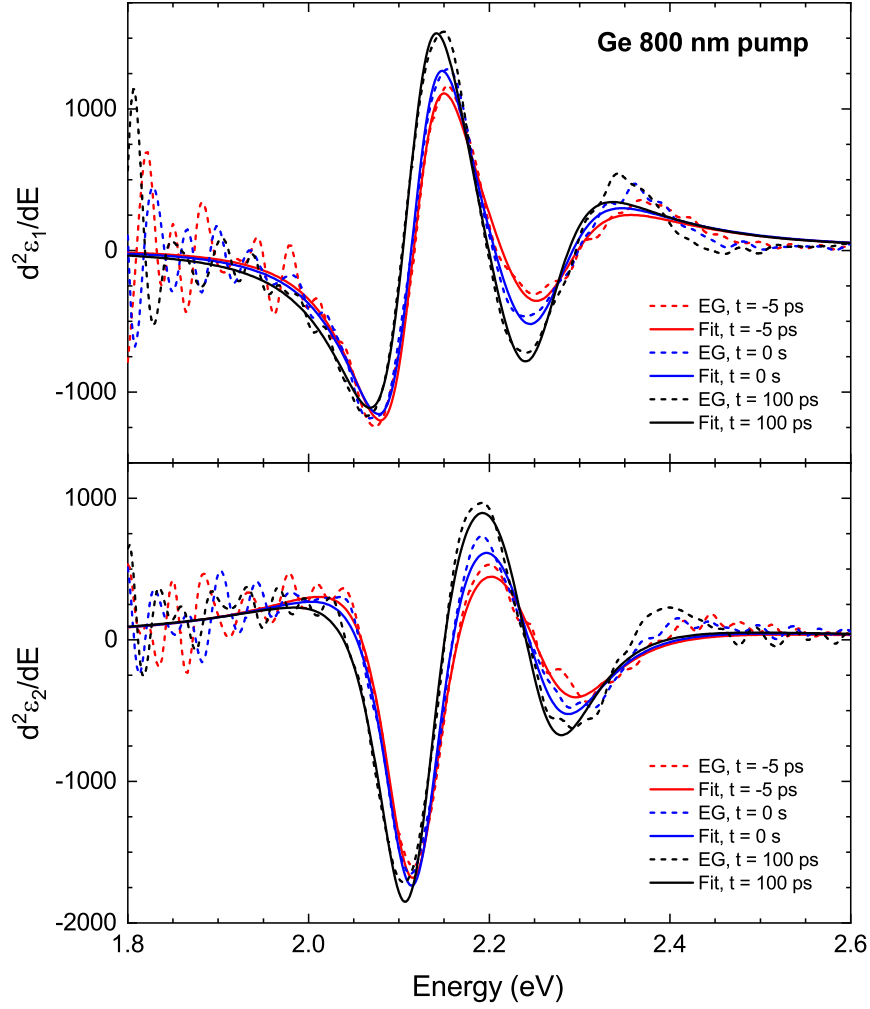


Figure 5.1: Second derivatives with respect to energy of the dielectric function in the region of E_1 and $E_1 + \Delta_1$ of Ge measured with an 800 nm pump pulse at different time delays before (-5 ps), at, and 100 ps after the pump pulse. Dashed lines represent the derivatives obtained as explained in the text. Solid lines represent the fits using two-dimensional lineshapes for E_1 and $E_1 + \Delta_1$.

The fit parameters in Eq. (71) are the amplitudes A_{E_1} and $A_{E_1+\Delta_1}$, the excitonic phase angles ϕ_{E_1} and $\phi_{E_1+\Delta_1}$, the CP energies E_1 and $E_1+\Delta_1$, and the broadenings Γ_{E_1} and $\Gamma_{E_1+\Delta_1}$. In the case of Si, a zero-dimensional (excitonic) lineshape best describes E_1 [95]. Its second energy derivative is given by

$$\frac{d^2\epsilon(E)}{dE^2} = \frac{-2A_{E_1}e^{i\phi_{E_1}}}{(E - E_1 + i\Gamma_{E_1})^3}. \quad (72)$$

The agreement between the fit and the second derivatives calculated from the EG filters deteriorates between 2.3 and 3.5 eV. A possible explanation might be a structure that arises due to phase-filling effects [96] slightly above $E_1 + \Delta_1$. This has been simulated in Ref. 96 for doped Ge with a carrier concentration of 10^{19} cm^{-3} at 77 K. Since the data we investigate in this work were measured at room temperature, we expect the structures shown in Fig. 2 of Ref. 96 to feature a larger spectral broadening for 300 K. Therefore, the extra feature might be the reason of the deviations between the fits and the second derivatives above 2.3 eV in Fig. 5.1, because the extra feature is not taken into account using the standard two-dimensional CP lineshape.

5.3 Results and discussion

Figures 5.2 and 5.3 depict the CP parameters as a function of delay time of Ge and Si, respectively. The vertical line marks the time $t = 0$ of the pump pulse. It should be noted that the time delay steps were not chosen to be constant. For

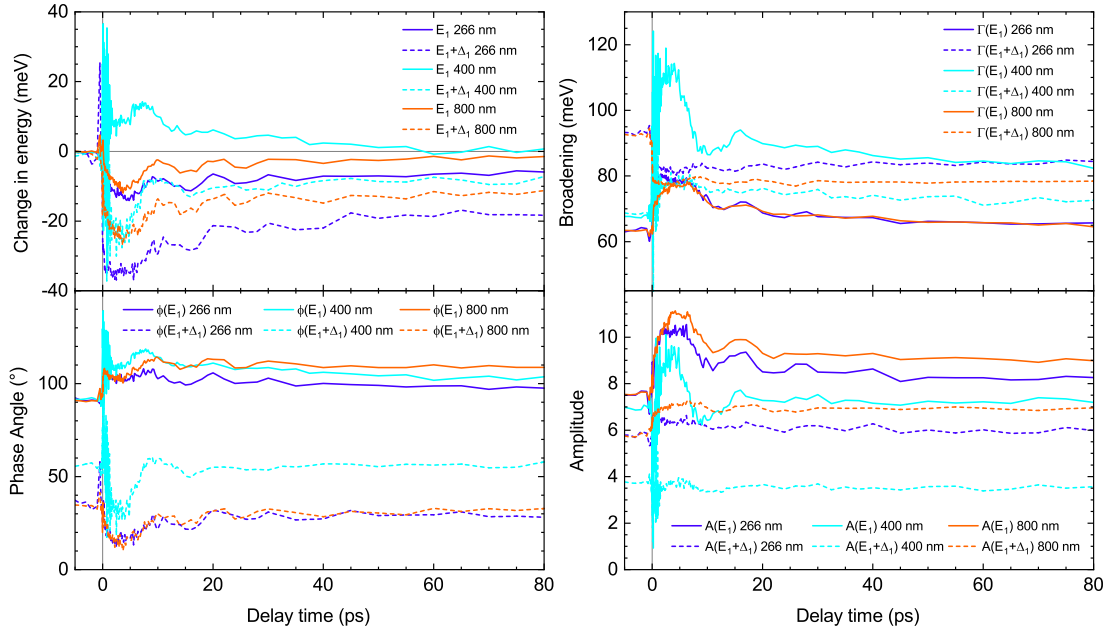


Figure 5.2: Temporal evolution of the critical point parameters of E_1 (solid) and $E_1 + \Delta_1$ (dashed) in Ge measured with 267 (purple), 400 (cyan), and 800 nm (orange).

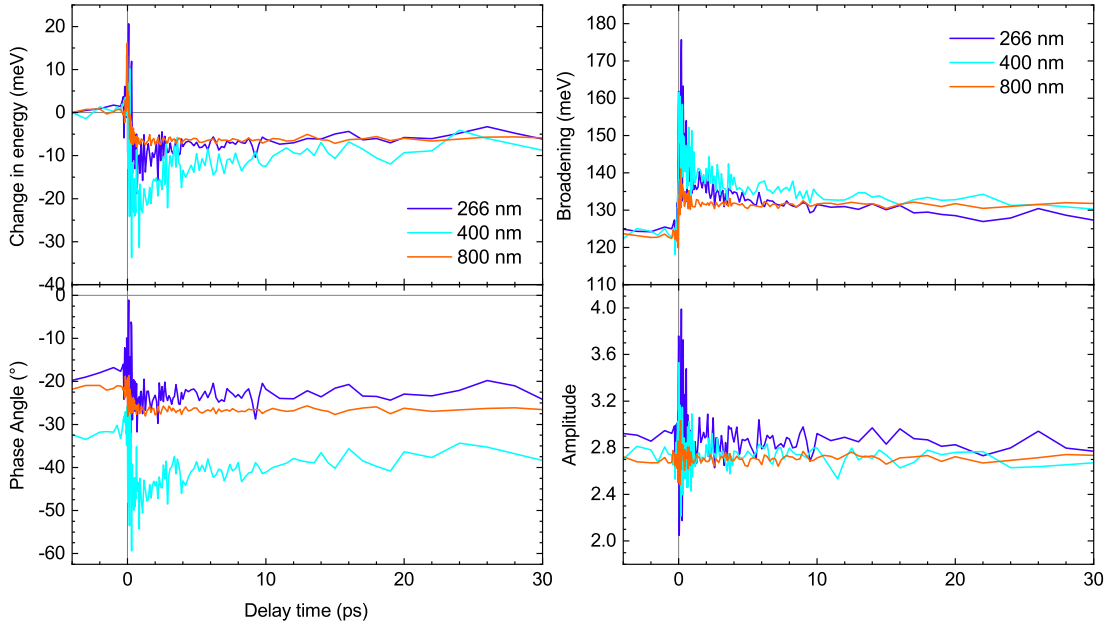


Figure 5.3: Same as Fig. 5.2 for E_1 in Si.

Ge measured with the 800 nm pump pulse, for instance, the time delay steps were 10-50 fs between $t = -0.3$ and 1 ps, 100-250 fs between $t = 1$ and 10 ps, 1-2 ps between $t = 11$ to 30 ps, and 5-100 ps ($t > 30$ ps).

We make several observations in the CP parameters of Ge. The E_1 and $E_1 + \Delta_1$ energies redshift after the pump pulse (except E_1 measured with $\lambda_{\text{pump}} = 400$ nm) and start to recover after about 4 ps. The redshift of the energies might be partly explained by a temperature increase due to laser heating, where the expected temperature increase is $\Delta T \approx 25$ K for the $\lambda_{\text{pump}} = 800$ nm data [9].

The amplitudes of both E_1 and $E_1 + \Delta_1$ increase, while the phase angles and broadenings show opposite behavior for the two CPs. The E_1 broadening increases, while the $E_1 + \Delta_1$ broadening decreases after the pump pulse. In general, it seems that some parameters recover faster than others (for example, the $E_1 + \Delta_1$ amplitude measured with $\lambda_{\text{pump}} = 400$ nm). The data set measured with a pump wavelength of 400 nm shows an artifact at about 1.8 eV which might affect the CP parameters.

In the case of Si, we observe a redshift of E_1 and an increase in broadening, which might be explained by laser heating. A redshift of 6 meV corresponds to a temperature rise of about 20 K, and an increase in broadening of about 7 meV corresponds to $\Delta T \approx 30$ K [95]. The amplitudes return to the values before the pump pulse after only 1-2 ps, while the recovery of the other parameters takes much longer (> 100 ps). A decrease of the phase angles might be explained by a

decrease of excitonic effects due to screening by the laser induced increased carrier concentration.

Within the first 30 ps, CAP oscillations with a period of about 11 ps are observed in the CP parameters of Ge. The period of CAP oscillations is given by [82]

$$T = \frac{\lambda}{2nv_s \cos \theta}, \quad (73)$$

where λ is the wavelength of the probe beam, n is the refractive index inside the material at λ , v_s is the sound velocity (given in Tab. 5.1), and θ is the angle of refraction. Due to the large refractive index, the angle inside the material is small

Table 5.1: Material parameters of Ge and Si at room temperature.

Parameter	Ge	Si	Ref.
B (N/cm ²)	7.5×10^6	9.8×10^6	97
β (1/K)	5.9×10^{-6}	2.6×10^{-6}	98, 99
C (J/(cm ³ ·K))	1.68	1.68	100
$\frac{\partial E_g}{\partial P}$ (eV/Pa)	5.0×10^{-11}	-1.5×10^{-11}	101
D_1^1 (eV)	-8.1		32
D_3^3 (eV)	5.9		32
v_s (cm/s)	4.87×10^5	8.43×10^5	102

according to Snell's law and we can approximate

$$T \approx \frac{\lambda}{2nv_s}. \quad (74)$$

Table 5.2: Wavelength λ and refractive index n at the E_1 and $E_1 + \Delta_1$ critical points of Ge and E_1 of Si, along with the period T of coherent longitudinal acoustic phonon oscillations calculated from Eq. (74) and the penetration depth ζ .

	λ (nm)	n	T (ps)	ζ (nm)
E_1 in Ge	586.5 ^a	5.68 ^b	10.6	28
$E_1 + \Delta_1$ in Ge	536.7 ^a	5.01 ^b	11.0	18
E_1 in Si	365.3 ^c	6.53 ^b	3.32	11

^aRef. 20

^bRef. 103

^cRef. 95

Table 5.2 lists the probe wavelengths and corresponding refractive indices at E_1 and $E_1 + \Delta_1$ of Ge and E_1 of Si, as well as the period calculated from Eq. (74).

The energy shifts shown in Fig. 5.2 can be fitted with the sum of a damped oscillator (similar to Ref. 84) and an exponential decay

$$\Delta E(t) = -\Delta E_a \cos\left(\frac{2\pi t}{T} - \delta\right) e^{-\frac{t}{\tau_a}} - \Delta E_b e^{-\frac{t}{\tau_b}}. \quad (75)$$

Figures 5.4 and 5.5 show the fit to the energy shifts ΔE_1 and $\Delta(E_1 + \Delta_1)$ obtained from fitting the 800 nm-pump data with Eq. (75). The fits were performed between 1 and 30 ps, i.e. ignoring the strong increase and decrease within the first picosecond since the CAP oscillations take time to build up, as has been shown for GaP and Si by Ishioka *et al.* [84], for instance. The fit parameters are listed in Tab. 5.3. The period of the oscillatory term of Eq. (75), which is

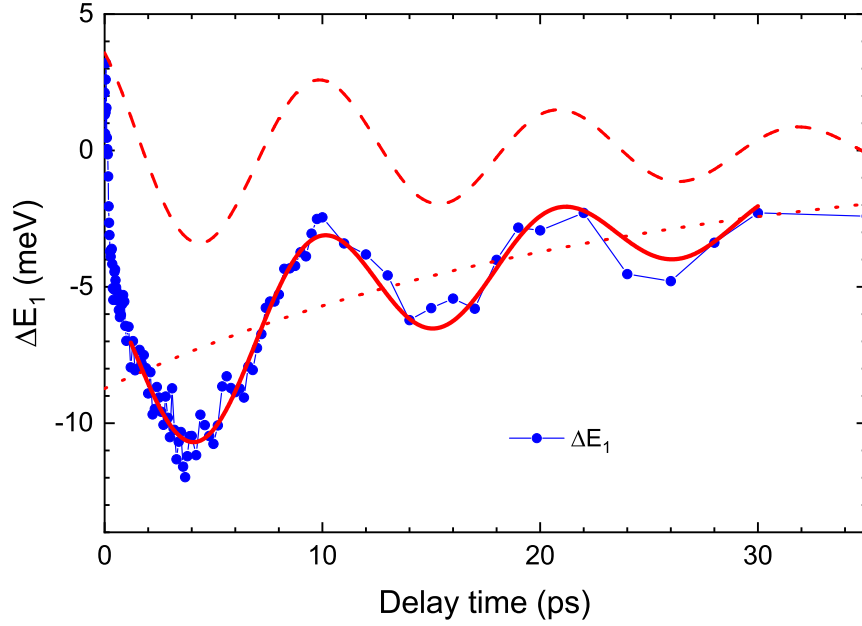


Figure 5.4: Shift ΔE_1 (change of the E_1 energies) with time delay of Ge measured with the 800 nm pump pulse. The solid line represents a fit with Eq. (75). The first ($\Delta E_a(t)$) and second ($\Delta E_b(t)$) terms in Eq. (75) are represented by the dashed and dotted lines, respectively.

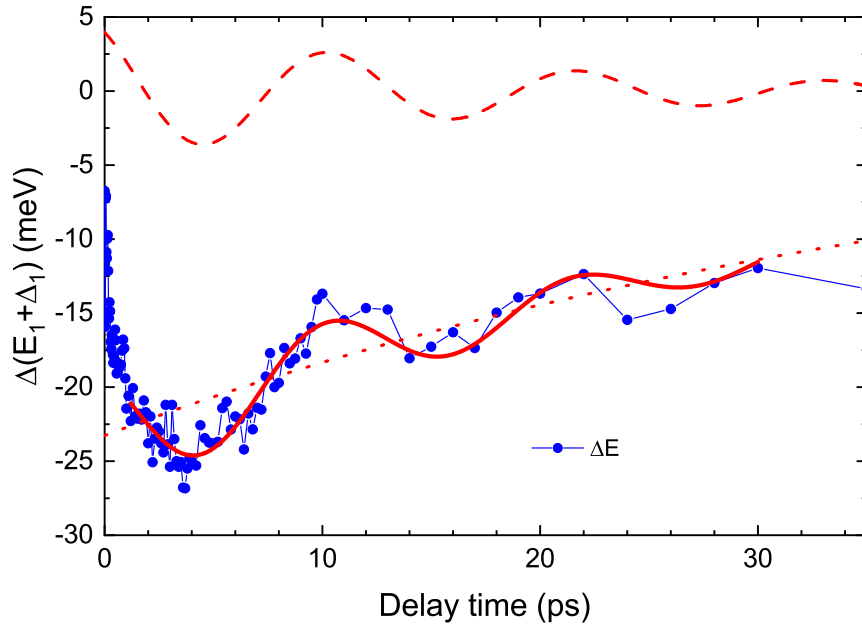


Figure 5.5: Same as Fig. 5.4 for $\Delta(E_1 + \Delta_1)$ (change of the $E_1 + \Delta_1$ energies).

Table 5.3: Parameters obtained from fitting Eq. (75) to the E_1 and $E_1 + \Delta_1$ shifts of Ge measured with the 800 nm pump pulse between 1 and 30 ps (Figs. 5.4 and 5.5).

	$\Delta(E_1)$	$\Delta(E_1 + \Delta_1)$
ΔE_a (meV)	4.2 ± 0.4	4.7 ± 0.8
ΔE_b (meV)	8.7 ± 0.3	23.3 ± 0.5
T (ps)	11.0 ± 0.2	11.4 ± 0.4
δ	2.58 ± 0.06	2.6 ± 0.1
τ_a (ps)	20 ± 4	18 ± 7
τ_b (ps)	23 ± 2	42 ± 3

represented by the dashed lines in Figs. 5.4 and 5.5, agrees very well with the calculated CAP periods given in Tab. 5.2. While the shift of $E_1 + \Delta_1$ is about twice as strong as ΔE_1 , the amplitude ΔE_a of the oscillatory term is about the same for both CPs. Adding and subtracting the two amplitudes ΔE_a can be used to estimate the strain inside the material due to the strain dependence of the E_1 and $E_1 + \Delta_1$ CPs via [36]

$$\Delta E_1 = \frac{\Delta_1}{2} + \Delta E_H - \sqrt{\frac{(\Delta_1)^2}{4} + (\Delta E_S)^2} \quad (76)$$

and

$$\Delta(E_1 + \Delta_1) = -\frac{\Delta_1}{2} + \Delta E_H + \sqrt{\frac{(\Delta_1)^2}{4} + (\Delta E_S)^2}, \quad (77)$$

where ΔE_H is the hydrostatic shift and ΔE_S is the shear splitting given by [36]

$$\Delta E_H = \sqrt{3}D_1^1\epsilon_H \quad (78)$$

and

$$\Delta E_S = \sqrt{6}D_3^3\epsilon_S. \quad (79)$$

The hydrostatic strain ϵ_H and shear strain ϵ_S depend on the in-plane (ϵ_{\parallel}) and out-of-plane (ϵ_{\perp}) strains in the following way [36]

$$\epsilon_H = \frac{\epsilon_{\perp} + 2\epsilon_{\parallel}}{3}, \quad (80)$$

$$\epsilon_S = \frac{\epsilon_{\perp} - \epsilon_{\parallel}}{3}. \quad (81)$$

Assuming that the film is elastically isotropic and the stress only depends on z , the only nonzero component of the elastic strain tensor is ϵ_{33} [10], which can be set equal to the out-of-plane strain $\epsilon_{33} = \epsilon_{\perp}$, while ϵ_{\parallel} is assumed to be zero. Adding Eqs. (76) and (77) and setting it equal to the sum of the two amplitudes ΔE_a given in Tab. 5.3, results in $\Delta E_H = 4.5$ meV. The hydrostatic strain can then be calculated using D_1^1 listed in Tab. 5.1, $\epsilon_H = -3.2 \times 10^{-4}$, which gives $\epsilon_{\perp} \approx -1.0 \times 10^{-3}$. Similarly, subtracting (77) from (76) gives

$$\Delta_1 - 2\sqrt{\frac{(\Delta_1)^2}{4} + (\Delta E_S)^2} = -0.5 \text{ meV}, \quad (82)$$

which is used to estimate the shear shift $|\Delta E_S| = 7.0$ meV and the out-of-plane strain $\epsilon_{\perp} \approx -1.5 \times 10^{-3}$.

To compare these results with the strain expected from theory, the expression for the electron-hole and phonon contributions to the stress σ_{ij} given in Eqs. (17) and (18) in Ref. 10 are used, which are

$$\sigma_{ij}^e = -B \frac{\partial E_g}{\partial P} \delta_{ij} N \quad (83)$$

and

$$\sigma_{ij}^p = -\frac{3B\beta}{C} (E - E_g) \delta_{ij} N, \quad (84)$$

where B is the bulk modulus, $\partial E_g / \partial P$ is the pressure dependence of the indirect band gap E_g , β is thermal expansion coefficient, N is the number of photoexcited electron-hole pairs per unit volume, C is the specific heat in units of $\text{J}/(\text{cm}^3 \cdot \text{K})$, and E is the photon energy of the pump beam. The ratio of electronic and phonon contributions

$$\frac{\sigma_{ii}^e}{\sigma_{ii}^p} = -\frac{C}{3\beta} \frac{\partial E_g}{\partial P} \frac{1}{(E - E_g)} \quad (85)$$

to the stress for different pump wavelengths is given in Tab. 5.4. For the 800 nm

Table 5.4: Ratio $\sigma_{ii}^e / \sigma_{ii}^p$ of the electron and phonon contributions to stress.

Pump wavelength	Ge	Si
800 nm	5.3	-7.5
400 nm	2.0	-1.6
267 nm	1.2	-0.9

pump pulse, the electron-hole contribution is much larger, while for the 267 nm

pulse, the two contributions are about the same. The relation between the strain and the stress tensor components, ϵ_{33} and $\sigma_{11} = \sigma_{22} = \sigma_{33} = \sigma$, is given by the compliance tensor components for diamond symmetry (O_h space group) [34, 35]

$$\epsilon_{33} = (S_{11} + 2S_{12})\sigma. \quad (86)$$

The compliance tensor components can be calculated from $S_{11} + 2S_{12} = (C_{11} + 2C_{12})^{-1}$ [21], where C_{11} and C_{12} are components of the stiffness tensor, which are $C_{11} = 1.285 \times 10^7$ N/cm² and $C_{12} = 0.483 \times 10^7$ N/cm² for Ge (see Tab. 3.6a in Ref. 21). This gives for Ge measured with the 800 nm pump pulse

$$\epsilon_{\text{el}} = (S_{11} + 2S_{12}) \left(-B \frac{\partial E_g}{\partial P} N \right) \approx -6.4 \times 10^{-4} \quad (87)$$

and

$$\epsilon_{\text{ph}} = (S_{11} + 2S_{12}) \left(-\frac{3B\beta}{C} (E - E_g) \right) \approx -1.2 \times 10^{-4}. \quad (88)$$

The total strain $\epsilon_{33} = \epsilon_{\text{el}} + \epsilon_{\text{ph}} = -7.6 \times 10^{-4}$ compares reasonably well to the out-of-plane strain of $\epsilon_{\perp} \approx -1.0 \times 10^{-3}$ and $\epsilon_{\perp} \approx -1.5 \times 10^{-3}$ estimated from the energy shift amplitudes ΔE_a . Using Eqs. (76) and (77), the calculated energy shifts are $\Delta E_1 = -3.6$ meV and $\Delta(E_1 + \Delta_1) = -3.5$ meV.

In the case of Si, the calculated strain is on the order of 7×10^{-6} for the 267 and 800 nm pump pulse data sets, and 2×10^{-5} for the data measured with the 400 nm pump pulse. Due to the negative pressure dependence of the indirect gap, which is $\partial E_g / \partial P = \partial E_{\Gamma X} / \partial P = -1.5$ eV/Pa [101], the electron-hole and phonon

contributions do not add up as in the case of Ge, but partly cancel one another. Another explanation for the absence of CAP oscillations in Si might be the larger velocity of sound, which causes the strain pulse to leave the probed volume faster than for Ge.

5.4 Summary

The pseudodielectric function of Ge and Si measured with pump-probe spectroscopic ellipsometry is analyzed by fitting analytical critical point lineshapes to the second derivatives with respect to energy of the data. Energies, broadenings, excitonic phase angles, and amplitudes of the E_1 and $E_1 + \Delta_1$ critical points in Ge and E_1 in Si are shown as functions of time delay. In the temporal evolution of E_1 and $E_1 + \Delta_1$ in Ge, coherent longitudinal acoustic phonon oscillations are observed. The measured period of 11 ps compares very well with the expected value. The out-of-plane strain estimated from the amplitude of the oscillations in the energy shifts is in reasonable agreement with the strain calculated from theory. Coherent phonon oscillations are not detected in the case of Si, probably due to the shorter wavelength of E_1 and larger velocity of sound compared to Ge, which is related to the decay of the oscillations. Future work will address effects related to the laser-induced carrier density by considering band gap renormalization, band filling, and Burstein-Moss shifts.

Supplementary material

The supplementary material includes further considerations regarding the absence of coherent acoustic phonon oscillations in Si and optical phonon oscillations in Ge.

Acknowledgments

The authors would like to thank Christopher J. Stanton for his help with the interpretation of the results. This work was supported by Air Force Office of Scientific Research under award number FA9550-20-1-0135 and the National Science Foundation (No. DMR-1505172).

5.5 Supplementary material

5.5.1 Notes on experiment and data analysis

Experimental parameters and chosen filter widths used for the computation of the second energy derivatives as discussed in Sec. 5.2 are given in Tab. 5.2. Figure 5.6 depicts the real and imaginary parts of the pseudo-DF of Ge measured with an 800 nm pump pulse. While the CAP oscillations are present in the pseudo-DF at a probe energy of $E = 2.06$ eV, they are barely observable at $E = 2.27$ eV, i.e. at $E_1 + \Delta_1$. In the CP energies obtained from the second derivative analysis, on the other hand, the oscillations are more pronounced than in the pseudo-DF, especially after about 20 ps, and are even found in the case of $E_1 + \Delta_1$.

5.5.2 Coherent phonon oscillations

Coherent acoustic phonon oscillations arise from interference of the probe beam reflected from the surface and upon the strain pulse, which moves through the material [84]. We expect to see oscillations related to the time it takes for the strain pulse to leave the probed volume, $\tau = \zeta/v_s$, i.e. we assume a damping of $e^{-v_s t/\zeta}$, where ζ is the penetration depth. Figure 5.7 depicts the intensity decay inside the material according to Beer's law, $I(z) = I_0 e^{-\alpha z}$ (α is the absorption coefficient), for the different probe and pump wavelengths. The horizontal line marks the intensity $I(\zeta) = I_0/e$, which is the intensity at the penetration depth

Table 5.5: Filter width ΔE and range of step size for the data sets of Ge and Si measured with $\lambda_{\text{pump}} = 800, 400,$ and 267 nm pump pulse wavelengths.

λ_{pump}	ΔE (meV)	Step size (meV)	Spectral range (eV)	Fitted range (eV)	Time range (ps)
Ge 800 nm	12	1.5...3.5	1.55...3.67	1.80...2.60	-5...4000
Ge 400 nm	10	2.0...7.3	1.01...3.72	1.60...2.90	-7...5000
Ge 267 nm	15	1.3...3.5	1.53...3.99	1.80...2.60	-5...5000
Si 800 nm	20	2.0...7.4	1.01...3.83	3.15...3.65	-7...5400
Si 400 nm	30	1.9...7.3	1.01...3.94	3.15...3.65	-7...5400
Si 267 nm	20	2.0...7.9	0.95...3.67	3.15...3.55	-5...2600

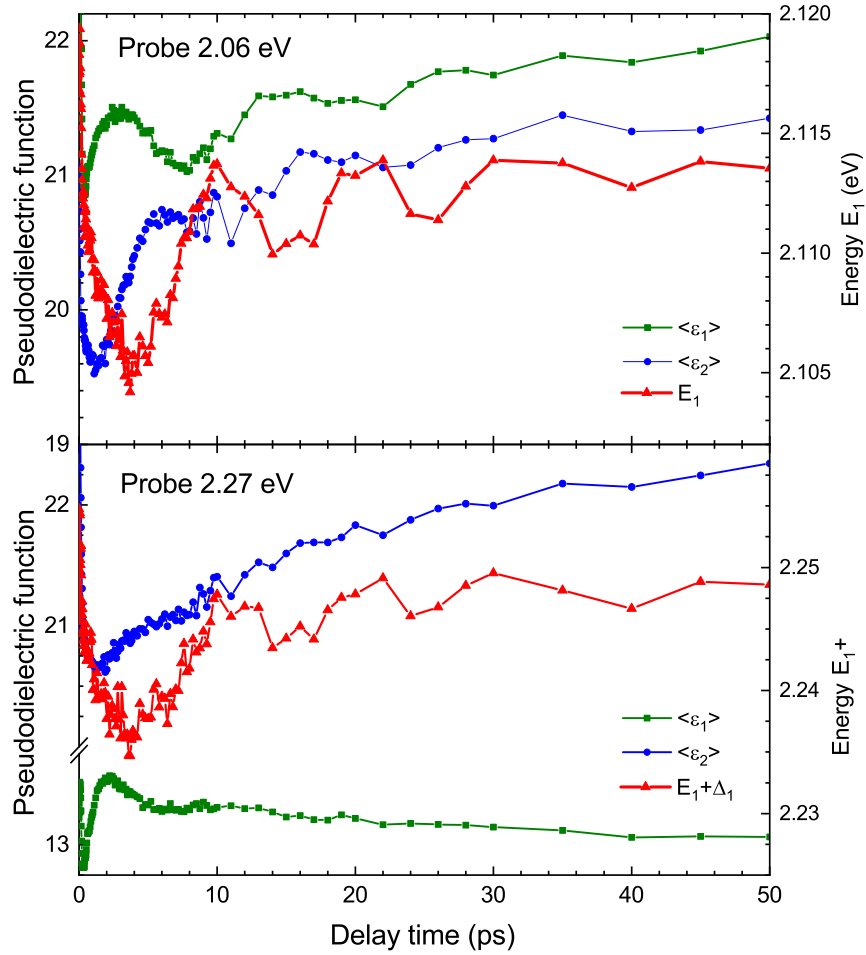


Figure 5.6: Real (squares) and imaginary (dots) parts of the pseudodielectric function of Ge measured with an 800 nm pump pulse at probe energies of 2.06 eV (top) and 2.27 eV (bottom) close to E_1 and $E_1 + \Delta_1$ as functions of delay time along with the E_1 and $E_1 + \Delta_1$ critical point energies obtained from the second derivative analysis explained in the text.

$\zeta = 1/\alpha$. Figure 5.8 shows the damped oscillator $\cos(2\pi ft)e^{-t/\tau}$ calculated with $\tau = \zeta/v_s$ and $f = 1/T$ given in Tab. 5.2 for the E_1 and $E_1 + \Delta_1$ critical points in Ge and E_1 in Si. For a probe wavelength of $\lambda = 587$ nm (E_1 in Ge), two minima within the first 20 ps are present, while we find three minima within 30 ps for E_1 and $E_1 + \Delta_1$ in Ge (see Fig. 5.6). In the case of Si, the damped oscillator has only one distinct minimum for $\tau = \zeta/v_s$, which could explain why no phonon oscillations in the critical point parameters of Si can be identified, since the first few picoseconds are dominated by noise (as can be seen in Fig. 5.3), in particular for the data measured with pump pulse wavelengths of 267 and 400 nm. A comparison of the damped oscillator and the E_1 energy as a function of time delay of Si is provided in Fig. 5.9.

Coherent optical phonon oscillations have been reported in (001)-oriented Ge [104], GaP and Si [84], single crystal Sb [105], graphite [106], and single crystal Zn [107]. Pfeifer *et al.* [104] find a frequency of 9.086 ± 0.001 THz, which matches the optical phonon modes [78] at $k = 0$. In the case of Ge measured with an 800 nm pump pulse, we observe oscillations within the first 500 fs, as illustrated in Fig. 5.10, with a period between 100 and 150 fs, i.e. a frequency of 7-10 THz. However, this is the only data set of the ones investigated which shows oscillations with a frequency close to optical phonon frequencies in this time interval, and further measurements are required to investigate if optical phonon oscillations can be detected for Ge, or if the origin of these oscillations is of a different (maybe

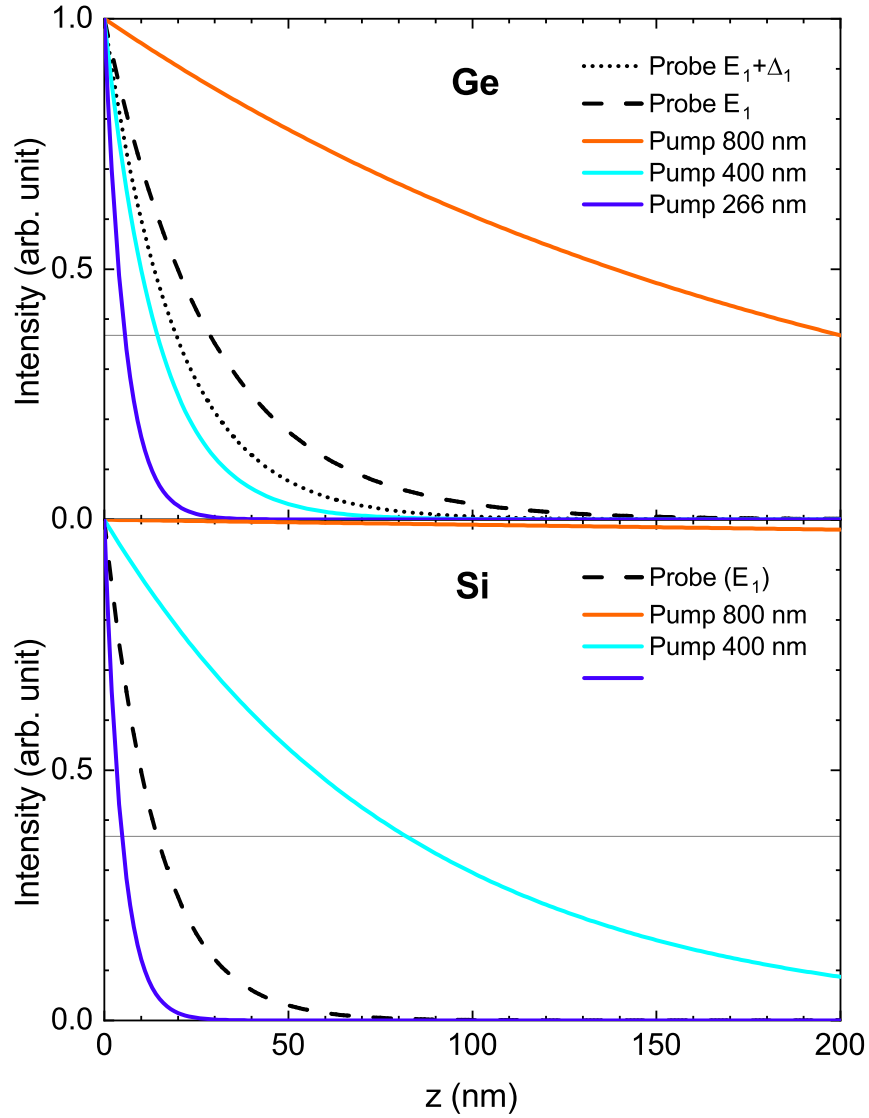


Figure 5.7: Attenuation of the intensity inside the material of the probe and pump light beams in Ge (top) and Si (bottom). The probe intensities are calculated for the E_1 (dashed) and $E_1 + \Delta_1$ (dotted) wavelengths. The horizontal line marks the penetration depth $d = I_0/e$.

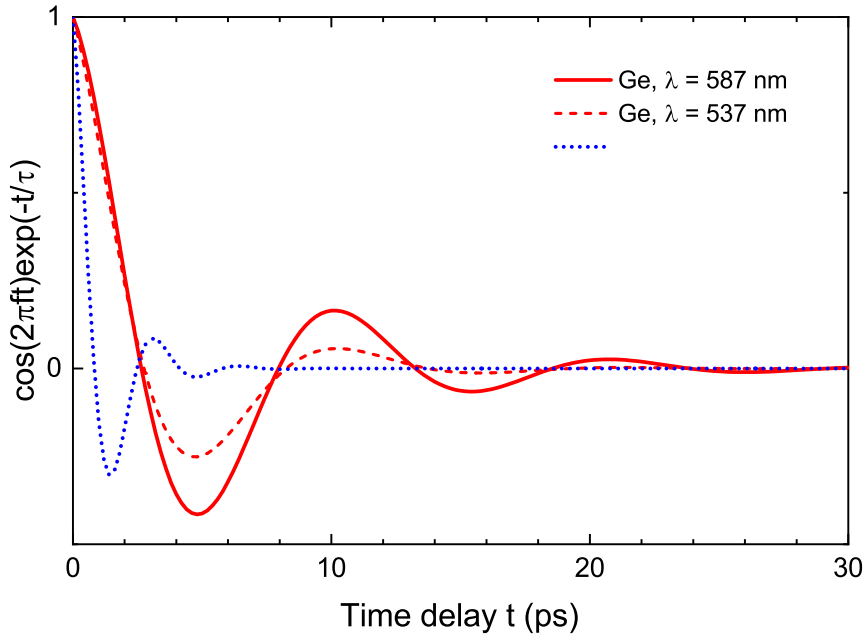


Figure 5.8: Damped oscillator $\cos(2\pi ft)e^{-t/\tau}$ with $\tau = \zeta/v_s$ and $f = 1/T$ calculated using the parameters given in Tab. 5.2 for E_1 (solid) and $E_1 + \Delta_1$ (dashed) of Ge and E_1 of Si (dotted), where $1/f = T$ is the period of coherent acoustic phonon oscillations.

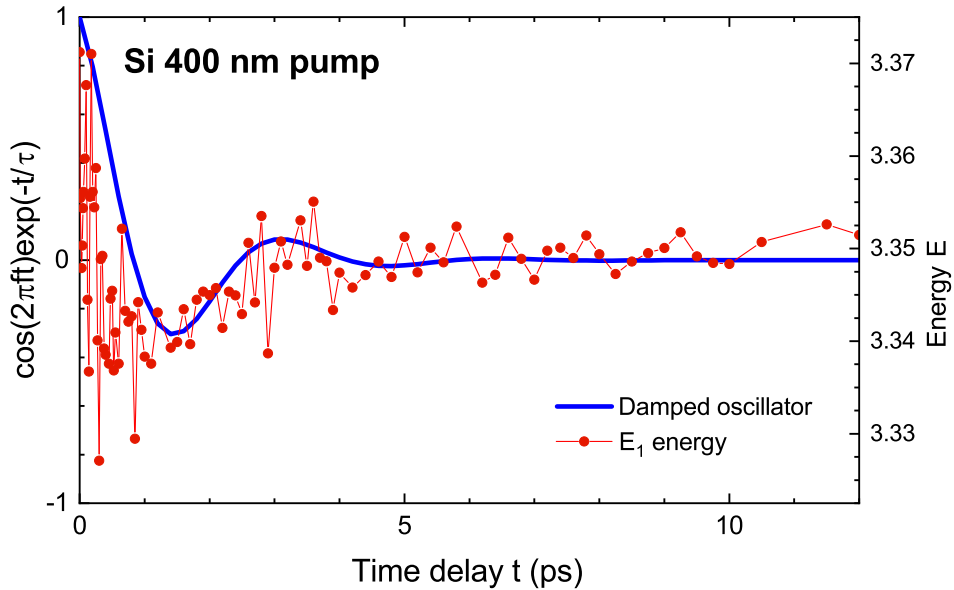


Figure 5.9: Comparison of a damped oscillator $\cos(2\pi ft)e^{-t/\tau}$ where $f = 1/T$ and $\tau = \zeta/v_s$ with T and ζ listed in Tab. 5.2 compared to the E_1 energy of Si measured with a 400 nm pump pulse.

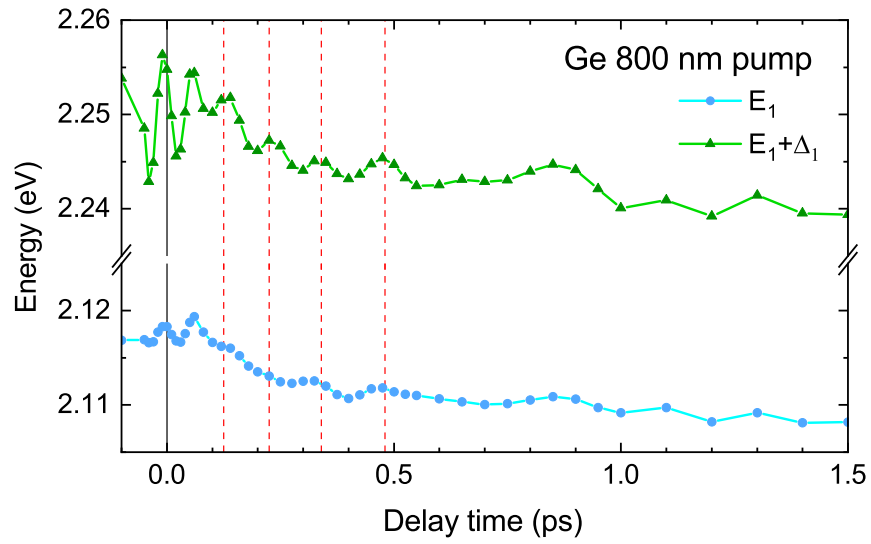


Figure 5.10: Oscillations in the E_1 and $E_1 + \Delta_1$ energies of Ge measured with an 800 nm-pump pulse as functions of delay time. The period of these oscillations is found to be between 100 and 150 fs.

instrumental) nature.

6 CONCLUSION

The major part of the present work has been the quantitative analysis of the dielectric function of semiconductors obtained from spectroscopic ellipsometry and time-resolved femtosecond pump-probe ellipsometry in order to study how critical points are affected by temperature, as well as photoexcitation by an ultrashort laser pulse.

Excitonic effects at the direct band gap of Ge have been modelled using the Hulthén-Tanguy theory, which has resulted in very good agreement between the fit and the data. These results are remarkable in respect of several simplifications applied to the theory, as well as the fact the amplitude was not treated as an adjustable parameter, but instead calculated based on $k \cdot p$ theory and material parameters from the literature. Considering non-parabolicity and warping will make it possible to apply the model to other semiconductors as well and will be addressed in future work.

The linear filter technique defined in Ref. 11 has shown to be a practical method to calculate second energy derivatives by providing a tangible way of choosing a suitable amount of smoothing. It is in particular convenient to be applied to the data measured with femtosecond pump-probe ellipsometry, since they are not given in equidistant energy or wavelength steps. Investigating the second derivatives makes it possible to draw more reliable conclusions on how the

energies, broadenings, phase angles, and amplitudes of the transient critical points change with time delay. The second-derivative analysis of the time-resolved data of Ge and Si from [9] has shown that all critical point parameters are affected by photoexcitation with an ultrafast laser pulse, and that coherent acoustic phonon oscillations play a role in the case of Ge. Future work will include the study of other materials, e.g. GaSb, InP, or germanium-tin alloys, measured with the pump-probe setup at ELI Beamlines, and will also address other effects, such as band gap renormalization and band filling effects.

APPENDIX

A.1 Digital linear filters

In this section, a few more comments on the data analysis are provided. Let's first repeat the definition of the direct space convolution [11]

$$\bar{f}(E) = \int_{-\infty}^{\infty} dE' f(E') b_M(E - E') \quad (\text{A1})$$

with the EG-filters [11]

$$b_M(x) = \left(1 - \frac{a}{1!} \frac{d}{da} + \frac{a^2}{2!} \frac{d^2}{da^2} - \dots + (-1)^M \frac{a^M}{M!} \frac{d^M}{da^M} \right) a^{-\frac{1}{2}} e^{-\frac{x^2}{4a}} \quad (\text{A2})$$

where $a = 1/\Delta k^2$. Wavelength-to-energy conversion can be achieved by substituting Eq. (A2) into Eq. (A1) and approximating the integral as a sum over the data points $f(\lambda_j)$, where $\Delta k = 1/\Delta E$ [11]

$$\bar{f}(E) = \int_{-\infty}^{\infty} dE' f(E') b_M(E - E') = hc \int_{-\infty}^{\infty} \frac{d\lambda}{\lambda^2} f(\lambda) b_M\left(E - \frac{hc}{\lambda}\right), \quad (\text{A3})$$

which can be written as

$$\bar{f}(E) \approx hc(\Delta\lambda) \sum_{j=-\infty}^{\infty} \frac{1}{\lambda_j^2} f(\lambda_j) b_M\left(E - \frac{hc}{\lambda}\right). \quad (\text{A4})$$

Using Eq. (A4), a data set given in equidistant wavelength steps can be converted to a data set equidistant in energy and noise can be effectively suppressed at the same time [11], which is illustrated in Fig. A.1 for a model data set (“false” data) with random numbers added to simulate noise. It can be seen in Fig. A.1 that the

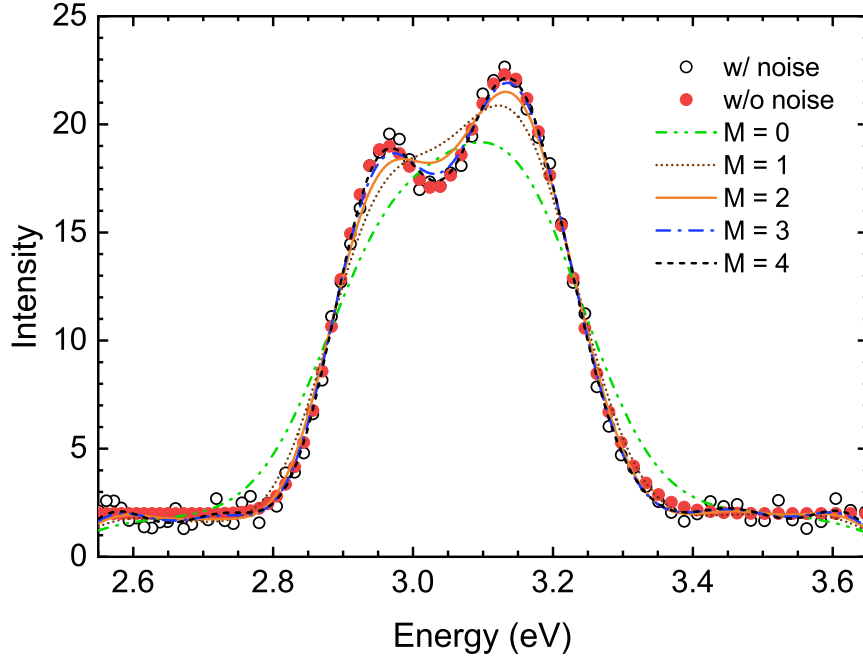


Figure A.1: Wavelength-to-energy conversion using Eq. (A4) for various $M = 0, \dots, 4$ (lines) of model data with noise (open circles). Solid circles represent the model data without noise.

agreement between Eq. (A4) and the data increases for higher M . As pointed out by Le *et al.* [11], $M = 4$ sufficiently suppresses noise and reconstructs the original function. In principle, the agreement should increase further for larger values of M . However, for the data sets investigated in this work, no real improvement could be obtained by using $M > 4$.

A.1.1 Second energy derivatives

Savitzky-Golay [37] (SG) coefficients can be used to numerically calculate second derivatives of the dielectric function with respect to energy. Figure A.2 and A.3 show the second derivatives of the dielectric function of Ge measured at 500 K [16] calculated using SG coefficients and fitted with a 0D, 1D, and 2D lineshape for comparison. The best agreement is given for a 2D-lineshape, in agreement with Ref. 23.

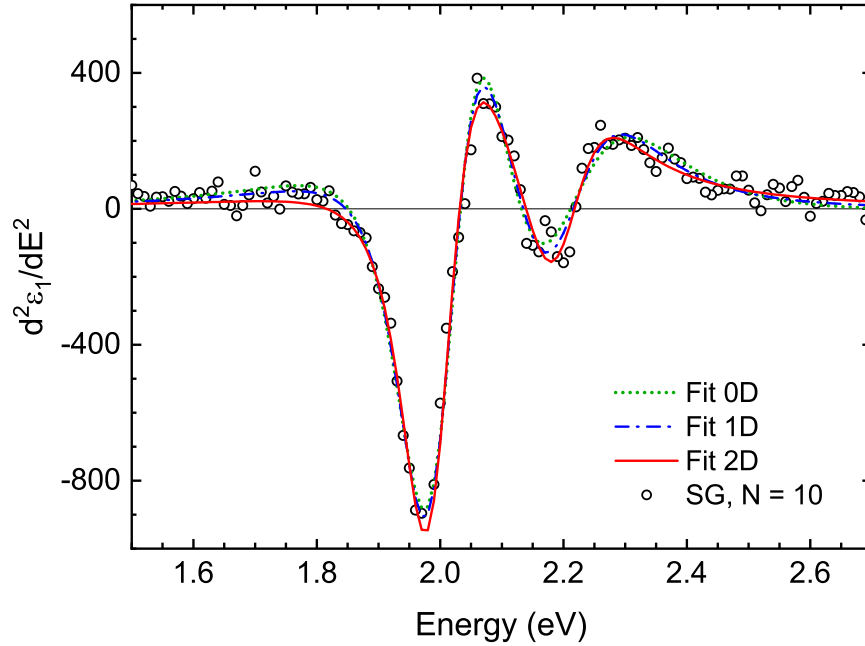


Figure A.2: Second derivative with respect to energy of the real part of the dielectric function of Ge measured at 500 K from Ref. 16 in the range of E_1 and $E_1 + \Delta_1$ (symbols). The second derivatives were obtained using Savitzky-Golay [37] (SG) coefficients using a polynomial of third degree over $N = 10$ data points. Lines represent the best fit to the data points using the second derivative of a 0D (dotted), 1D (dash-dotted), and 2D (solid) CP lineshape (Eq. (15)).

As mentioned in the main part of the present work, there are several advantages

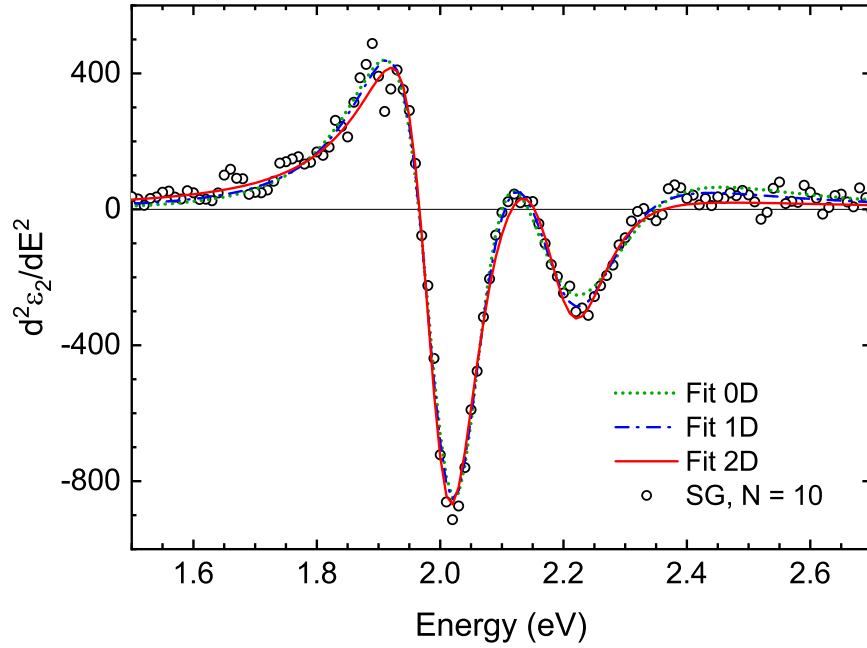


Figure A.3: Same as Fig. A.2 but for the imaginary part of the dielectric function of Ge measured at 500 K from Ref. 16.

of using the linear filter method introduced by Le *et al.* [11]. Figures A.4 and A.5 show the second derivatives of the dielectric function of Ge measured at 500 K [16] calculated using the SG (symbols) and EG (dotted line) methods. It should be noted that the amount of smoothing for these two cases is relatively large.

In order to determine the width of the EG linear filter, I applied the method by Yoo and Aspnes [42] for the computation of the discrete Fourier transform including the removal of discontinuities at the endpoint of the segment of interest to the various data sets using *Mathematica*.

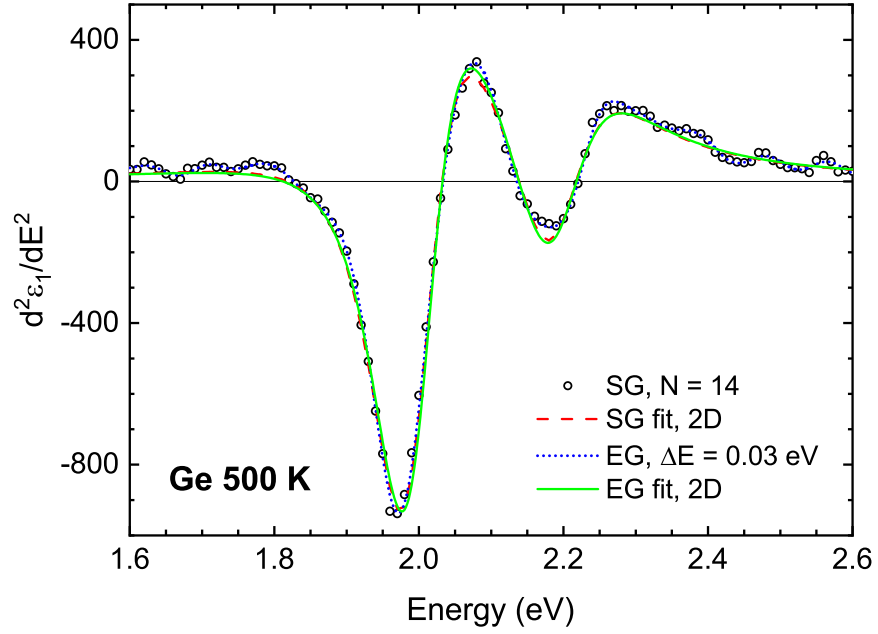


Figure A.4: Second derivative with respect to energy of the real part of the dielectric function of Ge measured at 500 K from Ref. 16 in the range of E_1 and $E_1 + \Delta_1$. The second derivatives were obtained using Savitzky-Golay [37] (SG) coefficients using a polynomial of third degree over $N = 14$ data points (symbols) and the EG-filers defined in Eq. 70 (dotted line). Dashed and solid lines represent the best fit to the SG and EG derivatives using the second derivative of a 2D CP line shape.

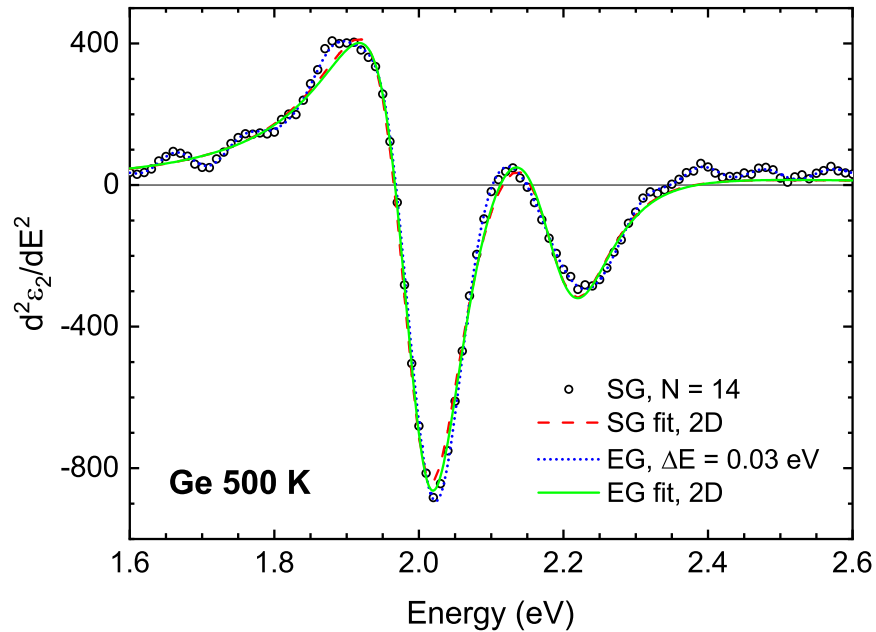


Figure A.5: Same as Fig. A.2 but for the imaginary part of the dielectric function of Ge measured at 500 K from Ref. 16.

A.2 Code

Equation (70) can easily be converted into C++:

```
vector<double> EG(int rows, double lower, double upper,
double DeltaE, double step, vector<double> energy,
vector<double> eps)
{
    int N, index = 0;
    N = fabs(upper - lower) / step + 1;
    double sum = 0.;
    vector<double> fbar(N);
    double constant = (1 / (12288. * sqrt(pi) * DeltaE));

    if (energy[6] < energy[5]) {
        for (int i = N - 1; i >= 0; i--) {
            sum = 0.;
            for (int k = rows - 2; k > 0; k--) {
```

```

sum = sum + constant
* fabs(energy[k + 1] - energy[k - 1])/2.
* (eps[k] * pow(DeltaE, -8.))
* exp(-(lower + i * step - energy[k])
* (lower + i * step - energy[k])
/ (4 * DeltaE * DeltaE))
* (pow(energy[k] - (lower + i * step), 8.)
- 72.
* pow(energy[k] - (lower + i * step), 6.)
* pow(DeltaE, 2.)
+ 1512.
* pow(energy[k] - (lower + i * step), 4.)
* pow(DeltaE, 4.)
- 10080.
* pow(energy[k] - (lower + i * step), 2.)
* pow(DeltaE, 6.)
+ 15120. * pow(DeltaE, 8.));
}
fbar[index] = sum;
index++;
}
}
else
{
for (int i = N - 1; i >= 0; i--) {
sum = 0.;
for (int k = 1; k <= rows - 2; k++) {
sum = sum + constant
* fabs(energy[k + 1] - energy[k - 1])/2.
* (eps[k] * pow(DeltaE, -8.))
* exp(-(lower + i * step - energy[k])
* (lower + i * step - energy[k])
/ (4 * DeltaE * DeltaE))
* (pow(energy[k] - (lower + i * step), 8.)
- 72.
* pow(energy[k] - (lower + i * step), 6.)
* pow(DeltaE, 2.)
+ 1512.
* pow(energy[k] - (lower + i * step), 4.)
* pow(DeltaE, 4.)
- 10080.

```

```

        * pow(energy[k] - (lower + i * step), 2.)
        * pow(DeltaE, 6.)
        + 15120. * pow(DeltaE, 8.));
    }
    fbar[index] = sum;
    index++;
}
}
return fbar;
}

```

A.3 Fitting of the dielectric function with the Hulthén-Tanguy model

Fitting the dielectric function and its second derivatives with the Hulthén-Tanguy model using *Mathematica* showed to be extremely time-consuming. Therefore, I implemented a Levenberg-Marquardt algorithm as defined in chapter 15.5 of Ref. 61 in C++. The Levenberg-Marquardt algorithm was modified, such that it is possible to fit the real and imaginary parts of the dielectric function and their second energy derivatives simultaneously by minimizing a “weighted” χ^2 :

$$\begin{aligned}
\chi^2(\mathbf{a}) = & \sum_{j=1}^N \left[\frac{\epsilon_{1,j} - \epsilon_{1,\text{model}}(E_j, \mathbf{a})}{\sigma} \right]^2 + \sum_{j=1}^N \left[\frac{\frac{d^2 \epsilon_{1,j}}{dE^2} - \frac{d^2 \epsilon_{1,\text{model}}(E_j, \mathbf{a})}{dE^2}}{c\sigma} \right]^2 \\
& + \sum_{j=1}^N \left[\frac{\epsilon_{2,j} - \epsilon_{2,\text{model}}(E_j, \mathbf{a})}{\sigma} \right]^2 + \sum_{j=1}^N \left[\frac{\frac{d^2 \epsilon_{2,j}}{dE^2} - \frac{d^2 \epsilon_{2,\text{model}}(E_j, \mathbf{a})}{dE^2}}{c\sigma} \right]^2, \quad (\text{A5})
\end{aligned}$$

where \mathbf{a} is an array containing all fit parameters, N is the number of data points, $\epsilon_{1(2),j}$ are the data points (i.e. the real(imaginary) part of the dielectric function), $\epsilon_{1(2),\text{model}}(E_j, \mathbf{a})$ is the real(imaginary) part of the dielectric function defined in Eq. 42 (i.e. the Hulthén-Tanguy model), σ is the standard deviation, and c is

a factor used to “weigh” χ^2 of the second derivatives, which otherwise would be orders of magnitudes larger than χ^2 of the dielectric function.

To fit a data set, several steps are required:

1. Perform a discrete Fourier transform along with removal of endpoint discontinuities of the real and imaginary parts.
2. Define the filter width ΔE according to the white noise onset of the Fourier coefficients.
3. Calculate the second derivatives with respect to energy using the EG filters.
4. Fit the Sellmeier coefficients (A_1 and B'_1) to the real part of the dielectric function.
5. Fit the energy and hh-broadening.
6. Set the lh-broadening equal to the hh-broadening.
7. Repeat steps 4, 5, and 6 until best fit parameters are found.

The Levenberg-Marquardt algorithm requires the derivatives with respect to the fit parameters of the function that should be fitted to the data, i.e.

$$\frac{d\epsilon(E)}{dE_0}, \tag{A6}$$

$$\frac{d\epsilon(E)}{d\gamma_{hh}}, \tag{A7}$$

$$\frac{d}{dE_0} \frac{d^2\epsilon(E)}{dE^2}, \quad (\text{A8})$$

and

$$\frac{d}{d\gamma_{hh}} \frac{d^2\epsilon(E)}{dE^2} \quad (\text{A9})$$

In Eq. (42), $\tilde{g}(\xi)$ depends on the digamma function $\psi(z)$. Since both $\epsilon(E)$ and $d^2\epsilon(E)/dE^2$ are fitted to the dielectric function and its second energy derivative, respectively, the first, second, and third derivatives of $\psi(z)$ need to be computed.

An algorithm to calculate the polygamma function is provided in section 3.3.4 in Ref. 108, along with a code, which I converted to C++ and extended to include the above-mentioned derivatives ($d^n\psi(z)/dz^n$ where $n = 0, 1, 2, 3$) using Eq. 3.3.14 in Ref. 108. The Bernoulli numbers needed for the calculation of $d^n\psi(z)/dz^n$ are taken from section 1.1 in Ref. 108. In the following, the code based on section 3.3.4 in Ref. 108 to calculate $d^n\psi(z)/dz^n$, where $n = 1, 2, 3$ is given:

```

complex<double> PolyGamma(int deriv, complex<double> c) {
/*
Notes:
deriv = 1,2,3 defines the ‘‘deriv-th’’ derivative
of the digamma function
c is the complex argument
*/
    complex<double> temp = c;
    complex<double> res;
    double re = real(c);
    double im = imag(c);

    int n;
    double x0, x1 = 1.0, y1, psi, th;

```

```

double z0, z2, rr, ri, tn, tm, ct2, result = 0.;
th = arg(temp);

if (im == 0.0 && re == (int)re && re <= 0.0) {
    psr = 1.0e300;
    psi = 0.0;
}
else {
    if (re < 0.0) {
        x1 = re;
        y1 = im;
        re = -re;
        im = -im;
    }

    x0 = re;

    if (re < 8.0) {
        n = 8 - (int)re;
        x0 = re + n;
    }

    if (x0 == 0.0)
        if (im != 0.0)
            th = 0.5 * pi;
        else
            th = 0.0;
    else
        th = atan(im / x0);

    z2 = x0 * x0 + im * im;
    z0 = sqrt(z2);

    if (deriv == 1) {
        double arr[9] = {
            0.16666666666666667e0,
            -0.3333333333333333e-1,
            0.23809523809523808e-1,
            -0.3333333333333333e-1,
            0.75757575757575758e-1,
            -0.2531135531135531e0,

```

```

1.1666666666666667e0 ,
-7.092156862745098e0 ,
54.971177944862156 };
psr = (x0*x0 - im*im) / (2.*z2*z2) + x0/z2;
psi = -x0*im / (z2*z2) - im/z2;

for (int k = 1; k < 8; k++) {
    psr += arr[k]*pow(z0, -(2.*k+1.))
        *cos((2.*k+1.)*th);
    psi -= arr[k]*pow(z0, -(2.*k+1.))
        *sin((2.*k+1.)*th);
}

if (re < 8.0) {
    rr = 0.0;
    ri = 0.0;
    for (int k = 1; k <= n; k++) {
        rr += ((x0-k)*(x0-k) - im*im)
            /(((x0-k)*(x0-k)-im*im)
            *((x0-k)*(x0-k)-im*im)
            + 4.*(x0-k)*(x0-k)*im*im);
        ri += 2.*(x0-k)*im
            /(((x0-k)*(x0-k)-im*im)
            *((x0-k)*(x0-k)-im*im)
            +4.*(x0-k)*(x0-k)*im*im);
    }
    psr += rr;
    psi -= ri;
}

if (x1 < 0.0) {
    ct2 = (cos(2.*pi*re)-cosh(2.*pi*im))
        *(cos(2.*pi*re)-cosh(2.*pi*im));
    psr += (im*im-re*re)/((im*im+re*re)
        *(im*im+re*re))
        -4.*pi*pi*(sin(pi*re)
        *sin(pi*re)*cosh(pi*im)*cosh(pi*im)
        -cos(pi*re)*cos(pi*re)
        *sinh(pi*im)*sinh(pi*im))/ct2;
    psi += 2.*re*im
        /((im*im+re*re)*(im*im+re*re))

```

```

        +8.*pi*pi*sin(pi*re)*cos(pi*re)
        *sinh(pi*im)*cosh(pi*im)/ct2;
    psr *= -1;
    psi *= -1;
    re = x1;
    im = y1;
}
complex<double> result1(psr, psi);
res = result1;
}
else if (deriv == 2) {
    double arr[9] = {
        -0.5e0,
        0.16666666666666667e0,
        -0.16666666666666667e0,
        0.3e0,
        -0.83333333333333333e0,
        3.2904761904761903e0,
        -17.5e0,
        120.56666666666666e0,
        -1044.452380952381e0 };
    psr = (3.*im*im*x0-pow(x0,3))
        /pow(z2,3)+(im*im-x0*x0)/(z2*z2);
    psi = (-pow(im,3)+3.*im*x0*x0)
        /pow(z2,3)+2.*im*x0/(z2*z2);

    for (int k = 1; k < 9; k++) {
        psr += arr[k]*pow(z0, -(2.*k+2.))
            *cos((2.*k+2.)*th);
        psi -= arr[k]*pow(z0, -(2.*k+2.))
            *sin((2.*k+2.)*th);
    }

    complex<double> temp, I(0., 1.), cpi(pi, 0.);

    if (re < 8.0) {
        rr = 0.0;
        ri = 0.0;
        for (int k = 1; k <= n; k++) {
            temp = -2.*I/pow(x0-k+I*im, 3);
            rr += real(temp);

```

```

        ri += imag(temp);
    }
    psr += rr;
    psi += ri;
}
if (x1 < 0.0) {
    temp = 2.*I/(pow(re+im*I,3))
          +2.*I*pow(cpi,3)
          /(tan(cpi*(re+im*I))
             *sin(cpi*(re+im*I))
             *sin(cpi*(re+im*I)));
    psr += real(temp);
    psi += imag(temp);
    re = x1;
    im = y1;
}
complex<double> result2(psr, psi);
res = result2;
}
else if (deriv == 3) {
    double arr[9] = {
        2.0e0,
        -1.0e0,
        1.3333333333333333e0,
        -3.0e0,
        1.0e1,
        -46.066666666666667e0,
        2.80e2,
        -2.1702e3,
        2.0889e4 };
    psr = (3.*pow(im, 4)-18.*pow(x0*im, 2)
           +3.*pow(x0, 4))
           /pow(z2,4)+(2.*pow(x0, 3)-6.*im*im*x0)
           /pow(z2,3);
    psi = 12.*(pow(im, 3)*x0-im*pow(x0, 3))
           /pow(z2,4)+(2.*pow(im, 3)-6.*im*x0*x0)
           /pow(z2,3);

    for (int k = 1; k < 9; k++) {
        psr += arr[k]*pow(z0, -(2.*k+3.0))
              *cos((2.*k+3.)*th);
    }
}

```

```

        psi -= arr[k]*pow(z0, -(2.*k+3.0))
            *sin((2.*k+3.)*th);
    }

    complex<double> temp, I(0., 1.), cpi(pi, 0.);

    if (re < 8.) {
        rr = 0.0;
        ri = 0.0;
        for (int k = 1; k <= n; k++) {
            temp = 6.*I/pow(x0-k+I*im, 4);
            rr += real(temp);
            ri += imag(temp);
        }
        psr += rr;
        psi += ri;
    }

    if (x1 < 0.0) {
        temp = - 6.*I/ (pow(re+im*I, 4))
            -2.*I*pow(cpi, 4)
            *(2.*I/pow(tan(cpi*(re+im*I))
            *sin(cpi*(re+im*I)), 2)
            -pow(sin(cpi*(re+im*I)), -4));
        psr += real(temp);
        psi += imag(temp);
        psr *= -1;
        psi *= -1;
        re = x1;
        im = y1;
    }
    complex<double> result3(psr, psi);
    res = result3;
}
}
return res;
}

```

The *Mathematica* command `CForm[]` converts *Mathematica* code into C++

language. This makes it possible to simply convert the various derivatives computed with the help of *Mathematica* and include it into the C++ program (and avoid typing thousands of lines of code by hand).

REFERENCES

- [1] G. G. Macfarlane, T. P. McLean, J. E. Quarrington, and V. Roberts, *Phys. Rev.* **108**, 1377 (1957).
- [2] W. Bludau, A. Onton, and W. Heinke, *J. Appl. Phys.* **45**, 1846 (1974).
- [3] R. Soref, *Nat. Photonics* **4**, 495 (2010).
- [4] G. G. Macfarlane, T. P. McLean, J. E. Quarrington, and V. Roberts, *J. Phys. Chem. Solids* **8**, 388 (1959).
- [5] J. Menéndez, D. J. Lockwood, J. C. Zwickels, and M. Noël, *Phys. Rev. B* **98**, 165207 (2018).
- [6] C. Emminger, F. Abadizaman, N. S. Samarasingha, T. E. Tiwald, and S. Zollner, *J. Vac. Sci. Technol. B* **38**, 012202 (2020).
- [7] C. Tanguy, *Phys. Rev. B* **60**, 10660 (1999).
- [8] J. Shah, *Ultrafast Spectroscopy of Semiconductors and Semiconductor Nanostructures*, (Springer, Berlin, 1999).
- [9] S. Espinoza, S. Richter, M. Rebarz, O. Herrfurth, R. Schmidt-Grund, J. Andreasson, and S. Zollner, *Appl. Phys. Lett.*, **115**, 052105, (2019).
- [10] C. Thomsen, H. T. Grahn, H. J. Maris, and J. Tauc, *Phys. Rev. B* **34**, 4129 (1986).
- [11] V. L. Le, T. J. Kim, Y. D. Kim, and D. E. Aspnes, *J. Vac. Sci. Technol. B* **37**, 052903 (2019).
- [12] H. Fujiwara, *Spectroscopic ellipsometry: principles and applications* (John Wiley & Sons, West Sussex, England, 2007).
- [13] R. M. A. Azzam and N. M. Bashara, *Ellipsometry on polarized light* (North Holland Publ. Co., Amsterdam, 1984).
- [14] M. Fox, *Optical properties of solids* (Oxford University Press, New York, 2010).
- [15] J. A. Woollam Co., Inc., Lincoln, NE. Model V-VASE.
- [16] C. Emminger (2017), (Master thesis, Johannes Kepler University, Linz, Austria).

- [17] F. Abadizaman (2020), (Ph.D. thesis, New Mexico State University, Las Cruces, NM, USA).
- [18] T. N. Nunley, N. S. Fernando, N. Samarasingha, J. M. Moya, C. M. Nelson, A. A. Medina, and S. Zollner, *J. Vac. Sci. Technol. B* **34**, 061205 (2016).
- [19] C. M. Herzinger and B. Johs, U.S. Patent No. 5,796,983 (18 August 1998).
- [20] N. S. Fernando, T. N. Nunley, A. Ghosh, C. M. Nelson, J. A. Cooke, A. A. Medina, S. Zollner, C. Xu, J. Menendez, and J. Kouvetakis, *Appl. Surf. Sci.* **421**, 905 (2017).
- [21] P. Y. Yu and M. Cardona, *Fundamentals of Semiconductors: Physics and Materials Properties*, (Springer-Verlag, Berlin, 1996).
- [22] L. Van Hove, *Phys. Rev.* **89**, 1189 (1953).
- [23] L. Viña, S. Logothetidis, and M. Cardona, *Phys. Rev. B* **30**, 1979 (1984).
- [24] D. E. Aspnes, *Handbook on Semiconductors*, edited by M. Balkanski (North-Holland, Amsterdam, 1980).
- [25] M. Cardona, *Modulation Spectroscopy*, edited by F. Seitz, D. Turnbull, and H. Ehrenreich (Academic, New York, 1969).
- [26] D. E. Aspnes, *Phys. Rev. B* **12**, 2297 (1975).
- [27] R. J. Elliott, *Phys. Rev.* **108**, 1384 (1957).
- [28] C. Tanguy, *Phys. Rev. Lett.* **75**, 4090 (1995).
- [29] The data were retrieved from the data base of the *WVASE* software by *J. A. Woollam Co., Inc.* and were tabulated at the University of Lincoln-Nebraska.
- [30] *J. A. Woollam Co., Inc.*, Lincoln, NE. Model FTIR.
- [31] C. Thomsen, J. Strait, Z. Vardeny, H. J. Maris, and J. Tauc, *Phys. Rev. Lett.* **53**, 989 (1984).
- [32] M. Chandrasekhar and F. H. Poollak, *Phys. Rev. B* **15**, 2127 (1977).
- [33] P. Etchegoin, J. Kircher, M. Cardona, C. Grein, *Phys. Rev. B* **45**, 11721 (1992).
- [34] J. F. Nye, *Physical Properties of Crystals*, (Oxford Univ. Press, Oxford, 1969).

- [35] R. C. Powell, *Symmetry, Group Theory, and the Physical Properties of Crystals* (Springer, New York, 2010).
- [36] S. Zollner, in: S.T. Pantelides, S. Zollner (Eds.), *Silicon-Germanium Carbon Alloys: Growth, Properties and Applications*, (Taylor&Francis, New York, 2002), p. 387.
- [37] A. Savitzky, and M. J. E. Golay, *Anal. Chem.* **36**, 1627 (1964).
- [38] V. R. D'Costa, Y. Fang, J. Mathews, R. Roucka, J. Tolle, J. Menéndez, and J. Kouvetakis, *Semicond. Sci. Technol.* **24**, 115006 (2009).
- [39] R. Roucka, R. Beeler, J. Mathews, M.Y. Ryu, Y. Kee Yeo, J. Menéndez, and J. Kouvetakis, *J. Appl. Phys.* **109**, 103115 (2011).
- [40] L. Hulthén, *Ark. Mat. Astron. Fys.* **28A**, 1 (1999).
- [41] A. Ferreira da Silva, *Phys. Rev. B* **37**, 4799 (1988).
- [42] S. D. Yoo and D. E. Aspnes, *J. Appl. Phys.* **89**, 8183 (2001).
- [43] D. E. Aspnes, V. L. Le, and Y. D. Kim, *J. Vac. Sci. Technol. B* **37**, 051205 (2019).
- [44] V. L. Le, T. J. Kim, Y. D. Kim, and D. E. Aspnes, *J. Kor. Sci. Phys. Soc.* **77**, 819 (2020).
- [45] D. K. Hoffman, T. L. Marchioro, M. Arnold, Y. Huang, W. Zhu, and D. J. Kouri, *J. Math. Chem.* **20**, 117 (1996).
- [46] D. K. Hoffman, D. J. Kouri, and E. Pollak, *Comput. Phys. Commun.* **147**, 759 (2002).
- [47] J. Menéndez, C. D. Poweleit, and S. E. Tilton, *Phys. Rev. B* **101**, 195204 (2020).
- [48] D. B. Cuttris, *Bell Syst. Techn. J.* **40**, 509 (1961).
- [49] B. Tattian, *Appl. Opt.* **23**, 4477 (1984).
- [50] E. O. Kane, *J. Phys. Chem. Solids* **1**, 82 (1956).
- [51] E. O. Kane, *J. Phys. Chem. Solids* **1**, 249 (1957).
- [52] M. Cardona, *J. Phys. Chem. Solids* **24**, 1543 (1963).
- [53] M. Hobden, *J. Phys. Chem. Solids* **23**, 821 (1962).

- [54] C. Persson and U. Lindefelt, *J. Appl. Phys.* **82**, 5496 (1997).
- [55] G. Dresselhaus, A. Kip, and C. Kittel, *Phys. Rev.* **98**, 368 (1955).
- [56] G. G. Macfarlane, T. P. McLean, J. E. Quarrington, and V. Roberts, *Proc. Phys. Soc.* **71**, 863 (1958).
- [57] P. Lawaetz, *Phys. Rev. B* **4**, 3460 (1971).
- [58] L. M. Roth, B. Lax, and S. Zwerdling, *Phys. Rev.* **114**, 90 (1959).
- [59] V. L. Le, Y. D. Kim, and D. E. Aspnes, *Opt. Express* **28**, 38917 (2020).
- [60] V. L. Le, T. J. Kim, Y. D. Kim, and D. E. Aspnes, *J. Appl. Phys.* **129**, 224902 (2021).
- [61] S. A. Teukolsky, B. P. Flannery, W. H. Press, and W. T. Vetterling, *Numerical recipes in C* (Press Syndicate of the University of Cambridge, New York, 1992), Chap. 15.5.
- [62] T. P. McLean and E. G. S. Paige, *J. Phys. Chem. Solids* **23**, 822 (1962).
- [63] T. P. McLean and E. G. S. Paige, in *Proceedings of the International Conference on the Physics of Semiconductors*, edited by A. C. Stickland, 450 (Institute of Physics, London, 1962).
- [64] G. Nelin and G. Nilsson, *Phys. Rev. B* **10**, 612 (1974).
- [65] P. Lautenschlager, P. B. Allen, and M. Cardona, *Phys. Rev. B* **33**, 5501 (1986).
- [66] T. Nishino, T. Yanagida, and Y. Hamakawa, *J. Phys. Soc. Japan* **30**, 579 (1971).
- [67] G. H. Li, A. R. Goñi, K. Syassen, and M. Cardona, *Phys. Rev. B* **49**, 8017 (1994).
- [68] N. S. Samarasingha and S. Zollner, *J. Vac. Sci. Technol. B* **39**, 052201 (2021).
- [69] F. A. D'Altroy and H. Y. Fan, *Phys. Rev.* **103**, 1671 (1956).
- [70] N. Tandon, J. D. Albrecht, and L. R. Ram-Mohan, *J. Appl. Phys.* **118**, 045713 (2015).
- [71] V. G. Tyuterev, S. V. Obukhov, N. Vast, and J. Sjakste, *Phys. Rev. B* **84**, 035201 (2011).

- [72] E. M. Conwell, *High Field Transport in Semiconductors*, (Academic, New York, 1967).
- [73] D. K. Ferry, in *Semiconductor Transport*, (Taylor & Francis, New York, 2000).
- [74] L. Reggiani, *Hot-Electron Transport in Semiconductors*, (Springer, New York, 1985).
- [75] B. R. Nag, in *Semiconductors Probed by Ultrafast Laser Spectroscopy*, edited by R. R. Alfrano, Vol. 1 (Academic Press, London, 1984).
- [76] W. Pötz and P. Vogl, Phys. Rev. B **24**, 2025 (1981).
- [77] S. Zollner, S. Gopalan, and M. Cardona, J. Appl. Phys. **68**, 1682 (1990).
- [78] W. Weber, Phys. Rev. B **15**, 4789 (1977).
- [79] S. Zollner, S. Gopalan, and M. Cardona, Sol. State Comm. **76**, 877 (1990).
- [80] Y. Toyozawa, J. Phys. Chem. Solids **25**, 59 (1964).
- [81] S. Richter, M. Rebarz, O. Herrfurth, S. Espinoza, R. Schmidt-Grund, and J. Andreasson, Rev. Sci. Instrum. **92**, 033104 (2021).
- [82] H. T. Grahn, H. J. Maris, and J. Tauc, IEEE J. Quantum Elect. **25**, 2562 (1989).
- [83] O. B. Wright, B. Perrin, O. Matsuda, and V. E. Gusev, Phys. Rev. B **64**, 081202 (2001).
- [84] K. Ishioka, A. Rustagi, U. Höfer, H. Petek, and C. J. Stanton, Phys. Rev. B **95**, 035205 (2017).
- [85] M. Vinod, G. Raghavan, V. Sivasubramanian, Sci. Rep. **8**, 17706 (2018).
- [86] X. Han, M. Wang, W. Zhao, X. Xing, K. Wang, and P. Lu, Opt. Comm. **461**, 125257 (2020).
- [87] S. Wu, P. Geiser, J. Jun, J. Karpinski, J.-R. Park, and R. Sobolewski, Appl. Phys. Lett. **88**, 041917 (2006).
- [88] K. Ishioka, K. Brixius, A. Beyer, A. Rustagi, C. J. Stanton, W. Stolz, K. Volz, U. Höfer, and H. Petek, Appl. Phys. Lett. **108**, 051607 (2016).
- [89] K. Ishioka, A. Beyer, W. Stolz, K. Volz, H. Petek, U. Höfer, and C. J. Stanton, J. Phys.: Condens. Matter **31**, 094003 (2019).

- [90] Y.-K. Huang, G.-W. Chern, C.-K. Sun, Y. Smorchkova, S. Keller, U. Mishra, and S. P. DenBaars, *Appl. Phys. Lett.* **79**, 3361 (2001).
- [91] C.-K. Sun, J.-C. Liang, C. J. Stanton, A. Abare, L. Coldren, and S. P. DenBaars, *Appl. Phys. Lett.* **75**, 1249 (1999).
- [92] J. Wang, Y. Hashimoto, J. Kono, A. Oiwa, H. Munekata, H. Sanders, and C. J. Stanton, *Phys. Rev. B* **72**, 153311 (2005).
- [93] R. Liu, C. S. Kim, G. D. Sanders, C. J. Stanton, J. S. Yahng, Y. D. Jho, K. J. Yee, E. Oh, and D. S. Kim, *Phys. Rev. B* **72**, 195335 (2005).
- [94] P. Babilotte, P. Ruello, D. Mounier, T. Pezeril, G. Vaudel, M. Edely, J.-M. Breteau, and V. Gusev, *Phys. Rev. B* **81**, 245207 (2010).
- [95] P. Lautenschlager, M. Garriga, L. Viña, and M. Cardona, *Phys. Rev. B* **36**, 4821 (1987).
- [96] C. Xu, N. S. Fernando, S. Zollner, J. Kouvetakis, and J. Menéndez, *Phys. Rev. B* **118**, 267402 (2017).
- [97] L. E. Vorobyev, *Handbook Series on Semiconductor Parameters, Vol. 1: Si, Ge, C (Diamond) GaAs, GaP, GaSb, InAs, InP, InSb* edited by M. Levinshstein, S. Rumyantsev, and M. Shur (World Scientific, Singapore, 1996).
- [98] G. A. Slack and S. F. Bartram, *J. Appl. Phys.* **46**, 89 (1975).
- [99] Y. Okada and Y. Tokumaru, *J. Appl. Phys.* **56**, 314 (1984).
- [100] D. Gerlich, B. Abeles, and R. E. Miller, *J. Appl. Phys.* **36**, 76 (1965).
- [101] W. Paul, *J. Appl. Phys.* **32**, 2082 (1961).
- [102] H. J. McSkimin and P. Andreatch, *J. Appl. Phys.* **35**, 2161 (1964).
- [103] D. E. Aspnes and A. A. Studna, *Phys. Rev. B* **27**, 985 (1983).
- [104] T. Pfeifer, W. Kütt, H. Kurz, and R. Scholz, *Phys. Rev. Lett.* **69**, 3248 (1992).
- [105] K. Ishioka, M. Kitajima, and O. V. Misochko, *J. Appl. Phys.* **103**, 123505 (2008).
- [106] K. Ishioka, M. Hase, M. Kitajima, L. Wirtz, A. Rubio, and H. Petek, *Phys. Rev. B* **77**, 121402 (2008).
- [107] M. Hase, J. Demsar, and M. Kitajima, *Phys. Rev. B* **74**, 212301 (2006).

- [108] S. Zhang and J. Jin, *Computation of Special Functions*, (John Wiley & Sons, 1996).